Consortium

for

Small-Scale Modelling

Newsletter

April 2013 *No. 13*

Deutscher Wetterdienst

MeteoSwiss

Ufficio Generale Spazio Aereo e Meteorologia

ΕΘΝΙΚΗ ΜΕΤΕΩΡΟΛΟΓΙΚΗ ΥΠΗΡΕΣΙΑ

Instytucie Meteorogii i Gospodarki Wodnej

Administraţia Naţională de Meteorologie

Agenzia Regionale per la Protezione Ambientale dell'Emilia Romagna Servizio Idro Meteo Clima

Federal Service for Hydrometeorology and Environmental Monitoring

Centro Italiano Ricerche Aerospaziali

Amt für GeoInformationswesen der Bundeswehr

Agenzia Regionale per la Protezione Ambientale del Piemonte

www.cosmo-model.org

Editors: Cosmin Barbu (NMA); Massimo Milelli (ARPA-Piedmont); Ulrich Schättler (DWD);

Table of Contents

Editorial **1**

Michał Ziemiański 1

1 Working Group on Data Assimilation **3**

Are atmospheric-model tendency errors perceivable from routine observations?
M. Tsyrulnikov, V. Gorin 3

COSMO Data Assimilation. Applications for Romanian Territory
A. Iriza, R. C. Dumitrache, C. D. Barbu, A. Lupaşcu, B. A. Maco 19

2 Working Group on Physical Aspects: Upper Air **25**

Implementation of TKE–Scalar Variance Mixing Scheme into COSMO
E. Machulskaya, D. Mironov 25

On the Direct Comparison of COSMO Model Sub-Grid Stratiform Cloud Schemes with Satellite Images
E. Avgoustoglou 34

3 Working Group on Physical Aspects: Soil and Surface **39**

Realization of the parametric snow cover model SMFE for snow characteristics calculation according to standard net meteorological observations
E. Kazakova, M. Chumakov, I. Rozinkina 39

New Approach to Parameterization of Physical Processes in Soil in COSMO Model - Preliminary Results
G. Duniec, A. Mazur 50

4 Working Group on Interpretation and Applications **56**

On thunderstorm quantification
J. Parfiniewicz 56

Operational multiscale modelling system for air quality forecast
M. Giorcelli, S. Bande, M. Muraro, M. Milelli 58

5 Working Group on Verification and Case Studies **64**

Using synoptic classification to evaluate COSMOGR through Weather Dependant Verification
F. Gofa ,D. Tzeferi 64

Tropospheric Delay (ZTD) and Precipitable Water data from COSMO model vs. geodetic GPS network data
M. Kruczyk, A. Mazur 69

COSMO model validation using the Italian radar mosaic and the rain gauges estimated precipitation
N. Vela, R. Cremonini, E. Oberto, M. Giorcelli 83

6 Working Group on Predictability and Ensemble Methods 93

Development of a COSMO–based limited–area ensemble system for the 2014 Winter Olympic Games
A. Montani, C. Marsigli, T. Paccagnella 93

Test of a COSMO-based convection-permitting ensemble in the Hymex framework
C. Marsigli, A. Montani, T. Paccegnella 100

Appendix: List of COSMO Newsletters and Technical Reports 105

The current issue of the COSMO Newsletter presents a selection of articles on the recent COSMO developments and results. They were extensively reviewed and discussed during the COSMO General Meeting which took place from 10 to 13 September 2012 in Lugano, Switzerland. You can find the meeting presentations at http://www.cosmo-model.org/content/consortium/generalMeetings/general2012/default.htm.

During the current COSMO year, we focus especially on development of the new version V5.0 of the COSMO model which unifies the recent code developments for our ART, CLM and NWP communities. The new version will become a good operational and scientific tool to fulfill our current requirements and needs, and will lay a foundation for further coordinated code development. The code development is managed according to the recently approved coding standards and using recently redesigned code management web pages.

The work on renewed COSMO strategy, to be outlined in the revised COSMO Science Plan, starts during this COSMO year. We are all invited to actively participate in the work and discussions, involved. They will take place on all the levels of our consortium and I expect especially lively and fruitful discussions taking place on the level of the Working Groups. The important aim of our discussion is also to address the cross-cutting issues, like e.g. strategy for further code improvement and development or nowcasting. I look forward to the results of all the discussions.

For the next General Meeting, we will meet in Sibiu, Romania, from 2 to 5 September 2013.

Michał Ziemiański
COSMO Scientific Project Manager

Participants of the 14th COSMO General Meeting in Lugano

Are atmospheric-model tendency errors perceivable from routine observations?

Michael Tsyrulnikov[1] and Vadim Gorin[2]

1: HydroMetCenter of Russia
2: Massachusetts Institute of Technology

1 Abstract

In predictability experiments with simulated model errors (ME) and the COSMO model, reproducibility of ME from finite-time model-minus-observed tendencies is studied. It is found that in 1-h to 6-h tendencies, ME appear to be too heavily contaminated by noises due to, first, initial errors and, second, trajectory drift as a result of ME themselves. The resulting reproducibility error is far above the acceptable level. The conclusion is drawn that the accuracy and coverage of current routine observations are far from being sufficient to reliably estimate ME.

2 Introduction

ME (defined as tendency errors) are a very important source of forecast errors in meteorology. Both in ensemble prediction and ensemble data assimilation, ME need to be simulated according to their probability distribution (their spatio-temporal structure). However, very little is known to date on this subject. So, any objective knowledge on ME would be very helpful.

This study aims to advance our understanding of the ME structures in the atmosphere, including their spatio-temporal and cross-variable aspects. ME are intended here to be estimated using real observations, so that model tendencies can be confronted with observed tendencies. The first question — can ME be recovered from realistic finite-time model-tendencies vs. observed-tendencies? — is addressed in this note.

3 ME: the general paradigm

3.1 Definition of ME

We start with the forecast equation

$$\frac{\mathrm{d}X}{\mathrm{d}t} = F(X), \tag{1}$$

where $X = X^m$ is the model (forecast) state and F the model r.h.s. (model operator).

If we substitute the truth into Eq.(1), a discrepancy arises (because the model operator F is always not perfect) — this discrepancy is called the *model error*.

Otherwise stated, the ME is defined as the difference between the model tendency $F(X)$ (evaluated at the true system state!) and the true tendency (e.g. Orrell et al. 2001):

$$\varepsilon = F(X^t) - \frac{\mathrm{d}X^t}{\mathrm{d}t}, \tag{2}$$

where the superscript t denotes the truth.

Strictly speaking, X^t is the true system state *mapped to the model space*. To elaborate on this, we introduce a hypothetical *full* functional space, $\mathcal{X}_{full}$, where a 'full' system state X_{full} is defined and which includes more variables than the *model space* $\mathcal{X}$ (say, minor atmospheric gases, aerosols etc.) at much higher (maybe, infinite) resolution. We need this *full* space in order to be able to hypothesize the existence of a deterministic differential equation (like Eq.(1)) that governs the true atmospheric state (in the relatively small *model* space, we certainly cannot believe that such a deterministic equation for the truth exists):

$$\frac{\mathrm{d}X_{full}}{\mathrm{d}t} = F^t_{full}(X_{full}), \tag{3}$$

where $X_{full} \in \mathcal{X}_{full}$ and F^t_{full} is the hypothetical perfect full-space model operator.

We assume that the model space $\mathcal{X}$ is a subspace of the full space $\mathcal{X}_{full}$, with a projection $\mathcal{P}$ of $\mathcal{X}_{full}$ onto $\mathcal{X}$: $X = \mathcal{P}X_{full}$.

Next, we apply the projection operator $\mathcal{P}$ to Eq.(3), getting

$$\frac{\mathrm{d}X}{\mathrm{d}t} = \mathcal{P}F^t_{full}(X_{full}) =: F^t(X_{full}). \tag{4}$$

So, the model-space state vector X (any state vector, not just the true one) satisfies:

$$\frac{\mathrm{d}X}{\mathrm{d}t} = F^t(X_{full}). \tag{5}$$

Now, we have both the model tendency $F(X)$ and the true tendency $F^t(X_{full})$, so that the ME can be defined as their difference:

$$\varepsilon = F(X) - F^t(X_{full}), \tag{6}$$

where $X = \mathcal{P}X_{full}$.

From Eq.(6), it follows that ε is a function of the point in *full* space: $\varepsilon = \varepsilon(X_{full})$ (in other words, ε in *defined* on $\mathcal{X}_{full}$).

Note that this second definition of ME given by Eq.(6) is, in a sense, more general than the usual definition given by Eq.(2). Indeed, Eq.(2) defines ME only at an actual true system state X^t, whereas Eq.(6) defines ME at any point in full space. This more general definition may be helpful in understanding the nature of ME and can be used in practice if an approximation to the true model $F^t(X_{full})$ is available.

We conclude the definitions subsection by remarking that the above ME are defined as *additive*: $\varepsilon = \varepsilon_{add} = F - F^t$. In principle, one could define them as multiplicative or in some other way.

3.2 How to evaluate ME?

Apparently, Eq.(6) can be useful in evaluating ε only if the true model-space operator $F^t(X_{full})$ is available. If not, we have to use the ME definition Eq.(2) and rely on the *observed truth* $X^t|_{obs}$ (not the *full* truth X^t_{full} and even not the model-space truth X^t!): e.g., we may expect that horizontal winds or temperature are observed, whereas vertical wind is not, etc.

Assuming $X^t|_{obs}$ is available for some period of time and aiming to evaluate ε, we use Eq.(2) evaluated at $X = X^t|_{obs}$:

$$\varepsilon|_{obs} = F|_{obs}(X^t) - \frac{\mathrm{d}X^t|_{obs}}{\mathrm{d}t}. \tag{7}$$

Here and elsewhere, $|_{obs}$ denotes restriction to *observed* space $\mathcal{X}|_{obs}$: $X|_{obs} = \Pi X$, where Π is the suitable projection (spatial interpolation to observation points).

Note that the standard definition of ME, Eq.(2), can be regarded as a particular case of Eq.(7) when the entire X^t is observed. Normally, X^t is *not* completely observed, so our basic equation in ME estimation will be Eq.(7).

It is worth stressing at this point that in Eq.(7), the argument of $F|_{obs}$ is the *model-space* (not observed-space!) X^t, which is only partially observed. This is the first major obstacle in objective ME evaluation/estimation: given the partially observed truth, $X^t|_{obs}$, we cannot exactly evaluate ε and so approximations are indispensable. In the predictability theory language, lack of X^t knowledge is nothing other than the error in initial conditions (analysis error). The other major obstacle — finite-time-tendency approximations — is discussed below.

We conclude this subsection by reiterating that we have defined the hierarchy of three embedded phase spaces:

1. The largest (hypothetical) *full* space $\mathcal{X}_{full}$, where the *true* system equation operates.
2. The medium (forecast) *model* space $\mathcal{X}$, where the *forecast* equation (the forecst model) is defined, $\mathcal{X} = \mathcal{P}\mathcal{X}_{full}$.
3. The smallest *observed* space $\mathcal{X}|_{obs}$, which consists of those model-space points that can be *observed*, $\mathcal{X}_{obs} = \Pi\mathcal{X}$.

3.3 Stochastic modelling of ME

From Eq.(6), we see that ME is some (unknown and, presumably, very complicated) function of the 'full' system state X_{full}. In reality, the 'full' system state is not just huge but even unknown, so that given some X, we are unable to recover $F^t(X_{full})$ not only because F^t is unknown but also because X_{full} is unavailable. This leads us to model the ME stochastically.

4 Finite-time ME

As only finite-time tendencies are observable in real world, we turn to time-integrated tendencies and ME.

If we regard system (model) state as an element of the respective functional (or, in the spatially discrete case, Euclidean) space, then Eq.(7) is nothing other than an ordinary differential equation. Therefore, we are allowed to integrate it in time from t_0 to $t_0 + \Delta t$, getting:

$$\breve{\varepsilon} := \int \varepsilon \, \mathrm{d}t = \int F(X^t) \, \mathrm{d}t - \Delta X^t, \tag{8}$$

where Δf denotes, for any function f, the temporal finite difference $\Delta f = f(t_0 + \Delta t) - f(t_0)$ and $\breve{f}$ stands for time integrated f: $\breve{f} = \int_{t_0}^{t_0+\Delta t} f(t) \, \mathrm{d}t$ [mnemonics: $\breve{}$ is reminiscent of an *accumulation* device]. Note that $\breve{\varepsilon}$ is sometimes called the *drift* (e.g. Orrell et al. 2001).

In Eq.(8), ΔX^t is available through observations (up to an observation error with known probability distribution); the unavailable quantity $F(X^t)$ can be approximated by the best available one, $F(X^m)$, where X^m is the model forecast started from an analysis. The replacement $X^t \to X^m$ gives rise to the error

$$\delta := \int F(X^m) \, \mathrm{d}t - \int F(X^t) \, \mathrm{d}t, \tag{9}$$

so that, since $\int F(X^m)\,\mathrm{d}t = \Delta X^m$, we have

$$\breve{\varepsilon} = \Delta X^m - \Delta X^t - \delta. \tag{10}$$

The error term δ appears due to, first, the initial-conditions difference ($X^m(t_0)$ differs from $X^t(t_0)$) and second, due to the drift of the model trajectory from the true one — provided both trajectories start from the same initial conditions. Indeed, denote by $X^{mt}(t)$ the (phase-space) *model* trajectory started from *true* initial conditions, see Fig.1.

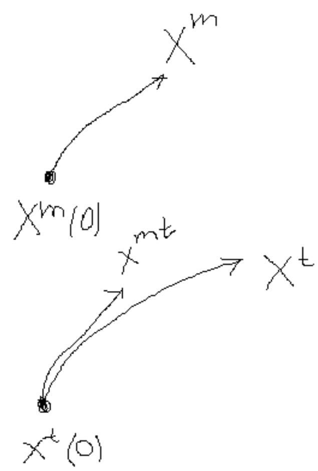

Figure 1: Model forecast X^m, the truth X^t, and the model forecast X^{mt} started from true initial conditions.

We may rewrite Eq.(9) as

$$\delta = \int [F(X^m) - F(X^{mt})]\,\mathrm{d}t + \int [F(X^{mt}) - F(X^t)]\,\mathrm{d}t. \tag{11}$$

Here, the first integral,

$$\delta_{ie} := \int [F(X^m) - F(X^{mt})]\,\mathrm{d}t. \tag{12}$$

is purely due to the forecast error growth in response to the initial error (the *internal* error growth, see e.g. Reynolds et al. 1994). The second integral,

$$\delta_{me} := \int [F(X^{mt}) - F(X^t)]\,\mathrm{d}t. \tag{13}$$

does not contain any contribution from the initial error $X^m(t_0) - X^t(t_0)$ and is solely due to ME (the *external* error growth, Reynolds et al. 1994).

In the Appendix, it is shown that for very small tendency interval lengths Δt, δ_{me} can be neglected: $\delta_{me} \ll \breve{\varepsilon}$. But experimentally, we found that in order for δ_{me} to be really negligible, Δt needs to be as small as 1 h (!) for winds and about 6 h for temperature (see below the numerical experiments section).

In general, both terms should be retained:

$$\breve{\varepsilon} = \Delta X^m - \Delta X^t - \delta_{ie} - \delta_{me}. \tag{14}$$

In the realistic situation, when the truth is available through noisy observations $X^o = X^t + \eta$, where η is the observation error, ΔX^t should be replaced in this equation by the *observed* tendency, ΔX^o:

$$\breve{\varepsilon} = \Delta X^m - \Delta X^o - \delta_{ie} - \delta_{me} - \Delta\eta. \tag{15}$$

The accumulated ME $\breve{\varepsilon}$ can only be seen in the observable $\Delta X^m - \Delta X^o$ difference if the noise terms δ_{ie}, δ_{me}, and $\Delta\eta$ in Eq.(15) are small enough. This, again, is will be checked in numerical experiments, see below. In principle, the 'signal' $\breve{\varepsilon}$ can be extracted from the difference $\Delta X^m - \Delta X^o$ not only if the noise is small but also if the noise has very well known probabilistic distribution. But this does not seem to be case in this problem: only the observation noise can be assumed to have more or less known distribution. The analysis error δ_{ie} and the model-error finite-time distortion δ_{me} are too poorly known. So, all we can hope is to find that the noise is small — compared with the forecast tendency (or the observed tendency).

5 Numerical predictability experiments

5.1 Goals

Using predictability experiments with known *a priori* ('synthetic') ME, find out whether the ME can be recovered (estimated) from forecast and observed (Eulerian) tendencies. In particular, assess the roles of the noise sources, δ_{ie} and δ_{me}, which contaminate the finite-time ME, $\breve{\varepsilon}$, as functions of observation-error variance, model-error variance, and the length of the finite-time tendency Δt.

5.2 The forecast model

COSMO model version 4.13 is used. The model grid has 40 full levels (41 half levels), 14 km mesh size in the horizontal, and has the top at about 40 hPa. The domain is European Russia (about 4500 by 5000 km).

5.3 Methodology

In the most general terms, we mimic the intermittent data assimilation cycle with "synthetic" observations and ME model (MEM), so that the observation-error statistics (variance) and ME themselves are known *a priori*.

5.3.1 Model errors

We assume here that only temperature and horizontal winds forecast equations are in error. We employ the simplest non-degenerate MEM: for each of the fields T, u, and v, the respective ε are specified to be *additive and constant in space and time during one assimilation cycle* (6 h). At different assimilation cycles (6-h intervals) ε are mutually independent zero-mean Gaussian pseudo-random variables with pre-specified variance σ_ε^2.

Thus, σ_ε is the only parameter of MEM for each of the three fields: T, u, v.

It is worth stressing that this MEM is not only the simplest one but also the one which can be most easily estimated. So, we simplified the MEM estimation problem to the greatest sensible extent. Our intention here is to try to solve the simplest problem, so that if we fail, there will be no sense to tackle the problem in a more realistic setup.

5.3.2 The 'truth'

The truth run is accomplished by time integration of the perturbed COSMO model: at each model time step, ε is subtracted from the r.h.s. of the model equations following the equation for the truth,

$$\frac{\mathrm{d}X^t}{\mathrm{d}t} = F(X^t) - \varepsilon. \tag{16}$$

(see Eqs.(7) and (2)).

The upper and lateral boundary conditions are exactly the same as for the model forecast (see below).

5.3.3 Observations

We assume that every degree of freedom in the fields T, u, v, q is observed — subject to observation error η.

In order to make the analysis (described below is this section) as simple as possible, we impose the observation error field that has, roughly, the same covariances as analysis background (6-h forecast) error covariances. Aiming at decorrelation length scales of about 100 km in the horizontal and 100 hPa in the vertical, we employ the following technique.

First, at the *thinned* COSMO grid (in the below experiments, we take every 5th grid point in the horizontal and every or 3rd grid point in the vertical), we simulate white noise with some variance σ^2_{ini} subject to subsequent tuning.

Second, we tri-linearly interpolate the observation-error field from the thinned grid to the full grid.

Third, we apply, several times, a smoothing filter (a moving average operator), which is defined as a simple averaging over the $5 \times 5 \times 3$ cube on the grid (5×5 in the horizontal and 3 in the vertical) on the COSMO grid. The more smoothing sweeps, the smoother the resulting field. There is also a minimum number of sweeps needed to make the field homogeneous (so that points on the thinned grid are no longer distinguishable from other grid points in the simulated fields).

For the selected number of sweeps (5 sweeps are used in the experiments described below), the variance σ_{ini} is finally tuned to yield the desired observation-error variance $\sigma^2|_{obs}$.

A realization of the pseudo-random observation-noise field is displayed in Fig.2 (a horizontal cross-section) and Fig.3 (a vertical cross-section).

5.3.4 Analysis

The analysis is univariate for all 4 fields (T, u, v, q). Since observations are placed at all grid points, the observation operator is the identity matrix for each univariate analysis: $H = I$. So, the gain matrix becomes

$$K = B(B + R)^{-1}. \tag{17}$$

As noted above, we assume the proportionality $R \propto B$, so that Eq.(17) rewrites as

$$K = \frac{\sigma_b^2}{\sigma_b^2 + \sigma_{obs}^2} \cdot I, \tag{18}$$

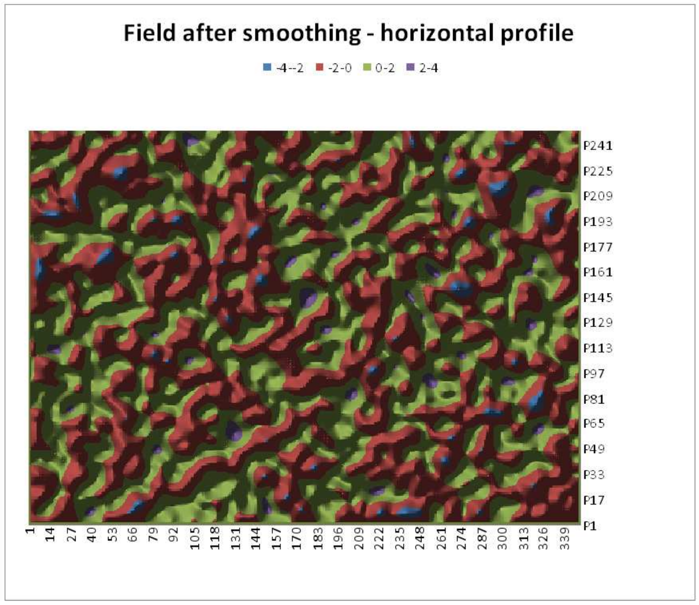

Figure 2: A horizontal cross-section of the observation noise.

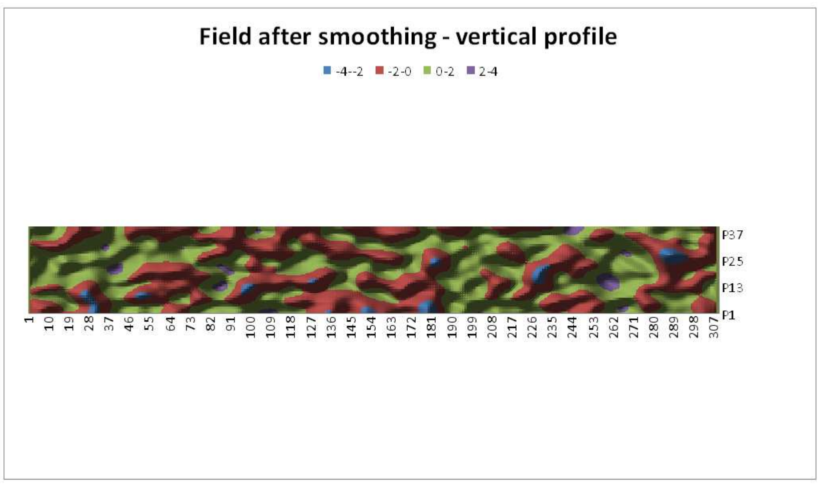

Figure 3: A vertical cross-section of the observation noise.

where σ_b is the background-error standard deviation and σ_{obs} the observation-error standard deviation.

This implies that the analysis decouples into a series of scalar (grid-point-wise) analyses. So, the analysis scheme is here extremely simple and fast.

After T, u, v, q fields are analyzed, we compute the p field by integrating the hydrostatic equation starting from the top model level, where COSMO is coupled with the global driving model. All computations are performed on the native COSMO grids.

5.3.5 Forecast

6-h forecasts at each assimilation cycle start from the above analyses and are performed with the unperturbed COSMO model — exactly as in the real world. The upper and lateral boundary conditions are build from the sequence of global driving-model analyses and 3-h forecasts with linear interpolation within 3-h time intervals.

5.4 Estimation of instantaneous ME from finite-time forecast-minus-observed tendencies. The experimental setup

Finite-time ME in T, u, v are checked. The length of the finite-time tendency Δt ranges from 1 h to 6 h. Recall that the ME are constant in space and time: within one cycle in the assimilation mode and for the whole forecast in the forecast mode.

ME temperature and wind components standard deviations are set up to be on two levels: realistic (1 K per day for T and 2 m/s per day for u and v) and unrealistically high (5 times larger: 5 K per day and 10 m/s per day, respectively).

Observation error standard deviations are set up again on two levels: realistic (1 K and 2 m/s for temperature and each of the two wind components, respectively) and unrealistically low (0.1 K for T and 0.2 m/s for u and v).

The intention with specifying unrealistically large ME and unrealistically low observation errors was to seek the condition under which ME *can be* estimated using observations.

5.5 ME observability criterion

Equation (15) shows that finite-time ME $\breve{\varepsilon}$ is observable through the difference of finite-time model tendencies and observed tendencies if

$$\breve{\varepsilon} \approx \Delta X^m - \Delta X^o. \tag{19}$$

We measure the degree of error involved in this approximate equality by the relative error defined as

$$r := \frac{\|\Delta X^m - \Delta X^o - \breve{\varepsilon}\|}{\|\breve{\varepsilon}\|}. \tag{20}$$

The norm here is the standard L^2 norm, where involves averaging over the central third of the domain in each of the three spatial dimensions and over assimilation cycles.

With our constant imposed ME $\varepsilon = \varepsilon_0$, the dift $\breve{\varepsilon}$ is simply $\breve{\varepsilon} = \varepsilon_0 \cdot \Delta t$.

Thus, for all assimilation experiments, we calculate r and, if $r \le 0.3$, we conclude that ME is observable and if $r > 0.3$ ME is not observable.

We check the three forecast tendency lengths $\Delta t = 1$, 3, and 6 h.

5.6 Results: Assessment of the ME observability errors

With the above realistic both ME and observation errors, the ME relative observability error r (see Eq.(20)) appears to be unacceptably high for all three tendency lengths examined: 1, 3, and 6 h. So, we don't display those results and turn to less realistic setups with better ME observability (smaller observation errors and/or larger ME).

Table 1 shows the values of r for the *unrealistic* case when observation errors are set to the very small levels: 0.1 K for temperature and 0.2 m/s for each wind component. Note that for technical reasons, in this and the next table, some cells are not filled in. We believe the presented results are quite enough to judge whether the selected ME estimation approach is viable.

Specifically, from Table 1, we see that even for unrealistically small observation errors (OE) and despite all degrees of freedom are observed for the four fields (T, u, v, q), the relative ME observability errors r are unacceptably high (see the first horizontal data section "OE small" in Table 1).

Table 1: RMS relative errors of ME observability. The unrealistic case (observation errors are small or zero; ME are realistic)

OE	Field	$\Delta t = 1$ h	$\Delta t = 3$ h	$\Delta t = 6$ h
OE small	T	> 1		0.68
	u	> 1		2.7
	v	> 1		3.4
OE=0	T	1.0	0.58	0.46
	u	1.2	1.8	1.6
	v	1.4	1.5	2.0
Fc starts	T	0.28	0.30	0.33
from	u	0.33	0.75	0.99
truth	v	0.35	0.69	1.20

The second horizontal data section in Table 1 (OE=0) presents the values of r for the case when observations (both in the assimilated observations and the observations used to compute the observed tendencies ΔX^o) are perfect. In this case, the observability error stems from, first, initial errors in the unobserved fields, second, from errors in the hydrostatically recovered pressure field, and third, from the ME-induced trajectory drift effect, δ_{me}. We see that even for perfect observations, r never becomes acceptable (i.e. is never less than $r = 0.3$) for neither of the three fields (T, u, v) and neither of the three tendency lengths (1, 3, 6 h).

Three points are worth noting here. First, T appears to be less badly observable than both u and v. This is discussed in the Interpretation section below. Second, for winds, r increases with the increasing Δt. Third, for temperature, the reverse Δt dependence occurs. This latter outcome can be assigned to the absence of wind-mass balancing in our simplistic analysis.

The lowermost horizontal data section of Table 1 corresponds to the setup in which no assimilation is, in fact, present and the forecasts start directly from the 'truth'. In this case, the ME observability error is caused only by the δ_{me} error component. We see that here, *temperature* ME observability errors are close to acceptable for all Δt, whereas *wind* ME errors are nearly acceptable only for $\Delta t = 1$ h. An interpretation of this difference in observability between temperature and winds will be given below in section .

Next, we examine the *extremely unrealistic* case — when OE are unrealistically low (or absent) whereas ME are unrealistically high, see Table 2. Qualitatively, the results here are largely the same as those presented in Table 1. This implies that nonlinearity does not play a significant role in ME observability in finite-time tendencies.

Further, we present typical plots of forecast-minus-observed tendencies $(\Delta X^m(t) - \Delta X^o(t))$ as well as expected tendencies $(\varepsilon_0 \cdot (t - t_0))$ as functions of lead time t. We consider here the case when forecasts start from the 'truth', so that only the δ_{me} error component plays a role here. Note that we show the plots for an arbitrarily selected grid point and at an arbitrary cycle of our intermittent data assimilation with "synthetic" observations.

Fig. 4 shows that for T, with perfect initial conditions, the 'target' $\varepsilon_0 \cdot (t - t_0)$ finite-time tendency error <u>is</u> roughly reproduced, albeit with an error, for the lead times up to about 12 h. Fig. 5 demonstrates that the u-wind ME observability time span is not longer than 2 h. As for the v-wind, the ME turn out to be observable during a period of time as short as about 1 h (see Fig. 6).

Next, we note that we have checked different ME amplitudes and found (somewhat sur-

Table 2: RMS relative errors of ME observability. The extremely unrealistic case (observation errors are small or zero; ME are unrealistically high)

OE	Field	$\Delta t = 1$ h	$\Delta t = 3$ h	$\Delta t = 6$ h
OE small	T	0.80	0.41	0.35
	u	1.75	0.98	1.09
	v	2.26	1.38	1.42
OE=0	T			0.34
	u			1.02
	v			1.30
Fc starts	T	0.27		0.34
from	u	0.26		0.98
truth	v	0.34		1.26

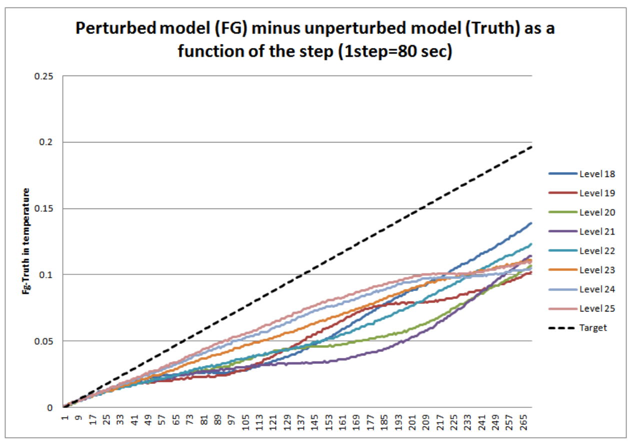

Figure 4: Forecast tendency T errors at different model levels vs. the integrated ME (dashed) at an arbitrary grid point

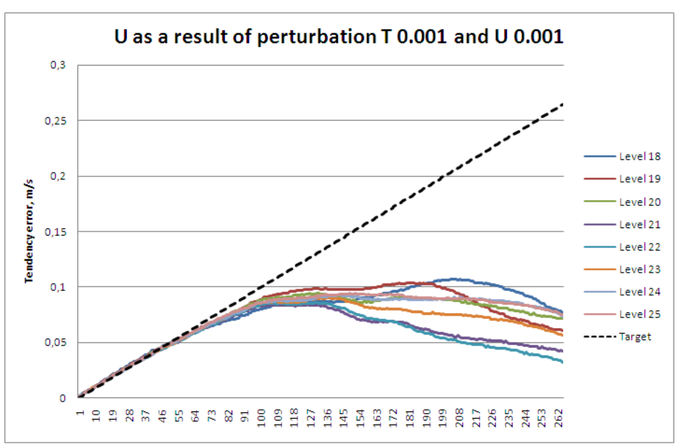

Figure 5: Same as Fig.4 except for u.

prisingly) that the ME observability does not depend much on the ME amplitude. This is confirmed by the relative errors presented in the lowermost horizontal sections of tables 1 and 2. So, linear mixing of the flow seems to be of primary importance, not its non-linearity.

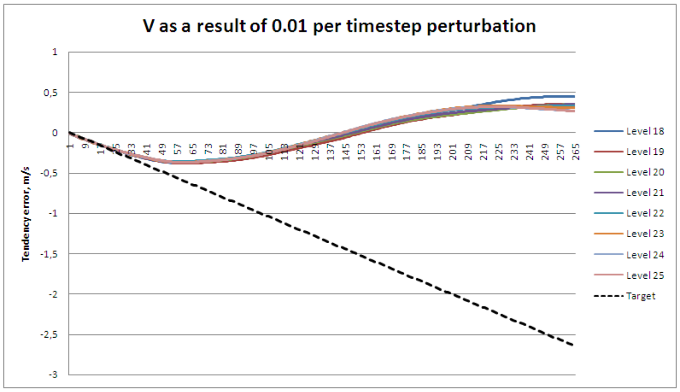

Figure 6: Same as Fig.4 except for v.

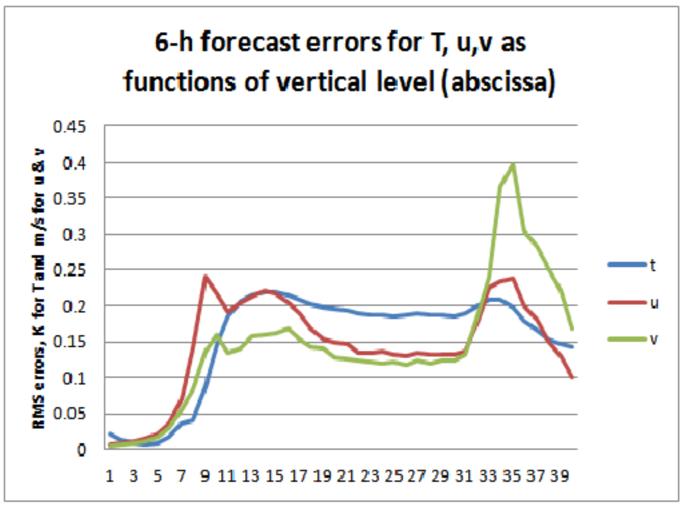

Figure 7: 6-h forecast RMS errors due to ME as functions of the vertical model level (realistic ME).

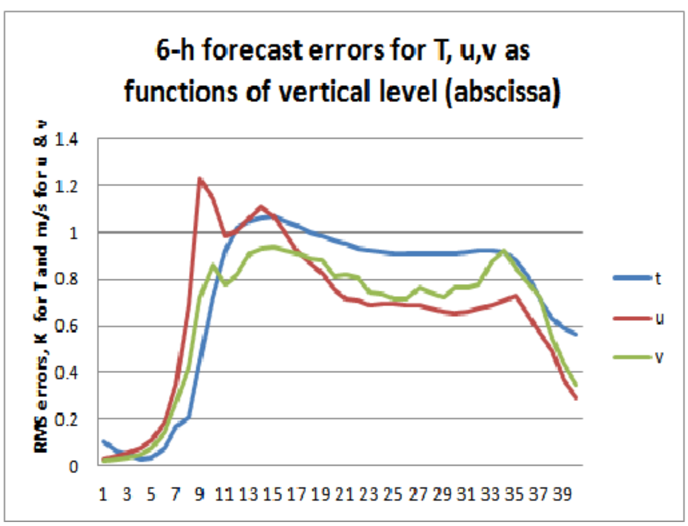

Figure 8: 6-h forecast RMS errors due to ME as functions of the vertical model level (unrealistically high ME).

Finally, we display standard deviations of the ME-induced forecast errors themselves (the forecasts start from the 'truth' and last for 6 h) as functions of altitude. Figs. 7 and 8 show that near the boundaries, especially near the upper boundary, the impact of ME is significantly reduced. This implies that introducing perturbations into boundary conditions is inevitable if we wish to obtain realistic forecast ensemble spread within the whole model atmosphere. The same conclusion is certainly valid for the lateral boundaries (not checked).

5.7 Conclusions drawn from the experiments

With the existing level of observation errors and ME, even the perfect observational coverage does not allow us to perceive the imposed most easily estimable constant-ME in finite-time forecast tendencies. The noise from initial errors (including the unobserved fields, like hydrometeors and vertical wind) and from the ME-induced trajectory drift (mixing the ME signal with the fields themselves) appears to be too high for the tested ME estimation approach to be useful.

5.8 Interpretation of the experimental results

Here, we discuss, using simple models, why for winds, ME disappear in the forecast tendency errors much more quickly than for temperature. We also check whether it is worth switching from Eulerian to Lagrangean tendencies in our ME estimation attempts.

The aim of this section is to theoretically verify that the above experimental results are, at least qualitatively, meaningful. This will make our conclusions more credible. Without any theoretical analysis, we would be less confident that the results of the experiments are really relevant for the problem at hand and are not caused by a program bug or other artifacts.

5.8.1 Temperature ME

Let the forecast model be the 1-D advection equation with a pre-specified and exactly known advection velocity c:

$$T_t^m + cT_x^m = 0, \tag{21}$$

where subscripts t and x stand for time and space partial derivatives, respectively, and the superscript m means "model" (forecast).

The 'truth' is, in accord with Eq.(2),

$$T_t^t + cT_x^t = -\varepsilon, \tag{22}$$

where the superscript t means the 'truth".

Let, further, the model (forecast) starts, at $t = t_0$, from the 'truth'. Then, the forecast-error (i.e. $T' := T^m - T^t$) equation, obtained by subtraction of Eq.(22) from Eq.(21), satisfies the following equation

$$T_t' + cT_x' = \varepsilon, \tag{23}$$

with the initial condition

$$T'(t_0) = 0. \tag{24}$$

Knowing $c = c(t, x)$, we easily solve the initial problem Eq.(23)–(24) using the method of characteristics:

$$\frac{\mathrm{d}T'}{\mathrm{d}t} = \varepsilon, \tag{25}$$

where $/\dot{\mathrm{d}}t$ denotes the full derivative along the physical-space trajectory defined by the equation

$$\frac{\mathrm{d}x}{\mathrm{d}t} = c(t, x) \tag{26}$$

and the initial condition

$$x(t_0) = x_0. \tag{27}$$

Integrating Eq.(25) along the advection trajectory (the characteristic) yields (recall, for zero initial error T')

$$T'(t, x) = \int_{t_0}^{t} \varepsilon(t, x(t, x_0))\,\mathrm{d}t \equiv \breve{\varepsilon}. \tag{28}$$

For constant in space and time ε, Eq.(28) implies that the forecast tendency error *does reproduce* $\breve{\varepsilon}$. This is in concert with the above experimental result: temperature ME are better observable from finite-time tendency errors than wind ME. Now, let us turn to the latter.

5.8.2 Wind

The principal difference from the temperature case it that wind is both the advected quantity and the advection velocity itself. Therefore, let us consider the non-linear advection equation (again, in 1-D) for the u wind component:

$$u_t^m + u^m u_x^m = 0, \tag{29}$$

$$u_t^t + u^t u_x^t = -\varepsilon. \tag{30}$$

Expressing $u^t = u^m - u'$, subtracting Eq.(30) from Eq. (29), and neglecting, for simplicity of the analysis, the non-linear (w.r.t. the perturbation u') term $u'u_x'$, we obtain

$$u_t' + u^m u_x' + u' u_x^m = \varepsilon \tag{31}$$

or, rearranging the terms,

$$u_t' + u^m u_x' = -u' u_x^m + \varepsilon. \tag{32}$$

Comparing this equation with its counterpart for temperature, Eq. (23), we see one single qualitative difference: the presence of the term $(-u'u_x^m)$ in the r.h.s. of the equation. To understand how it impacts the solution, let us suppose that $u_x^m \equiv g = const$ (i.e. u^m is a linear function of x only). Then, we have

$$\frac{\mathrm{d}u'}{\mathrm{d}t} = -gu' + \varepsilon. \tag{33}$$

Here, as before for temperature, $\mathrm{d}/\mathrm{d}t$ denotes the full derivative along the physical-space trajectory defined by the equation

$$\frac{\mathrm{d}x}{\mathrm{d}t} = u^m. \tag{34}$$

Along any trajectory defined by Eq.(34), with zero initial condition $u'(t = 0) = 0$, Eq.(33) is easily solved:

$$u'(t, x(t, x_0)) = \exp(-gt) \int_{t_0}^{t} \exp(g\tau)\varepsilon(\tau, x(\tau, x_0))\mathrm{d}\tau. \tag{35}$$

In this equation, the important feature is that in the course of integration, ε is multiplied by $\exp(g\tau)$, i.e. ε is *distorted*. This distortion makes the finite-time forecast tendency error less and less related to the integrated ME. We may, thus, speculate that it is this effect that makes *wind* ME less observable than temperature ME.

As a final remark here, we note that Eq.(35) implies that the ME observability time scale can be assessed as $g^{-1} = (u_x^m)^{-1}$, the flow time scale. For meso-scale flows, this time scale is of the order of hours, and so is, thus, the ME observability time.

5.8.3 Lagrangean vs. Eulerian tendencies

Let us consider the temperature advection equation, Eq.(21), and assume, in contrast to Eq.(22), that temperature ME is due to mis-specified advection velocity c as well as due to the temperature ME:

$$c \equiv c^m = c^t + c' : \tag{36}$$

$$T_t^m + c^m T_x^m = 0 \tag{37}$$

$$T_t^t + c^t T_x^t = -\varepsilon \tag{38}$$

$$T^m = T^t + T'. \tag{39}$$

Expressing $c^t = c^m - c'$ and $T^t = T^m - T'$, substituting them into Eq.(38) and subtracting the resulting equation from Eq.(37) yields:

$$T_t' + c^m T_x' + c' T_x^m - c' T_x' = \varepsilon. \tag{40}$$

In this equation, with the *Eulerian* tendency, T_t', is contaminated by the three terms: $c^m T_x' + c' T_x^m - c' T_x'$, whereas with the *Largangean* tendency, $T_t' + c^m T_x'$, only by the two terms: $c' T_x^m - c' T_x'$. Now, we claim that the difference between the two cases is not dramatic. Indeed, the 'gain' $c^m T_x'$ is comparable in magnitude with one remaining term, $c' T_x^m$. This can be seen by assuming realistic wind and temperature errors, and realistic natural variability standard deviations and length scales (not shown).

So, we conclude that, although switching from Eulerian to Lagrangean tendencies can reduce the impact of forecast errors due to initial errors propagated by advection, the contamination of the finite-time tendency errors by the ME-induced trajectory drift can hardly be reduced.

We note here that, in addition, advection error propagation is only part of the initial-error evolution. Further, in the above analysis, we did not take in to account the vertical advection associated with much larger errors in w. Finally, we do not have a dense enough in-situ observation network to estimate the Lagrangean tendencies (using remote sensing data is doubtful in view of their possible spatially and temporally correlated observation errors).

Summarizing this Eulerian/Lagrangean subsubsection, turning to Lagrangean tendencies would imply only a minor improvement and thus is not worth trying.

Summarizing the interpretational subsection , we conclude that the experimental results do not contradict to the theoretical conclusions/speculations.

Summarizing the whole experimental section, we conclude that the observation-based ME estimation endeavor has failed. This failure is confirmed by theoretic considerations.

6 Conclusions

The above experimental results unequivocally imply that perceivable (through in-situ observations) finite-time tendency errors are too heavily contaminated by both initial errors and

ME-induced trajectory drift errors, so that the signal-to-noise ratio is well below 1. Without having, thus, any real access to (time-integrated) true ME, any estimator that uses the difference between the model tendency and the observed tendency as a proxy to the true ME, would inevitably fail. In principle, one can imagine a much more sophisticated approach that attempts to allow for the (stochastic) distortion of ME by the chaotic atmosphere flow. But a realization of such an approach would be very difficult and time consuming, without any guarantee of success.

It is worth stressing that not only *instantaneous* ME are not recoverable from finite-time forecast-minus-observed tendencies, but *finite-time* ME are not recoverable either. Indeed, in our experiments we imposed constant in space and time ME.

So, with existing routine observations, an observations based ME estimation technique appears to be not feasible.

Appendix. Assessment of the ε-induced trajectory drift

Here, we wish to understand whether or not the quantity

$$\delta_{me} := \int_{t_0}^{t_0+\Delta t} F(X^{mt})dt - \int_{t_0}^{t_0+\Delta t} F(X^t)dt \tag{41}$$

(where the model forecast X^{mt} starts from the truth, $X^{mt}(t_0) = X^t(t_0)$) can be neglected in comparison with the time integrated ME:

$$\breve{\varepsilon} := \int_{t_0}^{t_0+\Delta t} \varepsilon(t)\, \mathrm{d}t. \tag{42}$$

To set up the problem, we, first, suppose that Δt is small enough for $X^{mt}(t)$ to remain close to $X^t(t)$ in the sense that the first-order Taylor expansion around X^{mt} can be applied:

$$F(X^t) = F(X^{mt}) - A \cdot \delta X, \tag{43}$$

where A is the Jacobian $\partial F / \partial X$ and

$$\delta X := X^{mt} - X^t. \tag{44}$$

Next, for simplicity of the analysis, we postulate that the operator A in Eq.(43) can be taken constant within $t \in (t_0, t_0 + \Delta t)$. Then the discrepancy δ_{me} becomes

$$\delta_{me} = \int_{t_0}^{t_0+\Delta t} A \cdot \delta X(t)\, \mathrm{d}t = A \int_{t_0}^{t_0+\Delta t} \delta X(t)\, \mathrm{d}t. \tag{45}$$

Now, we find $\delta X(t)$. From

$$\frac{dX^{mt}}{dt} = F(X^{mt}) \tag{46}$$

and

$$\frac{dX^t}{dt} = F(X^t) - \varepsilon, \tag{47}$$

we see that δX satisfies the equation

$$\frac{d\delta X}{dt} = A \cdot \delta X + \varepsilon \tag{48}$$

supplemented with the initial condition $\delta X(t_0) = 0$.

It is easy to show that the solution to Eq.(48) with zero initial condition is

$$\delta X(t) = \exp(At) \int_{t_0}^{t_0+\Delta t} \exp^(-As)\varepsilon(s)\,\mathrm{d}s. \tag{49}$$

Now, we return to the discrepancy in question, δ_{me}, and substitute $\delta X(t)$ from Eq.(48) into Eq.(45):

$$\delta_{me} = A \int_{t_0}^{t_0+\Delta t} \exp(At)dt \int_{t_0}^{t_0+\Delta t} \exp(-As)\varepsilon(s)\,\mathrm{d}s. \tag{50}$$

Let us evaluate Eq.(50) in the asymptotic limit $\Delta t \to 0$. For small enough Δt, $\varepsilon(s) \sim \varepsilon(t_0) \equiv \varepsilon_0$ and $\exp(At) \sim I + A(t - t_0)$, so that

$$\delta_{me} \sim A\varepsilon_0 \Delta t^2. \tag{51}$$

We roughly assess the application of A as multiplication by its time scale (the dynamical time scale T_{dyn}), thus Eq.(51) becomes

$$\delta_{me} \sim \varepsilon_0 \frac{\Delta t^2}{T_{dyn}}. \tag{52}$$

We note that the discrepancy r is important if it's comparable with $\breve{\varepsilon} \approx \varepsilon_0 \Delta t$. We see that the 'noise-to-signal ratio' is

$$\frac{\delta_{me}}{\breve{\varepsilon}} \approx \frac{\Delta t}{T_{dyn}}. \tag{53}$$

This equation suggests that we are allowed to neglect δ_{me} if $\Delta t \ll T_{dyn}$. On the meso scale, with T_{dyn} as small as hours, the 12-h tendencies appear to fail to capture the ME structure. Δt needs to be very small, perhaps, of the order of 1 h or less.

References

[1] Orrell, D., Smith, L., Barkmeijer, J., and T.N.Palmer, 2001: Model error in weather forecasting. *Nonlinear Processes in Geophysics*, v.8, **357-371**.

[2] Reynolds, C.A., Webster, P.J. and E. Kalnay, 1994: Random error growth in NMC's global forecasts. *Mon. Wea. Rev.*, v. 122, **1281-1305**.

COSMO Data Assimilation. Applications for Romanian Territory

Amalia IRIZA[1,2], Rodica Claudia DUMITRACHE[1], Cosmin Dănuţ BARBU[1], Aurelia Lupaşcu[1], Bogdan Alexandru MACO[1]

1: National Meteorological Administration
Sos. Bucuresti- Ploiesti, nr.97, Bucharest, Romania
2: Faculty of Physics, University of Bucharest,
PO Box Măgurele 11, Măgurele, Bucharest, Romania
amalia.iriza@meteoromania.ro

1 Introduction

In the context of numerical weather prediction, the requirements for a data assimilation system are dependent on the purpose and main characteristics of the numerical model for which they are used as initial conditions. The COSMO model in operational configuration is characterized by high resolution on a limited domain, with the main purpose of producing accurate short period numerical weather forecasts. One of the main concerns in improving the quality of numerical weather forecasts is the development of data assimilation techniques and proper usage of various types of observation data.

Data assimilation is an analysis technique in which the observed information is accumulated into the model state by taking advantage of consistency constraints with laws of time evolution and physical properties ([1]).

The purpose of this paper is the presentation of some results regarding the operational data assimilation in the numerical weather prediction model COSMO for the Romanian territory. Taking into account the availability of TEMP, PILOT and RADAR observation data, the necessary procedures to assimilate the data at both model resolutions ($7km$ and $2.8km$), for the Romanian territory were made.

In order to study the influence of assimilation for different observation types on the numerical weather forecast of the COSMO model for the domain of interest, the model was run in 4 different configurations using the available data.

Future plans include the usage in the operational activity of the data assimilation for TEMP, PILOT and RADAR observations in the COSMO model run for Romanian territory.

2 Methods and Data

The COSMO model is run operationally in the National Meteorological Administration since 2005, on a domain which covers the Romanian territory with 201×177 grid points for $7km$ horizontal resolution and 361×291 grid points for $2.8km$ horizontal resolution. Starting with 2009, data assimilation of SYNOP observations for all Romanian meteorological stations is run operationally.

For the assimilation of SYNOP, TEMP and PILOT observation, the nudging technique was used. The nudging scheme is based on the experimental nudging assimilation scheme developed for the former hydrostatic model DM and its Swiss version SM, and adapted, refined and extended in various aspects for the COSMO model. This technique is used in the COSMO model for the assimilation of most observation data (such as SYNOP, SHIP, RADAR Doppler, BUOY, AIRCRAFT and so on) except for RADAR observations ([2]).

For RADAR-derived precipitation rates, a Latent Heat Nudging scheme is used, which computes additional temperature and humidity increments at each model column independently from each other and is used only for convection-permitting model configurations (horizontal mesh width $\leq 3km$) ([2]).

Taking into account the data availability of TEMP, PILOT and RADAR observation data, a series of preprocessing procedures were made in order to assimilate the data for both horizontal resolutions ($7km$ and $2.8km$) of the COSMO model.

The TEMP and PILOT observation data for Romanian stations were obtained in BUFR format. The RADAR data were available in NetCDF format. TEMP and PILOT data for meteorological stations outside the Romanian territory (inside the COSMO domain, table 1) were received for the test case by courtesy of Davide Cesari from ARPA-SIMC (Agenzia Regionale per la Protezione Ambientale Emilia Romagna Servizio Idro Meteo Clima).

Station code	Location	Country
11035	Vienna / Hohe Warte	Austria
12425	Wroclaw / Maly Gad	Poland
13275	Belgrade Kosutnja	Serbia
14240	Zagreb/Maksimir	Croatia
16622	Thessaloniki	Greece
33393	L Viv	Ukraine

Table 1: Meteorological stations outside the Romanian territory (inside the COSMO domain).

The data format for the SYNOP, TEMP and PILOT observations required by the data assimilation nudging scheme is NetCDF. The necessary data format for the RADAR observation files is GRIB1.

For the conversion of the observation files from BUFR format to NetCDF format, the following additional software packages were used (by courtesy of Davide Cesari at ARPA-SIMC):

- wreport: a C++ library for decoding the BUFR data format;
- DB-all.e: utilities software for conversions from BUFR or NetCDF formats in WMO (World Meteorological Organization) standard format;
- bufr2netcdf: a library for conversions from standard BUFR to the NetCDF format required by the COSMO model.

For the conversion of the RADAR data from NetCDF to GRIB1 format and the interpolation in the COSMO grid at $2.8km$ resolution a procedure was developed based on the NCO (NetCDF Operator) software. The initial domain of the RADAR observations is 668×772 grid points, with a horizontal resolution of 0.0129316229208 degrees longitude and 0.00898306010458 degrees latitude. Observations are assimilated in the grid point closest to the location of the measurements. Observation processing includes (apart from the reading) spatial and temporal assignation of the observations to the model space, unifying TEMP (or PILOT) radiosonde parts in single complete profiles, applying bias corrections and so on ([2]).

3 Case Study

In order to analyze the influence of the data assimilation of TEMP, PILOT and RADAR observations, the COSMO model was run in various configurations for the 16^{th} of October $2012 - 00UTC$. The COSMO model was run in the following configurations:

- COSMO-RO-7km resolution with SYNOP data assimilation (C1);
- COSMO-RO-7km resolution with SYNOP-TEMP-PILOT data assimilation (C2);
- COSMO-RO-2.8km resolution with SYNOP-TEMP-PILOT and RADAR data assimilation (C3);
- COSMO-2.8km without data assimilation (C4).

The results of the COSMO model run in the 4 configurations mentioned before were compared as follows:

- the forecast from the COSMO-RO-7km with data assimilation for SYNOP observations against the forecast from the COSMO-RO-7km with the assimilation of the SYNOP, TEMP and PILOT data;
- the results from the COSMO-RO-2.8km without data assimilation against the forecast from the COSMO-RO-2.8km with the assimilation of the SYNOP, TEMP, PILOT and RADAR data.

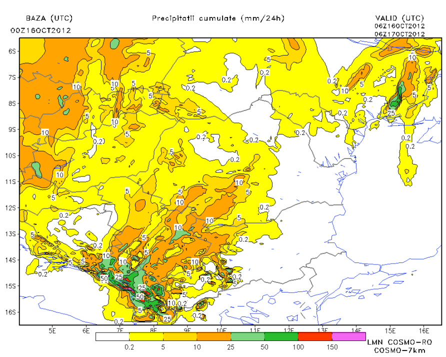

(a)

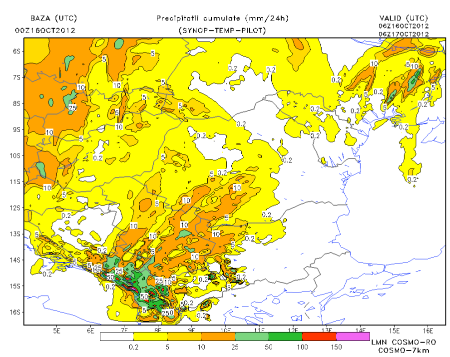

(b)

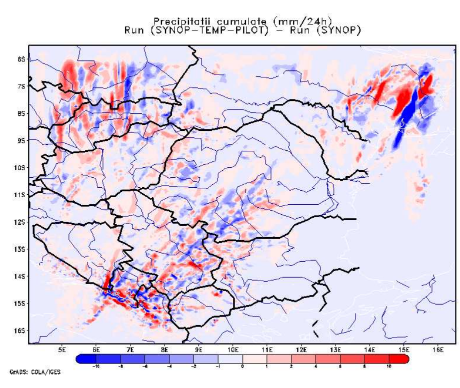

(c)

Figure 1: 16.10.2012 (00 UTC): COSMO-7km forecast for cumulated precipitation - 24h a) SYNOP; b) SYNOP, TEMP and PILOT; c) Difference (SYNOP-TEMP-PILOT) (SYNOP).

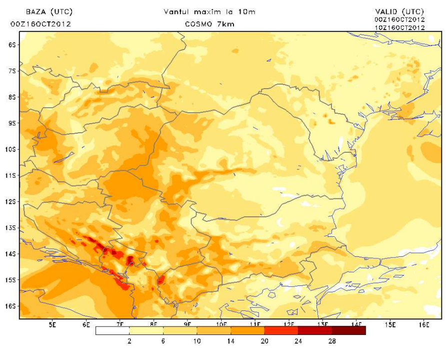

(a)

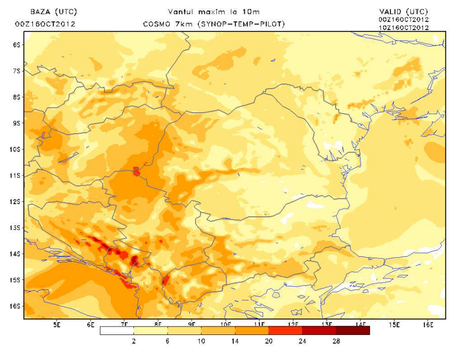

(b)

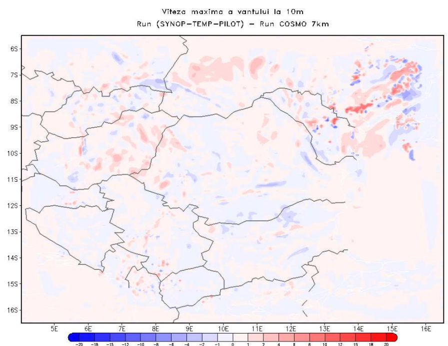

(c)

Figure 2: 16.10.2012 (00 UTC): COSMO-7km forecast for maximum wind speed - 10UTC a) SYNOP; b) SYNOP, TEMP and PILOT; c) Difference (SYNOP-TEMP-PILOT) (SYNOP).

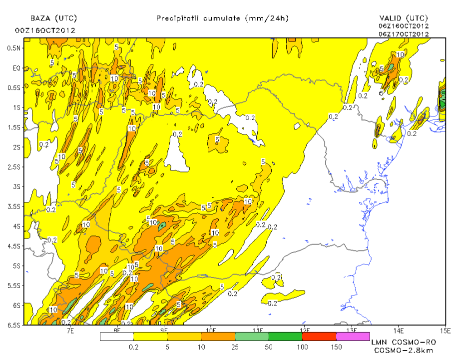

(a)

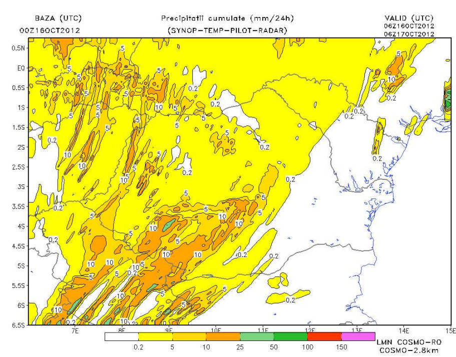

(b)

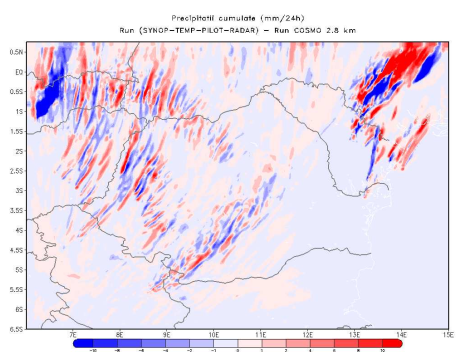

(c)

Figure 3: 16.10.2012 (00 UTC): COSMO-2.8km forecast for cumulated precipitation - 24h a) no data assimilation; b) SYNOP, TEMP, PILOT and RADAR; c) Difference (SYNOP-TEMP-PILOT-RADAR) - (COSMO-2.8km).

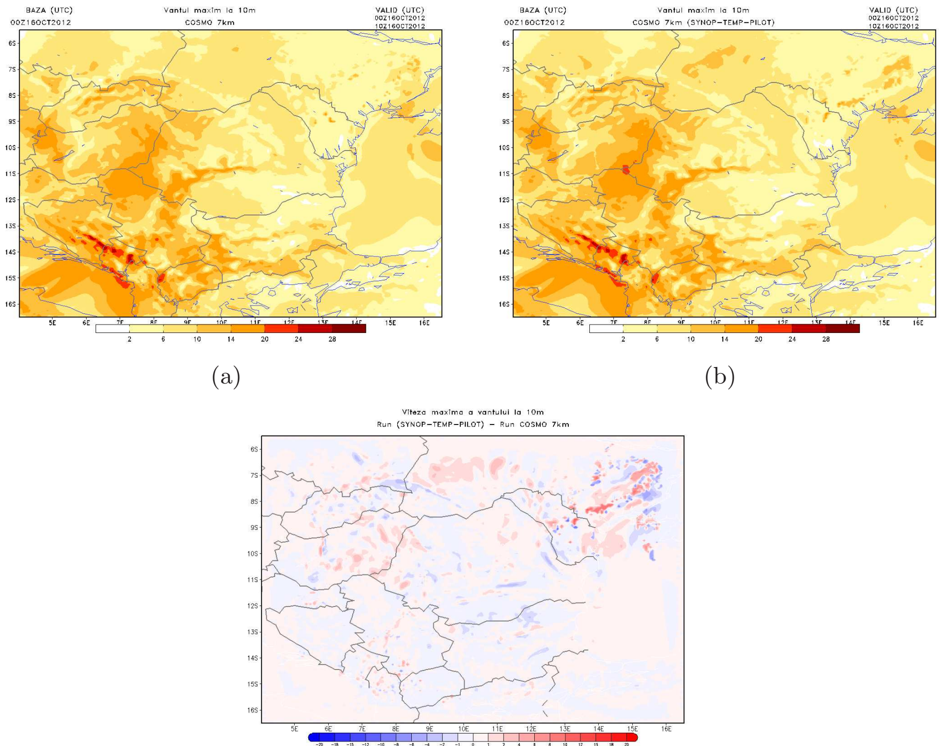

(a) (b)

(c)

Figure 4: 16.10.2012 (00 UTC): COSMO-2.8km forecast for maximum wind speed - 07UTC a) no data assimilation; b) SYNOP, TEMP, PILOT and RADAR; c) Difference (SYNOP-TEMP-PILOT-RADAR) - (COSMO-2.8km).

By analyzing the results of the COSMO model run with the configurations mentioned before, we can especially notice the influence of the assimilation of the vertical soundings in the forecast of the precipitation parameter. This can be observed mostly in the areas surrounding the location of the vertical soundings (fig. 1-3).

From the previous examples, for the COSMO run (configuration C3) we can observe the tendency of the model to overestimate and redistribute spatially the precipitation parameter in the immediate vicinity of the location of the vertical soundings (fig. 3).

If we analyze the forecast of the maximum wind speed we see that the COSMO model in configuration C2 (with vertical soundings data assimilation) overestimates the values of this parameter compared to the model run in configuration C1 (only SYNOP data), again mostly in the areas closest to the location of the vertical soundings (fig. 2).

For the COSMO-2.8km model run, the values of the maximum wind speed parameter forecasted by the model in configuration C3 (with SYNOP, TEMP, PILOT and RADAR observations) are also overestimated compared to the values forecasted by running the model without any data assimilation, especially for the western and central areas of the domain (fig. 4).

4 Conclusions

Although the assimilation of various observation data in the COSMO numerical model can lead to significant improvement of the quality of forecasts, these adjustments cannot be analyzed and emphasized properly in just one case study.

Future plans include the usage in the operational activity of the data assimilation for TEMP, PILOT and RADAR observations in the COSMO model run for Romanian territory. The difficulties in concluding this task are mainly due to the difficult procedures necessary for the conversion of the observation data from the available data formats to the ones required by the model. Also, another inconvenient is the high computing time required for the preprocessing of the RADAR data to the model grid.

References

[1] Bouttier F., Courtier P. 1999: Data Assimilation Concepts and Methods. ECMWF Meteorological Training Course Lecture Series: 59

[2] Schraff C., Hess R. 2012: A Description of the Nonhydrostatic Regional COSMO Model. Part III: Data Assimilation. COSMO User Guide.

Implementation of TKE–Scalar Variance Mixing Scheme into COSMO

Ekaterina Machulskaya and Dmitrii Mironov

German Weather Service, Offenbach am Main, Germany

1 Introduction

We report on the development and testing of a turbulence kinetic energy – scalar variance (TKESV) mixing scheme, and its implementation into the COSMO model. A summary of results obtained within the framework of the COSMO Priority Project UTCS is given, including a brief outline of the TKESV scheme, a discussion of the scheme performance in various clear and cloudy boundary-layer regimes as revealed by off-line single-column tests, details of the implementation of the new scheme into COSMO, and some results from numerical experiments with the full-fledged COSMO model. Future challenges are briefly discussed.

In what follows, standard notation is used, where t is the time, x_i are the space co-ordinates, and u_i are the velocity components (the subscript "3" refers to the vertical direction). The angle brackets denote a (grid-box) mean quantity, and a prime denotes a fluctuation about the mean.

2 Outline of the TKESV scheme

A turbulence kinetic energy – scalar variance mixing scheme for the COSMO model is developed. The scheme is formulated in terms of two scalars that are approximately conserved for phase changes in the absence of precipitation. These are the total water specific humidity q_t and the liquid water potential temperature θ_l. The TKESV scheme carries prognostic transport equations for the turbulence kinetic energy (TKE), $\frac{1}{2}\left\langle u_i'^2\right\rangle$, for the variances of the scalar quantities, $\left\langle q_t'^2\right\rangle$ and $\left\langle \theta_l'^2\right\rangle$, and for their covariance, $\langle q_t'\theta_l'\rangle$. The other second-order moments, viz., the Reynolds stress, $\left\langle u_i'u_j'\right\rangle$, and the scalar fluxes, $\langle u_i'q_t'\rangle$ and $\langle u_i'\theta_l'\rangle$, are determined through the algebraic diagnostic expressions obtained by neglecting the time-rate-of-change and the triple correlations terms in the respective transport equations. Notice that $\left\langle q_t'^2\right\rangle$, $\left\langle \theta_l'^2\right\rangle$ and $\langle q_t'\theta_l'\rangle$ actually characterize the potential energy of fluctuating fields, i.e. the turbulence potential energy.

A one-dimensional transport equation for the covariance of two generic scalars a and b reads

$$\frac{\partial \langle a'b'\rangle}{\partial t} = -\left\langle u_3'a'\right\rangle \frac{\partial \langle b\rangle}{\partial x_3} - \left\langle u_3'b'\right\rangle \frac{\partial \langle a\rangle}{\partial x_3} - \frac{\partial}{\partial x_3}\left\langle u_3'a'b'\right\rangle - \epsilon_{ab}, \tag{1}$$

where $\epsilon_{ab} = (\kappa_a + \kappa_b)\left\langle \frac{\partial a'}{\partial x_i}\frac{\partial b'}{\partial x_i}\right\rangle$ is the molecular destruction (dissipation) rate of the co-variance $\langle a'b'\rangle$, and κ_a and κ_b are the molecular diffusivities for the quantities a and b, respectively. The transport equations for the variances of q_t and θ_l and for their covariance are obtained from Eq. (1) by setting $a = b = q_t$, $a = b = \theta_l$, and $a = q_t$ and $b = \theta_l$, respectively.

The turbulent transport terms in the scalar (co-)variance equations, i.e. the divergence of the velocity-scalar triple correlations as given by the third term on the right-hand side of Eq. (1), are parameterized through advanced "diffusion+advection" formulations that account for the skewed nature of convective motions [12]. The scalar skewness is obtained from its own transport equation where closure assumptions for the unknown terms are formulated with due regard for non-Gaussianity of fluctuating fields [5, 6]. The turbulent transport term in the TKE equation (the divergence of the velocity-velocity triple correlation and the pressure-velocity correlation) is parameterized through a down-gradient diffusion formulation. The pressure scrambling terms in the Reynolds-stress and scalar-flux equations are parameterized with due regard for turbulence anisotropy. The dissipation terms in the TKE and in the scalar (co-)variance equations are parameterized through relaxation approximations in terms of dissipation time scales. The various time scales, viz., the dissipation time scales in the TKE and scalar (co)-variance equations and the return-to-isotropy time scales in the Reynolds-stress and scalar-flux equations, are set proportional to each other and are expressed in terms of turbulence length scale and the TKE. The formulation for the turbulence length scale accounts for the effect of static stability. A statistical cloud scheme is used to parameterize the effect of sub-grid scale (SGS) condensation (cloudiness) on the buoyancy production of TKE. A Gaussian scheme [20] modified to account, in a very approximate way, for the skewness of temperature and humidity fields [2] is utilized.

A detailed description of the TKESV scheme will be given in subsequent publications. An extended discussion of turbulence parameterization schemes used in numerical models of the atmosphere is given in [11].

It should be emphasized that within the framework of the current COSMO-model turbulence scheme [17, 18, 1], the time-rate-of-change and the turbulent transport terms are retained in the TKE equation only, whereas all other second-order moments, including scalar (co-)variances, are determined from the algebraic diagnostic expressions. As a consequence, the expressions for the scalar fluxes do not include non-gradient terms and do not allow for up-gradient heat transfer that is known to occur in many convective flows, e.g. in the cloud-free convective planetary boundary layer (PBL) or in the sub-cloud layer of cloud-topped PBLs. This can be readily verified by neglecting the left-hand side and the third term on the right-hand side of Eq. (1) and setting $a = b = \theta$, where θ is the potential temperature (θ_l is equal to θ if clouds are absent). Then, $-\langle u_3'\theta'\rangle \,\partial \langle\theta\rangle/\partial x_3 - \epsilon_{\theta\theta} = 0$, indicating that the up-gradient hear transfer, when the temperature flux $\langle u_3'\theta'\rangle$ and the temperature gradient $\partial \langle\theta\rangle/\partial x_3$ have the same sign, would mean physically impossible negative temperature-variance dissipation rate. It should also be noted that the current COSMO-model turbulence scheme utilizes a Blackadar-type turbulence length scale formulation independent of static stability and a quasi-Gaussian statistical cloud scheme (see [1] for details).

3 Single-column tests

The TKESV scheme is tested through a series of single-column numerical experiments. Results from experiments with the TKESV and the TKE schemes are compared with observational and numerical large-eddy simulation (LES) data from dry convective PBL and from cloudy PBLs (BOMEX and ARM shallow cumulus cases and DYCOMS-II stratocumulus case).

Figure 1 shows vertical profiles of potential temperature in the shear-free dry convective PBL driven by the surface buoyancy flux. As revealed by comparison of model results with the LES data from [13], the TKESV scheme clearly outperforms the TKE scheme. A well-mixed character of (the bulk of) dry convective PBL and up-gradient heat transfer in the upper part of the mixed layer, where the potential-temperature gradient and the heat flux are both positive, are well reproduced by the TKESV scheme. The TKE scheme gives an excessive (negative) potential-temperature gradient in most of the PBL and is incapable of reproducing up-gradient heat transfer due to the use of down-gradient formulations for the scalar fluxes. In Fig. 2, vertical profiles of the TKE and of the potential-temperature variance computed with the TKESV and the TKE schemes are compared with the LES data. Results from numerical experiments with the TKESV scheme are in better agreement with data, although both schemes invite further improvements. Note that the TKE scheme yields zero potential-temperature variance in the upper part of the mixed layer where the temperature gradient changes sign. This result is spurious. It stems from the neglect of the third-order transport (diffusion) of scalar variances within the TKE scheme, where the scalar-variance equations are reduced (truncated) to the balance between the mean-gradient production and dissipation. The TKESV scheme does account for the third-order transport of scalar variances and yields better estimates of the variances throughout the convective PBL.

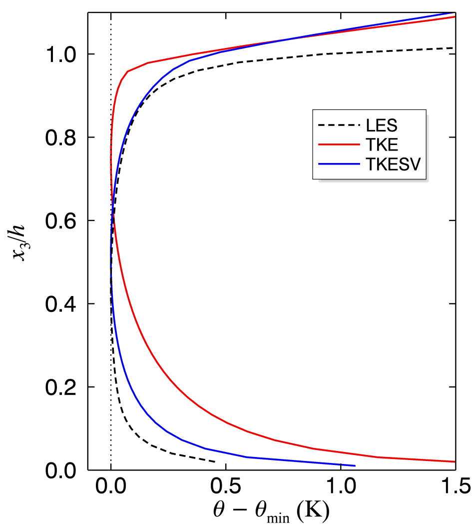

Figure 1: Potential temperature minus its minimum value vs. dimensionless height (h is the PBL depth) in the dry convective PBL. Black dashed curve shows LES data [13], and solid curves show results from numerical experiments with the TKE (red) and TKESV (blue) schemes.

The application of the TKESV and TKE scheme to the stratocumulus-topped PBL (DYCOMS-II test case, see [21]) reveal a similar performance of the two schemes. The TKESV scheme brings about minor improvements as to the scalar variances $\langle \theta_l'^2 \rangle$ and $\langle q_t'^2 \rangle$. In the shallow-cumulus regime (BOMEX test case, see [9, 19]), the application of the TKESV scheme leads to a better prediction of the scalar variances (Fig. 3), and to slight improvements with respect to the TKE, the vertical buoyancy flux and the mean temperature and humidity. A detailed analysis of results from numerical experiments suggests that the major difficulties in modelling the shallow cumulus regime are associated with the representation of the fractional cloud cover and its effect on the buoyancy flux. A quasi-Gaussian cloud parameterization used operationally in the COSMO model strongly overestimates fractional cloud cover in the cumulus-topped PBL. A modified parameterization with an ad hoc non-Gaussian correction [2] improves the fractional cloud cover. Both cloud parameterizations fail to accurately describe the effect of fractional cloudiness on the buoyancy flux (buoyancy production of TKE) in the shallow cumulus regime (although the parameterization with non-Gaussian correction does a slightly better job). A somewhat more sophisticated cloud scheme that accounts for non-Gaussian effects (e.g. through the skewness of scalar fields) is required.

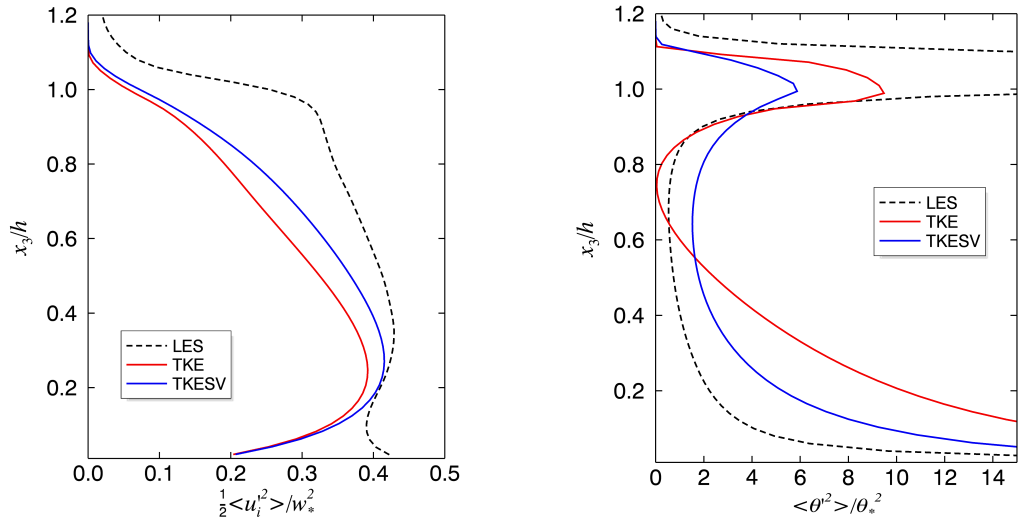

Figure 2: TKE (left panel) and potential temperature variance (right panel) vs. dimensionless height (h is the PBL depth) in the dry convective PBL. Black dashed curves show LES data [13], and solid curves show results from numerical experiments with the TKE (red) and TKESV (blue) schemes. Profiles are made dimensionless with the Deardorff [3, 4] convective scales of velocity, w_*, and temperature, θ_*.

4 Implementation into COSMO model

The TKESV scheme is implemented into the COSMO model and tested through a series of parallel experiments including the entire COSMO-model data assimilation cycle. Both COSMO-EU and COSMO-DE model configurations operational at DWD are used. The horizontal mesh size of these configurations is ca. 7 km and ca. 2.8 km, respectively. In the parallel experiments, the skewness-dependent "diffusion+advection" parameterizations of the third-order moments in the scalar (co-)variance equations are not used; instead, the third-order moments (fluxes of (co-)variances) are determined through the down-gradient formulations. Although the diffusion+advection parameterizations are available as an option, they are not recommended for immediate use with the full-fledged COSMO model. The use of the skewness-dependent third-order moments reduces numerical stability of the entire scheme. Then, a smaller time step is required, making the scheme computationally too expensive for current operational applications.

Results from the COSMO-EU and COSMO-DE parallel experiments with the TKESV scheme performed to date look promising. Verification of results against observational data indicate perceptible improvements as to some scores, e.g. two-metre temperature and humidity. Verification results show marginal improvements with respect to fractional cloud cover and no detectable changes with respect to precipitation. Performance of the TKESV scheme is exemplified by Figs. 4 and 5. The use of the TKESV scheme within COSMO-DE leads to a noticeable reduction of both bias and root-mean-square error (RMSE) of two-metre temperature and dew point depression. It should be emphasized that the curves in Figs. 4 and 5 are the result of averaging over the entire COSMO-DE domain. Local positive effects of the TKESV scheme on the COSMO-DE performance are often more pronounced.

As the results from the LES study of Mironov and Sullivan [16] demonstrate, the stably stratified PBL should be parameterized with due regard for the SGS heterogeneity of the

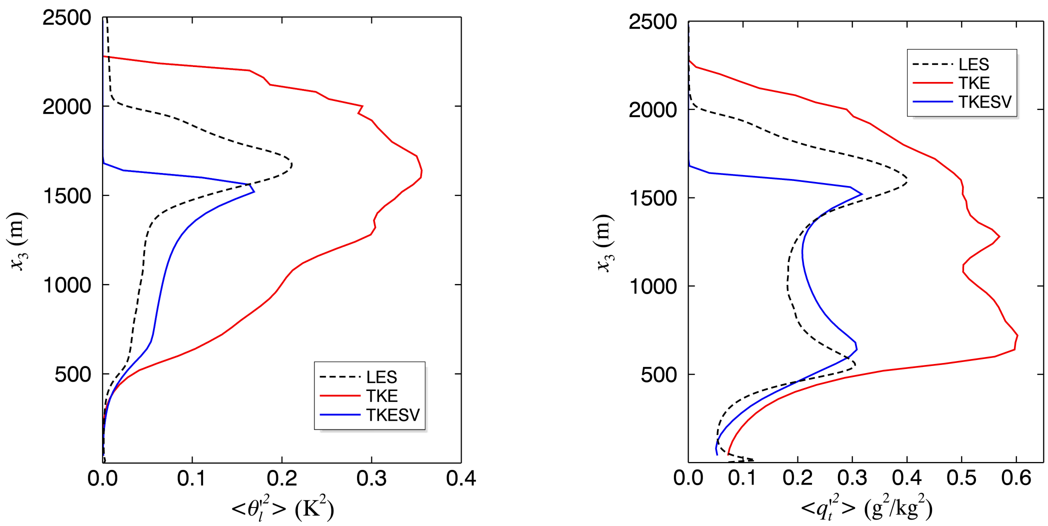

Figure 3: Variances of the liquid water potential temperature (left panel) and of the total water specific humidity (right panel) in the shallow-cumulus-topped PBL. Black dashed curves show data from LES of BOMEX shallow cumulus case performed by Heinze [7], and solid curves show results from numerical experiments with the TKE (red) and TKESV (blue) schemes. Both schemes use the cloud parameterization proposed in [2].

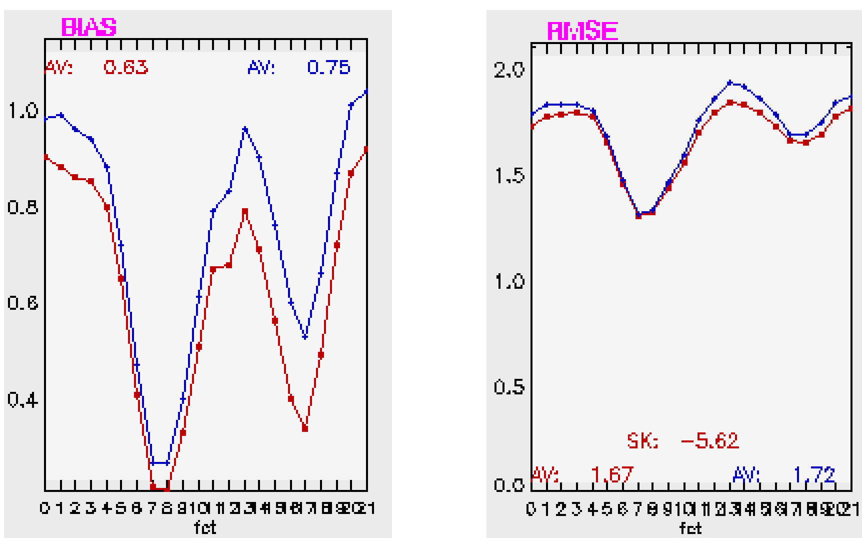

Figure 4: Bias (left panel) and RMSE (right panel) of two-metre temperature over the period from 1 July 2011 through 30 September 2011. Blue curves show operational COSMO-DE results, and red curves show results from parallel experiment with the new TKESV scheme. The curves are obtained by means of averaging over the COSMO-DE domain.

underlying surface, first of all, with respect to the temperature. An LES-based analysis of the second-moment budgets shows that the enhanced mixing in the heterogeneous stably stratified PBL is mainly due to a strong increase of the temperature variance near the underlying surface and the ensuing decrease of the magnitude of the (negative) buoyancy flux (cf. the importance of scalar variances in convective PBLs). As discussed in [16], there are

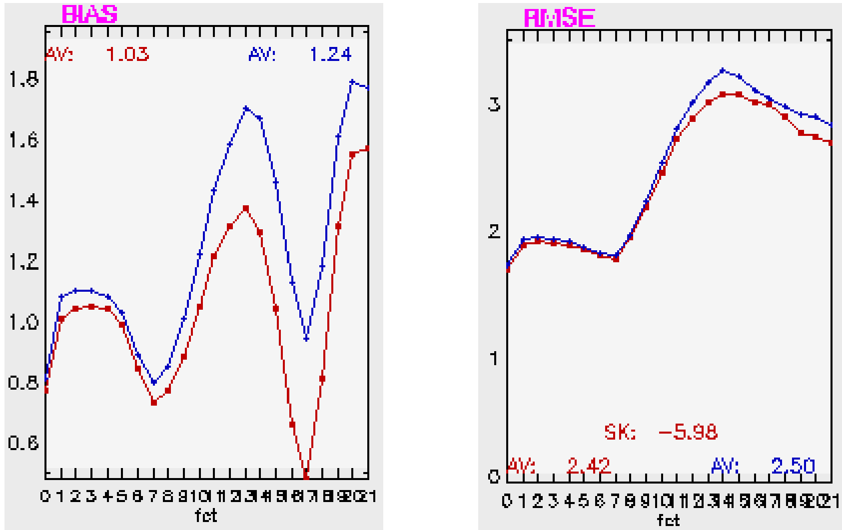

Figure 5: The same as in Fig. 4 but for the two-metre dew point depression.

several conceivable ways to account for this effect. One feasible way is the application of a tile approach. It allows to account for the enhanced mixing over heterogeneous surfaces in a physically plausible way and to prevent the PBL turbulence from dying out entirely as the (grid-box mean) static stability increases[1]. The idea is successfully tested through single-column numerical experiments (e.g. the increase of temperature variance and the enhancement of mixing over heterogeneous surfaces are reproduced). The number of tiles should not necessarily be large (otherwise the tiled scheme becomes computationally expensive) but the tiles with the largest difference in terms of thermal inertia should be accounted for. In this regard, the treatment of SGS water bodies is crucial. As the thermal inertia of water is (much) larger than the inertia of most other land types, the inclusion of SGS water allows to maintain the temperature difference between tiles and hence to account for the enhanced mixing due to surface heterogeneity. A parallel COSMO-EU experiment with a "two-tile" surface scheme is performed, where a "land tile" with the land-use type the same as in the operational COSMO model and an "inland water tile" ("lake") are considered in each COSMO-model grid box. The surface temperature of the inland water tile is computed with the lake parameterization scheme FLake [10, 14, 15]. Recall that in the operational COSMO configurations, only the grid boxes with the inland water fraction in excess of 0.5 are treated as the inland-water-type grid boxes whereas the SGS water bodies with fractional area coverage less than 0.5 are entirely ignored. Results from the parallel experiment indicate some improvements of the COSMO-model performance, e.g. warm bias of the near-surface temperature during summer is reduced.

[1] Cf. a long-standing COSMO-model problem with too large minimum diffusion coefficients that are used as a (unphysical) proxy for unaccounted mixing processes. These "background" diffusivities are insensitive to the mixing regime. They prevent the collapse of mixing but are often detrimental for stably stratified PBLs and for the inversions capping convective PBLs (produce too strong mixing where it is not needed). On the contrary, the TKESV scheme coupled to a tiled surface scheme is selective in terms of mixing regimes. For example, it produces enhanced mixing in the core of convective PBL but does not mix too strongly in the upper part of the stably stratified PBL and in the capping inversion.

5 Summary and outlook

A turbulence kinetic energy – scalar variance mixing scheme for COSMO is developed and favourably tested through single-column numerical experiments and through parallel experiments with the full-fledged COSMO model including the entire data assimilation cycle. The TKESV scheme outperforms the current COSMO-model TKE scheme. Verification of results from parallel experiments indicate improvements as to some scores, e.g. two-metre temperature and humidity and fractional cloud cover. A detailed scientific documentation of the TKESV scheme is in preparation. Modifications associated with the TKESV scheme will soon be included into the official COSMO-model code (for details, see the Priority Project UTCS Reports and the Model Development Plan at the COSMO web site).

In the future, the following issues should be addressed to further improve the COSMO-model mixing scheme.

(i) Development of a three-moment (mean, variance, and skewness) statistical cloud scheme capable of predicting the fractional cloud cover and the buoyancy flux in cloudy PBLs with due regard for non-Gaussian effects. This work is carried out by A. Seifert and A.-K. Naumann within the framework of the Hans Ertel Centre on Cloud and Convection, Hamburg. The major part of the work is completed (Naumann, A.-K., A. Seifert, and J. P. Mellado, 2013: A refined statistical cloud closure using double-Gaussian probability density functions. Submitted to *Geosci. Model Dev.*).

(ii) Further development and comprehensive testing of transport equations for the skewness of scalar quantities, coupling the skewness equations with the three-moment statistical cloud scheme. Closure assumptions for the scalar skewness equations and a skewness-dependent "diffusion+advection" parameterizations of the third-order moments in the scalar variance equations are developed and tested through single-column numerical experiments. They are available as an option within the TKESV scheme. These parameterizations are, however, not recommended for the immediate implementation into COSMO due to numerical stability problems (a smaller time step is required). The skewness-dependent parameterizations of the third-order transport may be used in the future, but further analysis, testing and tuning are required. However, the scalar skewness equations decoupled from the third-order transport but coupled to the statistical cloud scheme is a viable next-step option.

(iii) Improved coupling of the scalar (co-)variance equations to the tiled surface scheme to better account for the effect of surface heterogeneity on the structure and mixing properties of the PBL (mainly the stably stratified PBL). To this end, effort should go into the analysis of various flow regimes over heterogeneous surfaces (e.g. temperature-heterogeneous flat surface versus temperature-homogeneous surface with orographic features such as hills and valleys) and of the surface boundary conditions for the scalar (co-)variances with due regard for the surface heterogeneity. This work is to a large extent based on the LES findings reported in [16]. Further results are expected from co-operative work with P. Sullivan of NCAR.

The LES data set [8, 7], developed at the University of Hannover by R. Heinze and S. Raasch within the framework of the "Extramurale Forschung" program of the German Weather Service and the German Universities, will be extensively used to tackle the above issues.

Acknowledgments. The authors are grateful to Euripides Avgoustoglou, Peter Bechtold, Vittorio Canuto, George Craig, Ulrich Damrath, Sergey Danilov, Evgeni Fedorovich, Jochen Förstner, Jean-Francois Geleyn, Federico Grazzini, Vladimir Gryanik, Thomas Hanisch, Rieke Heinze, Richard Keane, Friedrich Kupka, Donald Lenschow, Chin-Hoh Moeng, Ned Patton, Robert Plant, Siegfried Raasch, Matthias Raschendorfer, Bodo Ritter, Harald Ruppert, Ulrich Schättler, Balázs Szintai, Axel Seifert, Pier Siebesma, Alan Shapiro, Peter Sullivan, Jeffrey Weil, and Jun-Ichi Yano for discussions and helpful suggestions. Thanks are due to Rieke Heinze for providing LES data shown in Fig. 3.

References

[1] Baldauf, M., A. Seifert, J. Förstner, D. Majewski, M. Raschendorfer, and T. Reinhardt, 2001: Operational convective-scale numerical weather prediction with the COSMO model: description and sensitivities. *Mon. Weather Rev.*, **139**, 3887–3905.

[2] Bechtold, P., J. W. M. Cuijpers, P. Mascart, and P. Trouilhet, 1995: Modeling of trade wind cumuli with a low-order turbulence model: Toward a unified description of Cu and Sc clouds in meteorological models. *J. Atmos. Sci.*, **52**, 455–463.

[3] Deardorff, J. W., 1970: Preliminary results from numerical integrations of the unstable planetary boundary layer. *J. Atmos. Sci.*, **27**, 1209–1211.

[4] Deardorff, J. W., 1970: Convective velocity and temperature scales for the unstable planetary boundary layer and for Rayleigh convection. *J. Atmos. Sci.*, **27**, 1211–1213.

[5] Gryanik, V. M., and J. Hartmann, 2002: A turbulence closure for the convective boundary layer based on a two-scale mass-flux approach. *J. Atmos. Sci.*, **59**, 2729–2744.

[6] Gryanik, V. M., J. Hartmann, S. Raasch, and M. Schröter, 2005: A refinement of the Millionshchikov quasi-normality hypothesis for convective boundary layer turbulence. *J. Atmos. Sci.*, **62**, 2632–2638.

[7] Heinze, R., 2013: *Large-Eddy Simulation von bewölkten Grenzschichten zur Untersuchung von Bilanzen der statistischen Momente zweiter Ordnung und zur Überprüfung von Turbulenzmodellen.* PhD thesis, Der Fakultät für Mathematik und Physik der Gottfried Wilhelm Leibniz Universität Hannover, 153 pp.

[8] Heinze, R., D. Mironov, and S. Raasch, 2012: Budgets of scalar fluxes for cloudy boundary layers. *20th Amer. Meteorol. Soc. Symp. on Boundary Layers and Turbulence*, Boston, MA, USA, paper 11.4, 9 pp.

[9] Holland, J. Z., and E. M. Rasmusson, 1973: Measurements of the atmospheric mass, energy, and momentum budgets over a 500-kilometer square of tropical ocean. *Mon. Weather Rev.*, **101**, 44–55.

[10] Mironov, D., V., 2008: Parameterization of lakes in numerical weather prediction. Description of a lake model. *COSMO Technical Report*, No. 11, 41 pp.

[11] Mironov, D. V., 2009: Turbulence in the lower troposphere: second-order closure and mass-flux modelling frameworks. *Interdisciplinary Aspects of Turbulence*, Lect. Notes Phys., **756**, W. Hillebrandt and F. Kupka, Eds., Springer-Verlag, Berlin, Heidelberg, 161–221.

[12] Mironov, D. V., V. M. Gryanik, V. N. Lykossov, and S. S. Zilitinkevich, 1999: Comments on "A New Second-Order Turbulence Closure Scheme for the Planetary Boundary Layer" by K. Abdella and N. McFarlane. *J. Atmos. Sci.*, **56**, 3478–3481.

[13] Mironov, D., V., V. M. Gryanik, C.-H. Moeng, D. J. Olbers, and T. H. Warncke, 2000: Vertical turbulence structure and second-moment budgets in convection with rotation: a large-eddy simulation study. *Quart. J. Roy. Meteorol. Soc.*, **126**, 477–515.

[14] Mironov, D., E. Heise, E. Kourzeneva, B. Ritter, N. Schneider, and A. Terzhevik, 2010: Implementation of the lake parameterisation scheme FLake into the numerical weather prediction model COSMO. *Boreal Env. Res.*, **15**, 218–230.

[15] Mironov, D., B. Ritter, J.-P. Schulz, M. Buchhold, M. Lange, and E. Machulskaya, 2012: Parameterization of sea and lake ice in numerical weather prediction models of the German Weather Service. *Tellus A*, **64**, 17330. doi: 10.3402/tellusa.v64i0.17330

[16] Mironov, D. V., and P. P. Sullivan, 2010: Effect of horizontal surface temperature heterogeneity on turbulent mixing in the stably stratified atmospheric boundary layer. *19th Amer. Meteorol. Soc. Symp. on Boundary Layers and Turbulence*, Keystone, CO, USA, paper 6.3, 10 pp.

[17] Raschendorfer, M., 1999: Special topic: The new turbulence parameterization of LM. *Quarterly Report of the Operational NWP-Models of the Deutscher Wetterdienst*, No. 19, 3–12.

[18] Raschendorfer, M., 2001: The new turbulence parameterization of LM. *COSMO Newsletter*, No. 1 , 89–97.

[19] Siebesma, A. P., Ch. S. Bretherton, A. Brown, A. Chlond, J. Cuxart, P. G. Duynkerke, H. Jiang, M. Khairoutdinov, D. Lewellen, Ch.-H. Moeng, E. Sanchez, B. Stevens, and D. E. Stevens, 2003: A large eddy simulation intercomparison study of shallow cumulus convection. *J. Atmos. Sci.*, **60**, 1201–1219.

[20] Sommeria, G., and J. W. Deardorff, 1977: Subgrid-scale condensation in models of non-precipitating clouds. *J. Atmos. Sci.*, **34**, 344–355.

[21] Stevens, B., C.-H. Moeng, A. S. Ackerman, Ch. S. Bretherton, A. Chlond, S. de Roode, J. Edwards, J.-Ch. Golaz, H. Jiang, M. Khairoutdinov, M. P. Kirkpatrick, D. C. Lewellen, A. Lock, F. Muller, D. E. Stevens, E. Whelan, and P. Zhud, 2005: Evaluation of large-eddy simulations via observations of nocturnal marine stratocumuls. *Mon. Weather Rev.*, **133**, 1443–1462.

On the Direct Comparison of COSMO Model Sub-Grid Stratiform Cloud Schemes with Satellite Images

Euripides Avgoustoglou

Hellenic National Meteorological Service, El. Venizelou 14, Hellinikon, Athens 16777, Greece

1 Introduction

In one of our previous works (Avgoustoglou E., 2012a), the possibility for direct comparison of the COSMO Model with remote sensing data was presented in reference to the wider geographical area around Greece. This possibility is based on the option of COSMO Model to create artificial satellite images and is enhanced by the fact that the Hellenic National Meteorological Service (HNMS) is using CineSat Software for the visualization of satellite data.

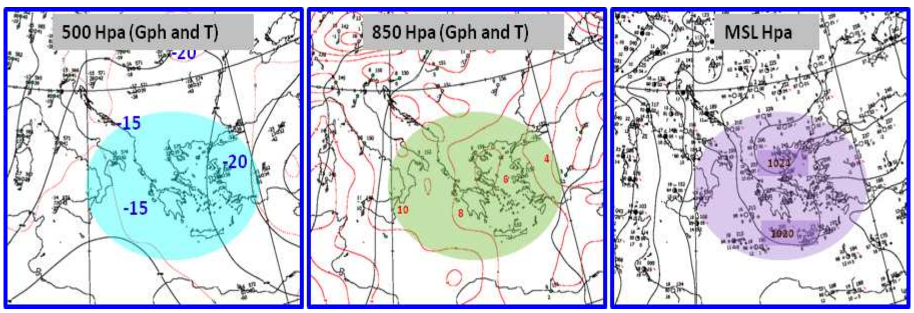

Figure 1: Analysis charts for 500 Hpa (left), 850 Hpa (medium), and Surface (right) at 00 UTC on the 5^{th} of November 2011 ©HNMS.

As a part of a systematic investigation under the UTCS project, a comparison of the implementation of two alternative sub-grid cloud schemes in the radiation scheme of COSMO model is presented over the wider geographical domain of the Balkans for a representative autumn case with extended areas of stratiform clouds developed over the Central-Eastern Mediterranean.

2 Highlights of the sub-grid stratiform cloud cover schemes in COSMO Model

The proper implementation of cloud cover in numerical weather prediction models stands as a challenging issue that goes beyond the straightforward assumption that all air inside the grid-box volume can be considered either saturated or unsaturated (Cotton, W. et al, 2011 and Mironov, D., 2009 and references there in). An obvious drawback of this hypothesis is that latent heat is released when condensation process occurs inside the grid box only after all its volume is saturated which might lead to an incorrect treatment to the initial cloud growth. Additionally, cloud cover might be affected by entrainment through grid box boundaries. In order to partially account for these processes in stratiform cloud-cover, a sub-grid statistical scheme, denoted as SGSL, is used in the moist turbulence module of COSMO model (Raschendorfer, M., 2005). This scheme is based on a bi-variate Gaussian distribution which is involving the quasi-conservative properties of saturation deficit and liquid water potential temperature (Sommeria, G. and Deardorff, J. W., 1977 and Mellor, G. L., 1977).

The resulting stratiform cloud cover from the implementation of SGSL in COSMO model is given by a two-parameter relation with respect to cloud cover at saturation and the critical value for over-saturation. The corresponding parameters and their default values used in this work are denoted as $clc\_diag = 0.5$ and $q\_crit = 4.0$ respectively.

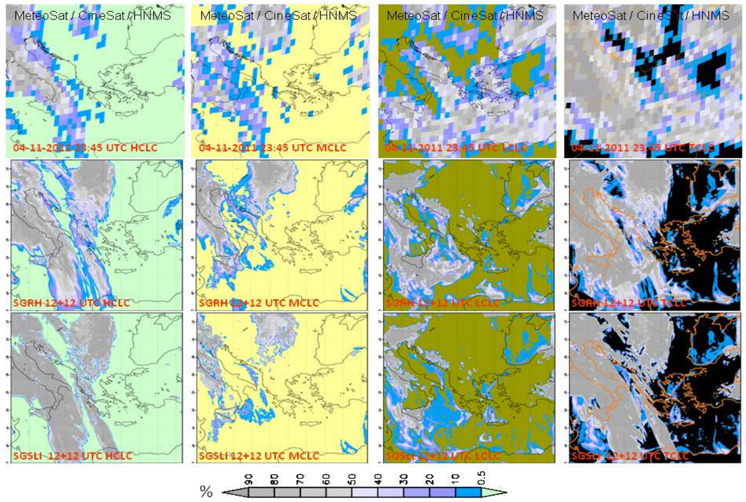

Figure 2: Cloud cover (%)on November 5 2011 at 00 UTC from the corresponding satellite (MPEF) figures (upper row ©HNMS/EUMETSAT), the SGRH Scheme (midle row) and the SGSLI scheme (lower row). The first, second, third and fourth columns refer to high, medium, low and total cloud cover respectivelly.

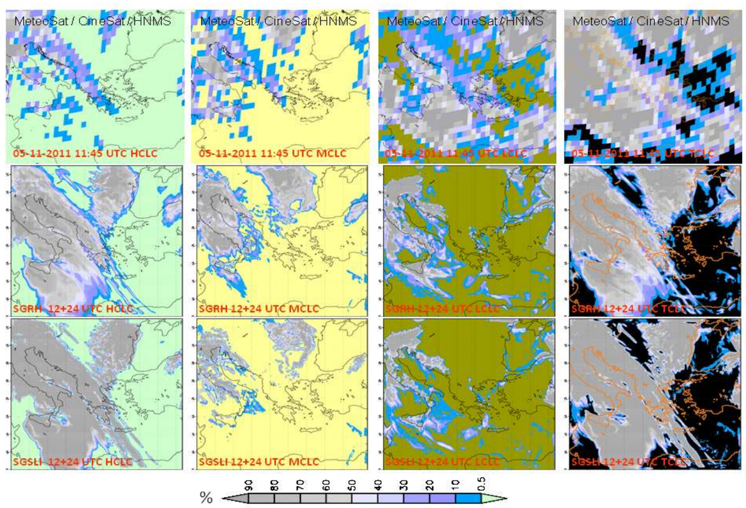

Figure 3: Cloud cover (%) on November 5 2011 at 12 UTC from the corresponding satellite (MPEF) figures (upper row ©HNMS/EUMETSAT), the SGRH Scheme (midle row) and the SGSLI scheme (lower row). The first, second, third and fourth columns refer to high, medium, low and total cloud cover respectivelly.

Within the context SGSL however, the cloud cover due to cloud ice content is treated by simply stating its value equal to 100% if *any* cloud ice is forecasted by the model. Additionally, the necessity for the effect of cloud-ice into the cloud cover (Deardorff, J. W., 1976 and Smith, S. A. and Del Genio, A. D., 2002) led to a modification of SGSL to a sub-grid statistical liquid-ice *mixed* scheme, denoted as SGSLI (Raschendorfer, M., 2008, 2011) through the introduction of a *mixed phase condensation* heat via an *icing factor* defined as the ratio of cloud ice over total cloud water content. In the radiation scheme of COSMO model, a semi-empirical sub-grid scheme, based on relative humidity and denoted as SGRH, is implemented by default to account for the stratiform cloud-cover (Seifert, A., 2011). The SGSL scheme is currently used operationally in the moist turbulence module of COSMO Model and the goal is to evaluate its use as a more general SGSLI scheme also in the radiation module within the scope of UTCS (Unified Turbulence Closure Scheme) priority project.

3 Case Study

A 36-hour period was considered, starting from 12 UTC of November 4 2011. The boundary conditions came from three-hour, forty-level analysis intervals based on GME and with horizontal grid of 0.5^0 ($\sim$ 50 Km). The horizontal grid size of COSMO model run is 0.0625^0 ($\sim$ 7 Km) and the integration time step was 30 secs. The domain under consideration is the wider Balkan Area with Greece at its center.

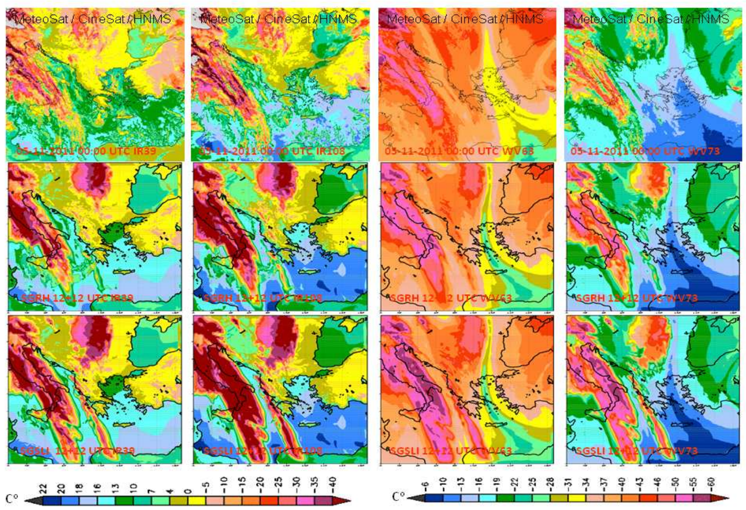

Figure 4: Cloud brightness temepratures (degs C) on November 5 2011 at 00 UTC from MSG satellite figures model (upper row) ©HNMS/EUMETSAT and the corresponding artficial satellite images from the SGRH scheme (midle row) and the SGSLI scheme (lower row). The first, second, third and fourth columns refer to 3.9 μm, 10.8 μm, 6.2 μm and 7.3 μm channels respectivelly.

From the synoptics standpoint (Fig. 1), the analysis charts show a relatively cold homogeneous filed in the center of the domain approximately between two barometric lows (eastern and western regions) and two highs (northern and southern regions) arranged alternately. This situation, resembling a barometric col, is characteristic of the area and favors low cloudiness practically over the Central-Eastern Mediterranean area. Some worm frontal activity over the western part of the domain should also be considered.

Regarding low cloud cover (third column of Fig. 2, and Fig. 3), it is overall underestimated by both SGRH and SGSLI schemes as shown in second and third rows of these figures respectively and with respect to the cloud analysis given in the first row. The cloud analysis figures have been produced by the Meteorological Products Extraction Facility Algorithms (MPEF) from METEOSAT (MSG) satellite data available locally at HNMS and were manipulated with CineSat software to match with the model figures. Both schemes miss most of low cloudiness over the eastern part of the domain while for the western part SGRH scheme performs relatively better.

The SGRH scheme performs also relatively better than the SGSLI scheme for high and medium cloudiness (first and second column of Fig. 2, and Fig. 3 respectively) that are practically confined over the western part of the domain and again in reference to the MPEF cloud analysis of the first row. An interesting feature regarding medium and high cloudiness is that the SGRH scheme provides a better tendency to resolve high cloud-cover, while the cloud structure of the SGSLI scheme has the tendency to remain more compact while for the medium cloud cover the situation is reversing. Both schemes agree with each other in reference to total cloud cover (fourth column of Fig. 2, and Fig. 3), however they both show a relatively poor performance over the eastern part of the domain which is essentially governed by low clouds. For the rest of the domain, the agreement with MPEF cloud analysis is excellent.

The above situation is highlighted in the comparison of cloud brightness temperatures between MSG and synthetic satellite images created by COSMO Model (Fig. 4 and Fig. 5) in the infrared channels of 3.9 μm, 10.8 μm (first and second column) and water-vapor channels of 6.2 μm, 7.3 μm (third and fourth column). The MSG images (first row these figures) show higher cloud brightness temperatures than the corresponding synthetic satellite images especially over the western region of the domain. However, the synthetic satellite images of the SGRH scheme (second row) provide an overall better signal than the ones of the SGSLI scheme.

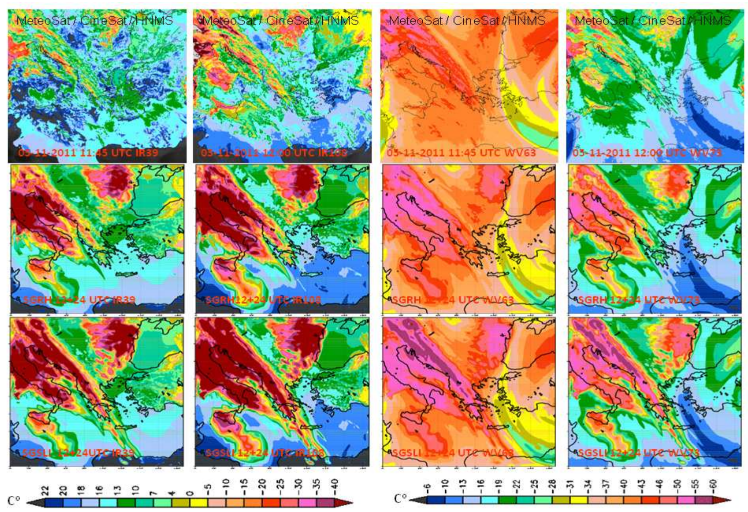

Figure 5: Cloud brightness temepratures (degs C) on November 5 2011 at 12 UTC from MSG satellite figures model (upper row) ©HNMS/EUMETSAT, and the corresponding artficial satellite images from the SGRH scheme (midle row) and the SGSLI scheme (lower row). The first, second, third and fourth columns refer to 3.9 μm, 10.8 μm, 6.2 μm and 7.3 μm channels respectivelly.

4 Summary and Outlook

The direct comparison of cloud cover and synthetic satellite images of COSMO model with the corresponding remote sensing products turns out to be a valuable feature towards the relative validation of the cloud schemes of the model. A more systematic evaluation of the different cloud schemes through the availability of these products (Avgoustoglou, E., 2011, 2012b) is currently under progress.

5 Acknowledgments

This work as well as my overall contribution to UTCS project were made possible through a modified version of COSMO Model provided by Matthias Raschendorfer who I gratefully thank. Dmitrii Mironov is gratefully acknowledged for his continuous support during my involvement in UTCS project as well as Norbet Liesering for his continuous help on the provision of boundary conditions.

References

[1] Avgoustoglou E., 2011: Investigation Of Different Parameterizations Of The Mixed Liquid-ice Sub-grid Statistical Cloud Scheme Over Greece. *Presentation* 13th COSMO General Meeting, 5-9 Rome, Italy.

[2] Avgoustoglou, E., 2012b: Assessment of the Sub-Grid Stratiform Cloud Schemes of COSMO Model with Satellite Data. *Presentation* 14th COSMO General Meeting, Lugano, Switzerland.

[3] Cotton, W., Bryan, G. and van der Heever, S., 2011: Storm and Cloud Dynamics. *Elsevier Academic Press, London United Kingdom and San Diego, CA, USA*.

[4] Deardorff, J. W., 1976: Usefulness of Liquid-Water Potential Temperature in a Shallow-Cloud Model. *Journal of Applied Meteorology*, **15**, 98-102.

[5] Mellor, G. L., 1977: The Gaussian Cloud Model Relations. *Journal of the Atmospheric Sciences*, **34**, 356-358.

[6] Mironov, D., 2009: Turbulence in the Lower troposphere: Second-order Closure and Mass-Flux Modelling Frameworks. *Lecture Notes in Physics*, **756**, 161-221.

[7] Sommeria, G. and Deardorff J. W., 1977: Subgrid-Scale Condensation in Models of Non-precipitating Clouds. *Journal of the Atmospheric Sciences*, **34**, 344-355.

[8] Raschendorfer, M., 2005: A new TKE-based Scheme for Vertical Diffusion and Surface-layer Transfer. *DWD Internal Report*.

[9] Raschendorfer, M., 2008: Mixed water/ice phase in the SGS condensation scheme and the moist turbulence scheme. *Presentation*, 10^{th} COSMO General Meeting, Cracow, Poland.

[10] Raschendorfer, M., 2011: Sub grid scale transport by turbulent diffusion: a consequence from the numerical treatment of principal model equations. *Presentation*, COSMO/CLM Training Course, Langen.

[11] Seifert, A., 2011: Physical Parameterizations: Cloud Microphysics and Subgrid-Scale Cloudiness. *Presentation*, COSMO/CLM Training Course, Langen.

[12] Smith, S. A. and Del Genio, A. D., 2002: A simple conceptual conceptual model of cirrus horizontal inhomogeneity and cloud fraction. *Quarterly Journal of the Royal Meteorological Society*, **128**, 149-171.

Realization of the parametric snow cover model SMFE for snow characteristics calculation according to standard net meteorological observations

E. Kazakova, M. Chumakov and I. Rozinkina

1 Introduction

Nowadays careful description of thermo-hydro interaction between land surface and atmosphere becomes topical in numerical weather prediction problems. It is connected with higher reality of atmospheric models, higher requirements to the accuracy and space-time resolution of described weather processes. It should be noted that land-surface characteristics are model variables, so further success of their forecasting depends on their initial values accuracy. The technology of making initial fields of these characteristics is based on operational meteorological observations processing. In case when this or that model variable is not the measured value, some functional dependencies are used.

In atmospheric models snow cover is described in terms of snow water equivalent (SWE) as a part of hydrological cycle. Its evolution can be described as a result of generated precipitation in model, percolation and melt water runoff. A special importance has the exact determination of snow water resources during melting of snow for more accurate estimation and forecasting of boundaries of its bedding, which define the whole structure of heat balance for snow-covered and snow-free areas. The difficulty is that SWE is not a part of standard meteorological observations, its measurements are held on some specialized stations in the form of time series with discreteness of several days. Such a situation doesnt satisfy demands of systems of initial fields construction for weather forecast models. Besides snow cover is a complex heterogeneous porous medium, consisting of all the phase components with constantly changing properties, which depend on external (atmospheric) and internal (for example, compaction due to gravity) factors. During the research of forecasts of snow cover characteristics, calculated by COSMO-RU, it was ascertained that using of simple dependences based on monotonous "aging functions" for initial GME-fields generation([3], [4]) can led to distortion in snow water equivalent values in two times and more ([6], [7]).

Integration of parameterizations implemented in atmospheric models, including multi-layer snow models (for example, [16]) needs to specify a whole number of regularly not measured external parameters, in the first place - heat and radiation fluxes. These variables can be taken only from atmospheric model, what inevitably leads to accumulation of discrepancies and departure from reality during long snow periods modeling.

This research is dedicated to the realization and discussion of the results got from rather economical approach of the snow "lively cycle" parameterization (model SMFE - Snow Model based on Finite-Element approach). The input parameters for SMFE are only regular standard meteorological station observations. The model can be used in future as an element of the initial fields construction system for atmospheric models (as an example - mesoscale model COSMO-RU) and also as an instrument for snow characteristics calculation at stations, where meteorological observations are held - for such applied tasks as, for example, holding the competitions on winter sports, hydrological forecasts, agricultural works planning.

2 Goals and Objectives

The goal of the present research was to realize the algorithm of snow cover characteristics calculation using only standard surface meteorological observations (snow depth, 2 meters temperature, dew point, 10 meters wind speed in SYNOP-code). It is very important for weather forecast tasks that realistic initial fields should be input in the model during the fixed periods of calculation start. So the algorithm should contain the main mechanisms in snow cover changing and be realized during short periods of time. The algorithm should be rather universal, i.e. it should provide realistic results for different climatic zones, including mountainous regions.

In the framework of PP CORSO for tasks realization connected with meteorological support of approaching winter Olympic Games in Sochi information about snow characteristics and their forecast for stations is needed. This problem can be solved, as nowadays automatic meteorological stations sending information about meteorological parameters with the high discreteness in time are set on sport facilities. An additional part of the research was to estimate the applicability of "classical" dependencies known from literature (for example, integral formulas for evaporation calculation).

3 Materials and Methods

The basis of the realized one-dimensional parametric model SMFE was the principle permitting to represent the snow column as a number of finite elements, which are in thermal and mechanical interaction with each other (fig. 1). Number of elements depends on the height of column. The column height is a snow height, measured at the meteorological stations. Each finite element has the form of cuboid with the height of 1 cm, length and width of 100 cm. I.e. if, for example, the measured snow height is 50 cm, this means that the column consists of 50 finite elements.

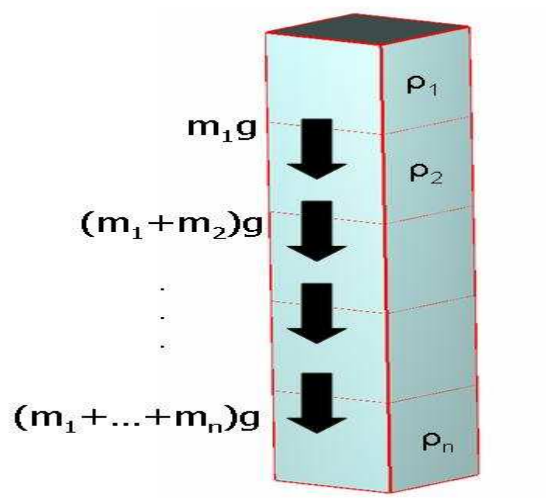

Figure 1: Representation of snow column in the snow model.

In the model the process of snow metamorphism due to gravity is taken into account according to dependence, suggested [17]. Thus, according to Yosida and Huzioka data Young modulus of snow E (Pa) as a function of snow density at temperatures from -1 to $-3°C$ and from -5 to $-13°C$ can be distinguished from formula (1) (we used the simplified condition for temperature: greater then $-5°C$ or less):

$$E_1 = (0.0167\rho - 1.86) \cdot 10^6 \; and \; E_1 = (0.059\rho - 10.8) \cdot 10^6 \tag{1}$$

It is supposed that finite elements experience only elastic deformation. The easiest elementary deformation is a relative elongation of some element:

$$e = \frac{l_n - l_0}{l_0}$$

where e - deformation, l_n - the length of an element after deformation, l_0 - the initial length of the element.

According to [1], in the capacity of fluidity limit the value of stress at permanent deformation $0.2\%(\sigma_{0.2})$ is chosen.

Thus for our case we have:

$$\frac{l_n}{l_0} = (1 - \sigma_{0.2}) = 1 - 0.002$$

Consider that following finite element experiences the pressure of the overlying layers the finish formula for snow density calculations take on form:

$$\rho = \frac{\frac{mg}{10^6(1-\sigma_{0.2})} + 1.86}{0.0167}, T > -5°C; \; \rho = \frac{\frac{mg}{10^6(1-\sigma_{0.2})} + 10.8}{0.059}, T < -5°C$$

where $m = (\rho_1 + \rho_2 + \ldots)H, H = 0.001\mathcal{M}$.

In many models for weather or climate forecasts in fresh-fallen snow description is used the assumption that fresh snow density is approximately equal to $100kg/m^3$. Yet according to numerous researches (for example [5], [15]) fresh snow density can differ from this value. The dependence on air temperature for fresh snow density calculations was proposed in paper [2] (formula (2)), which were used in the developed one-dimensional model:

$$\rho_{s,f} = 67.92 + 51.25e^{\frac{T_a}{2.59}}, T_a < 0°C; \; \rho_{s,f} = min(200, 119.2 + 20T_a), T_a > 0°C \tag{2}$$

where $\rho_{s,f}$ - fresh snow density, T_a - 2 meters temperature.

Depending on average daily temperature in model it is defined what kind of snow is fallen on the generated snow cover. If the temperature is positive, it is assumed that wet snow lies above the snow column (formed since the previous day), which will give snow density increase to the column "top" due to contained water. If the temperature is negative then dry snow is falling on the column, and further redistribution of density in snow column will depend on of what density and how much snow fell and whether can the snow cover existing from the previous day sustain the pressure of newly-fallen snow according to elastic deformation approach or considerably transform under its weight.

Daily temperature fluctuations according to formula (2) define whether density in the column is changing uniformly or there are sections with higher or lower density ("intrusions").

In case of snow depth decrease vertical distribution of liquid mass in elements of all "intrusions" is provided.

During snow melting processes and its water loss the runoff is included, which value depends on relief.

The case of so called blowing snow is taken into account, which is defined by the condition $100\% - (\frac{H_{new} \cdot 100\%}{H_{new}}) > 40\%$, where H_{new} - current snow height, H_{old} - snow height at previous day.

It is suggested that the maximum snow density in model cant be more then $700kg/m^3$ (conditionally equal to porous ice density).

For evaporation calculation from snow surface the widely known formula by P.P. Kuzmin ([8]) was used:

$$F = (0.18 + 0.098u_{10m})(e_{pot} - e_{2m})\ \mathcal{MM}/day \qquad (3)$$

where F - evaporation rate, u_{10m} - wind speed at 10-m height, e_{pot} - saturated vapor pressure over snow, e_{2m} - air vapor pressure at 2-m height.

For saturated vapor pressure calculations on 2 meters and on snow surface (snow roughness length) the use of formula ([10]) is needed, with a glance of tables ([9]):

$$e^* = 10^{[c + b/T]} T^a$$

a, b, c - constants, depending on whether evaporation is held over water or ice, T - 2-meters temperature or snow surface temperature.

Vapor pressure at 2-m height is:

$$f = \frac{e(T)}{e^*(T)},\ e(T) = e_{2\mathcal{M}}(T) = e^*(T) \cdot f$$

where f - relative humidity, calculating with the use of dew point values:

$$f = 10^{[(c - c_1) + b/D - b_1/T]} D^a T^{-a_1}$$

D - dew point temperature, a_1, b_1, c_1 - constants.

If the value of dew point is higher then a freezing point, then relative humidity is calculated according to formula:

$$f = (\frac{D}{T})^a 10^{b[1/D - 1/T]}$$

In case of absence measurements of snow temperature (or - as an additional option of model) the following relation for its definition is used ([8], [12]):

$$T_{snow} = T_{2\mathcal{M}} - \frac{1}{\mathcal{K}}\sqrt{\frac{\tau_0}{\rho}} ln\frac{z}{z_0}$$

where $\mathcal{K} = 0.4$ - constant von Karman, τ_0 - shear stress, $\rho = 1.293kg/\mathcal{M}^3$ - air density, $z = 2\mathcal{M}$ - the height for standard observations at meteorological station, $z_0 = 0.001\mathcal{M}$ - aerodynamic roughness for snow ([11]).

The formula for wind shear stress τ_0 mostly used in practice of engineering calculations ([18]) looks as:

$$\tau_0 = \rho c|u_{10\mathcal{M}}|u_{10\mathcal{M}}$$

where $c = 0.003$ - a typical value of friction coefficient [18], which is got through substitution of the height of surface friction $z = 2\mathcal{M}$ and aerodynamic roughness $z_0 = 0.001\mathcal{M}$ in formula for friction coefficient calculation:

$$c = \left(\frac{k}{ln(\frac{z}{2z_0})}\right)^2$$

The output parameters of the model for each station are snow density and snow water equivalent (average values), density distribution in the snow column (values for each finite element), snow surface temperature.

Model testing was held for some stations of the European part of Russia (fig. 2). Three seasons with snow cover were analyzed: 2009-2010, 2010-2011 and 2011-2012. Hydrological station observations of snow water equivalent and snow height with the frequency of once in 10 days, during snow melting - once in 5 days were used for comparison with the received model results of snow density and snow water equivalent. Initial fields of snow water equivalent for period February-March 2012, received from DWD modeling-assimilation global system (with the help of the global model GME), were also used for comparison. In this continuous data assimilation system the model snow parameterization coupled with aging functions is used - rather typical approach for problems like this. Particularly exactly such an information is used nowadays as initial data for weather conditions modeling in mesoscale model COSMO-RU ([13], [14]). A comparison between values of snow surface temperature received due to one-dimensional model and station SYNOP observations and initial field for the model COSMO-RU was held.

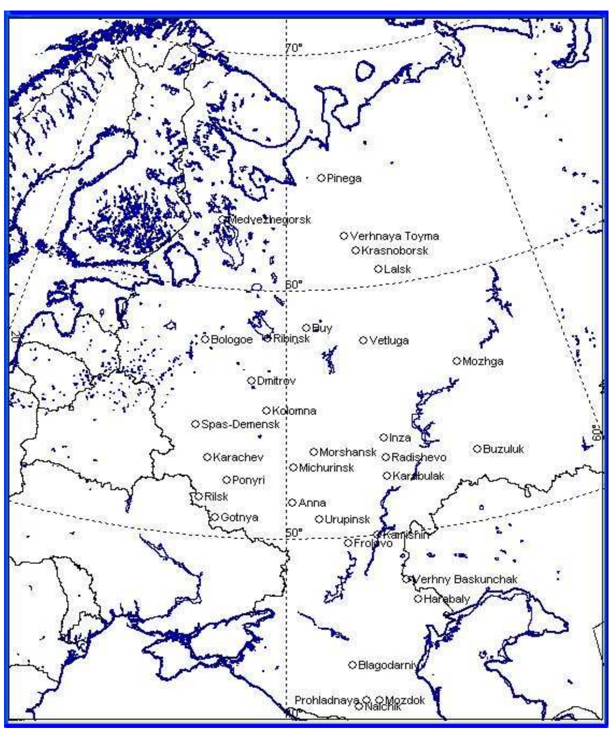

Figure 2: The researched region - European part of Russia.

Also the developed snow model was tested on the region of Sochi Olympic Games. The automatic meteorological stations data include measurements (temperature, relative humidity, wind speed, snow height, snow temperature) with the time interval of 30 minutes. The data of winter season 2011-2012 was available (fig. 7).

4 Results and Discussion

By comparing model results and hydrological observations it was revealed that the developed one-dimensional multi-layer snow model simulates well the snow evolution during the whole period of its existence (fig. 3, 4, 5). RMSE for water equivalent values for stations situated in different zones in the European Part of Russia is 1,5-8 mm by relative error of $15 - 20\%$. For example, for station Dmitrov RMSE is 1,3 mm by average absolute error of 7,6 mm and average SWE equal to 48 mm.

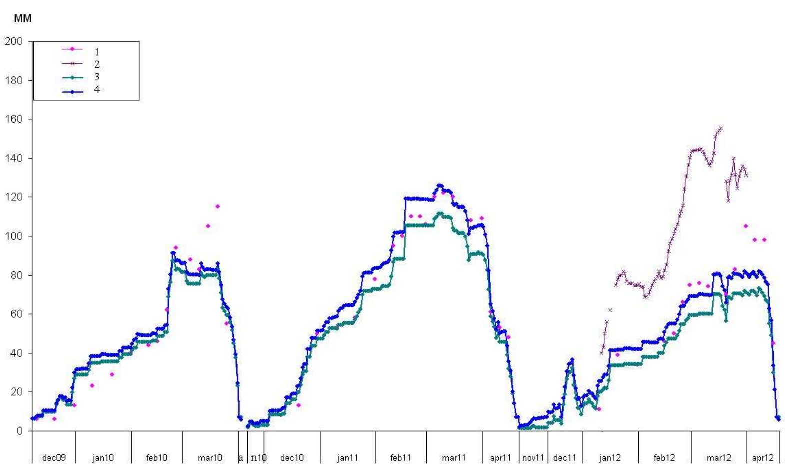

Figure 3: Snow water equivalent distribution during winter seasons 2009-2010, 2010-2011 and 2011-2012 for station Dmitrov: (1) hydrological station data; (2) initial field from the model GME, prepared for the model COSMO-RU; (3) model SMFE results; (4) model SMFE results with using formula (3).

As an example of successfulness of SWE modeling two stations can be examined: the first one - situated in the north of the European part of Russia, with predominance of low temperatures during snow falling (Medvezhegorsk), the second one - situated in unstable snow cover conditions, with predominance of temperatures near 0^oC during snow period (Nalchik). The analysis of model data makes it possible to conclude that in both cases the model simulates snow cover characteristics realistically.

It is much more smaller then discrepancies of the analogue values, calculated by GME (in the last case differences can reach $200 - 300\%$, and can change from 10 mm for southern regions to 130 mm - for northern) ([6]).

For station Medvezhegorsk the results of the model have more deviation in comparison with observations than for central and southern stations. It should be noted that this station is situated in forested area, and during cold season snow on trees can experience changes. These tiny changes can't be described in the model using only SYNOP data.

Thus the developed one-dimensional model accurately reproduces SWE evolution in time. This is achieved through using numerical finite-element scheme which allows taking into account the main principles of physical theory of elasticity.

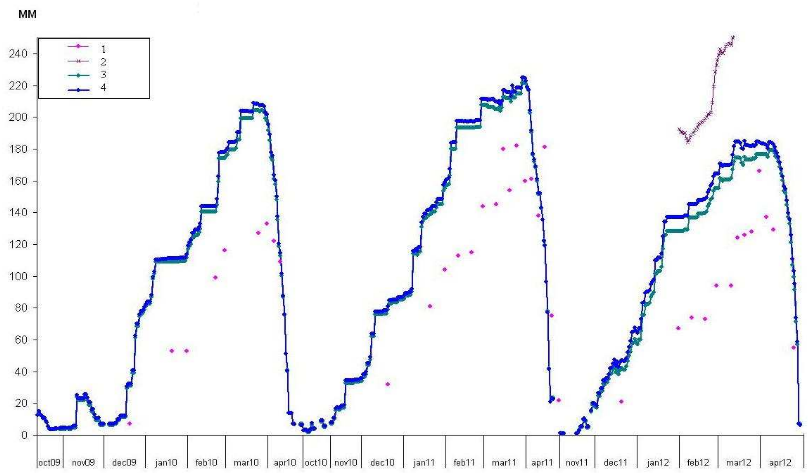

Figure 4: Snow water equivalent distribution during winter seasons 2009-2010, 2010-2011 and 2011-2012 for station Medvezhegorsk: (1) hydrological station data; (2) initial field from the model GME, prepared for the model COSMO-RU; (3) model SMFE results; (4) model SMFE results with using formula (3).

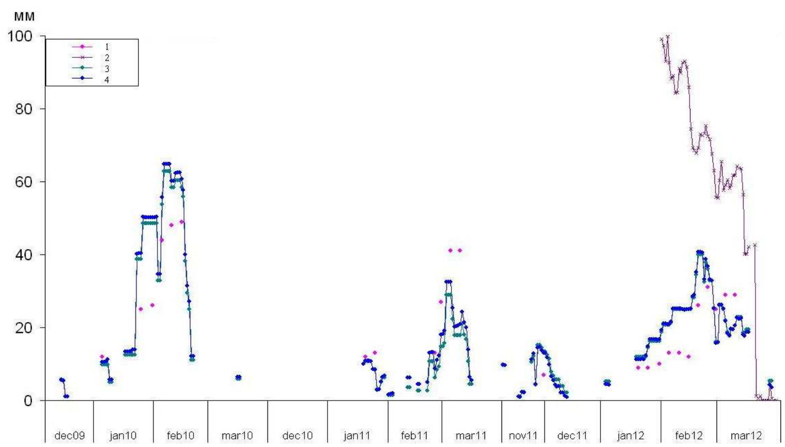

Figure 5: Snow water equivalent distribution during winter seasons 2009-2010, 2010-2011 and 2011-2012 for station Nalchik: (1) hydrological station data; (2) initial field from the model GME, prepared for the model COSMO-RU; (3) model SMFE results; (4) model SMFE results with using formula (3).

Snow surface temperature can be calculated in the model as an additional option. It is comparable with meteorological stations data (fig. 6). RMSE for the parametric model is less than 6^oC for 00 UTC for period 1 February - 31 March 2012, for snow surface temperature initial fields from GME-system - less than 5^oC. The same values are got for the developed model for periods of snow cover existence in different years 2009-2010, 2010-2011 and 2011-2012 for 00 UTC and 12 UTC. Some extreme low values can be observed (fig. 6), and it can be explained by using formulas for temperature calculations only for stable conditions (which are not always observed in nature).

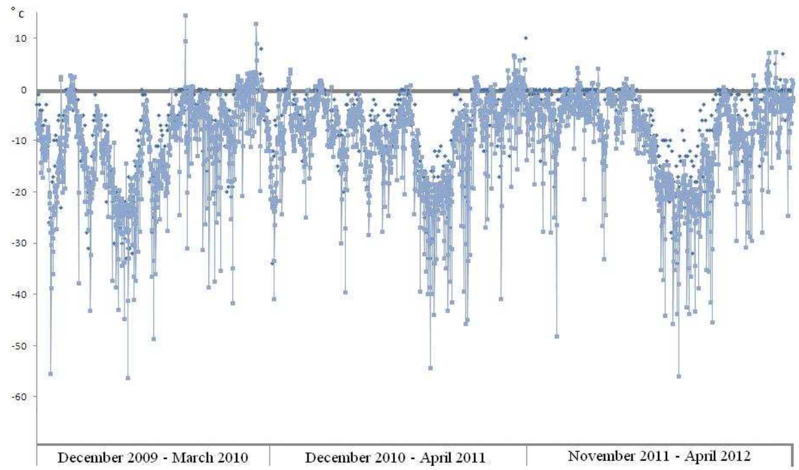

Figure 6: Snow temperature during winter seasons 2009-2010, 2010-2011 and 2011-2012 for station Poniri: blue dots - station data, gray dots - model results.

In order to calculate snow cover characteristics for the region of Sochi Olympic Games we use data with 30-minutes time interval from automatic meteorological stations. For winter period 2011-2012 we use stations, situated on the sports facility (fig. 7). As can be seen from the figure, snow height in mountain region can reach the value of some meters to the end of winter season.

The snow model makes it possible to calculate snow characteristics for the layer of snow. For providing meteorological forecasts during winter Olympic Games it is important to have knowledge about snow cover in the upper layer. As an example, the distribution of snow water equivalent was calculated for the upper 10 cm of snow cover for station 11 (fig. 8), as well as snow density (fig. 9). The model design allows receiving information about snow cover for any layer the user is interested in (so, it can be 50 cm or 20 cm or whatever).

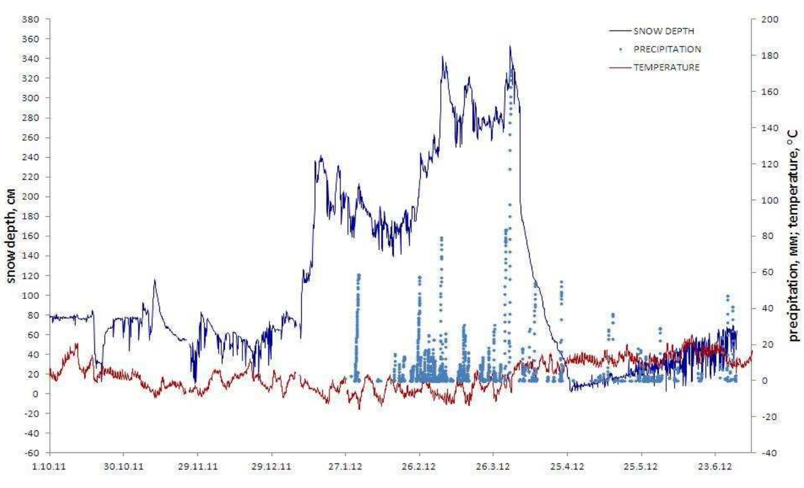

Figure 7: Distribution of snow depth, 2m temperature and precipitation for period 1 October 2011 - 1 August 2012 for automatic meteorological station 11 in the region of Sochi Olympic Games. The station height is 1580 m.

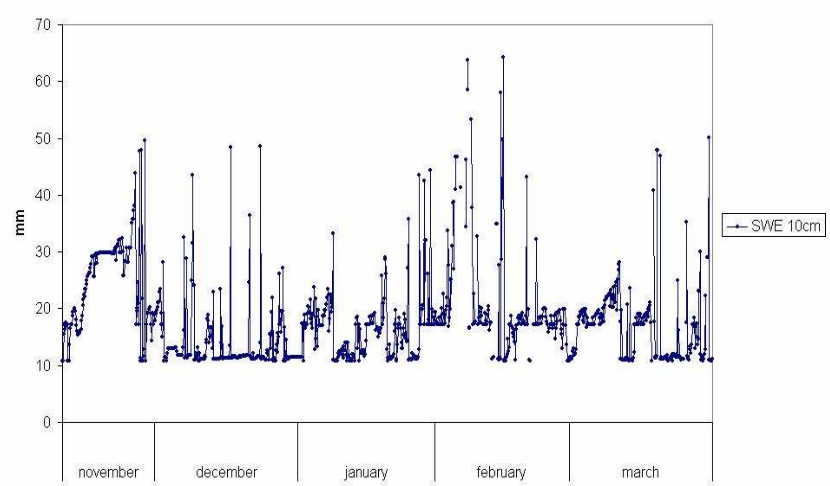

Figure 8: Distribution of snow water equivalent for the upper 10 cm for station 11 in the region of Sochi Olympic Games. 1 November 2011 31 March 2012.

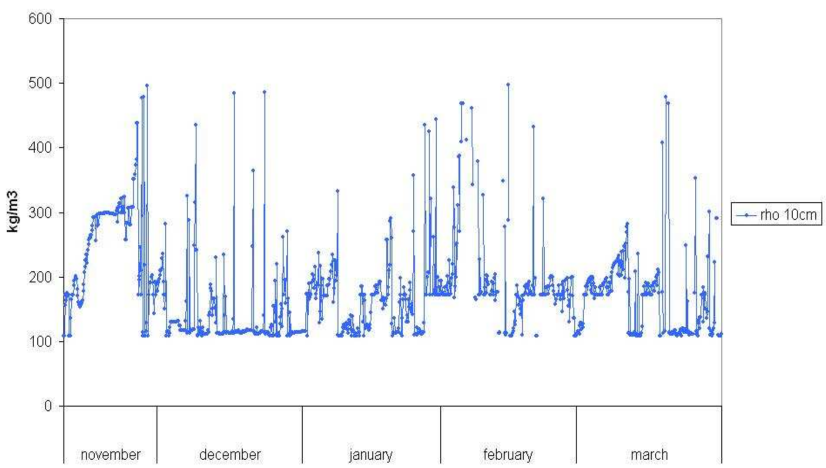

Figure 9: Distribution of snow density for the upper 10 cm for station 11 in the region of Sochi Olympic Games. 1 November 2011 - 31 March 2012.

5 Conclusion

The developed one-parametric numerical multi-layer model SMFE working with standard meteorological station data in SYNOP-code is realized. The structure of the model allows calculating of snow cover characteristics (SWE and snow density (average values for a snow column), snow density for each element, snow surface temperature) for each station with a discreteness, which is defined by snow depth measurements frequency (once a day - in case of stations situated at the European part of Russia, once in 3 hours - for automatic stations in the region of Sochi Olympic Games). Testing of SMFE based on physical elasticity principles by Russian meteorological stations situated in different climatic conditions is revealed that with its help realistic values of SWE and snow density can be obtained. The developed model was also tested for the region of Sochi Olympic Games according to automatic stations observations with high time discreteness. It is shown that snow characteristics can be calculated for any snow layer needed for a user. For that moment there is no such an observed data (SWE, snow density for snow period) in this region to compare with the model results. It is planned to develop the technology of operational making of analysis fields for snow cover in territories based on interpolation methods and combining the model results with satellite data and to enter the technology in the data assimilation block for mesoscale model COSMO-RU.

References

[1] All-Union State Standard 12004-81, 1986: Reinforcing Steel. Methods of Elongation Test. - Instead of All-Union State Standard 12004-66. - Moscow, The State USSR Committee on standards; Moscow: Publishing House of Standards.

[2] Bartlett, P.A, M.D. MacKay and D.L. Verseghy, 2006: Modified Snow Algorithms in the Canadian Land Surface Scheme: Model Runs and Sensitivity Analysis at Three Boreal Forest Stands, *Canadian Meteorological and Oceanographic Society, ATMOSPHERE-OCEAN* 43 (3), **207-222**.

[3] Dickinson, R.E., A. Henderson-Sellers, P.J. Kennedy and M.F. Wilson, 1986: Biosphere Atmosphere Transfer Scheme (BATS) for the NCAR Community Climate Model, NCAR Tech. Note, NCAR, TN275+STR.

[4] Doms, G., E. Heise et al., 2007: A Description of the Nonhydrostatic Regional Model LM, part 2: Physical Parameterization.

[5] Judson, A. and N. Doescen, July 2000: Density of Freshly Fallen Snow in the Central Rocky Mountains, *Bulleten of the American Meteorological Society*, vol.81, no.7, **1577-1587**.

[6] Kazakova, E. and I. Rozinkina, 2011: Testing of Snow Parameterization Schemes in COSMO-Ru: Analysis and Results, *COSMO Newsletter*, No.11, **41-51**.

[7] Kazakova, E., I. Rozinkina and E. Machulskaya, 2010: Testing Results of the New Snow Parameterization Scheme during Snow Melt Conditions in the Model COSMO-RU, *Proceedings of the State Institution Hydrometeorological research centre of Russian Federation*, Vol.344, Atmospheric Physics and Weather Forecast, Moscow, **147-164**.

[8] Kuzmin, P, 1961: Process of Snow Cover Melting, Leningrad, Hydrometeoizdat.

[9] List, R.J., 1971: Smithsonian Meteorological Tables. Sixth ed. Smithsonian Institution Press.

[10] Owen Pasish, O. and T.W.Putnam, 1977: NASA Technical Note D-8401. Equations for the Determination of Humidity from Dewpoint and Psychrometric Data, National Aeronautics and Space Administration, Washington, D.C.

[11] Pielke, R., 2001: Mesoscale Meteorological Modeling, 2nd Edition, *International Geophysics Series*, Vol.78.

[12] Prandtl, L., 1928: Uber die ausgebildete turbulenz. - ZAMM, No. 5.

[13] Rivin ,G., I. Rozinkina and D. Blinov, 2012: Technological Line of the Short-Range Mesoscale Operative Weather Forecasts System COSMO-RU with 7 km Grid Step, *Proceedings of the Hydrometeorological research centre of Russian Federation*, Vol.347, Hydrometeorological Forecasts, Moscow, **61-80**.

[14] Schttler, U., G. Doms and C. Schraff, 2012: A Description of the Nonhydrostatic Regional Model LM, part 7: Users Guide.

[15] Strack, J.E., G.E. Liston and R. Pielke, Oct. 2004: Modeling Snow Depth for Improved Simulation of Snow-Vegetation-Atmosphere Interactions, *Journal of Hydrometeorology - Special section*, Vol.5.

[16] Volodina, E., L. Bengtsson and V. Lykosov, 2000: Parameterization of Heat and Water Transfer in Snow Cover for Seasonal Variations of Land Hydrological Cycle Modeling, *Meteorology and Hydrology*, No.5, **5-14**.

[17] Yosida, Z. and T. Huzioka, 1954: Some Studies of the Mechanical Properties of Snow. *IAHS Red Book Series*, Publ. no. 39, Gentbrugge, **98-105**.

[18] User Manual. www.flow3d.com

New Approach to Parameterization of Physical Processes in Soil in COSMO Model - Preliminary Results

Grzegorz Duniec and Andrzej Mazur[1]

1: Department for Numerical Weather Forecasts. Insitute of Meteorology and Water Management National Research Institute. PL-01-673 Warsaw, Podleśna st. 61; grzegorz.duniec@imgw.pl; andrzej.mazur@imgw.pl

Summary

In this paper a first try of a new approach to parameterization of physical processes in soil in COSMO model is presented. Authors tried to established whether the increasing of a number of levels in TERRA_LM model would result positively in quality of forecasts.

1 Introduction

Basic facts: we must be honest - multi-level soil model TERRA_ML is (still!) a weak point in COSMO model. Thus, there is a need for improvement - via proper initialization, more reliable data, new parameterization etc.

In a current (reference) version of COSMO soil model is based on 7-level structure. Substantial change (some time ago) from two levels (TERRA) to seven levels (TERRA_ML) made a substantial difference in results.

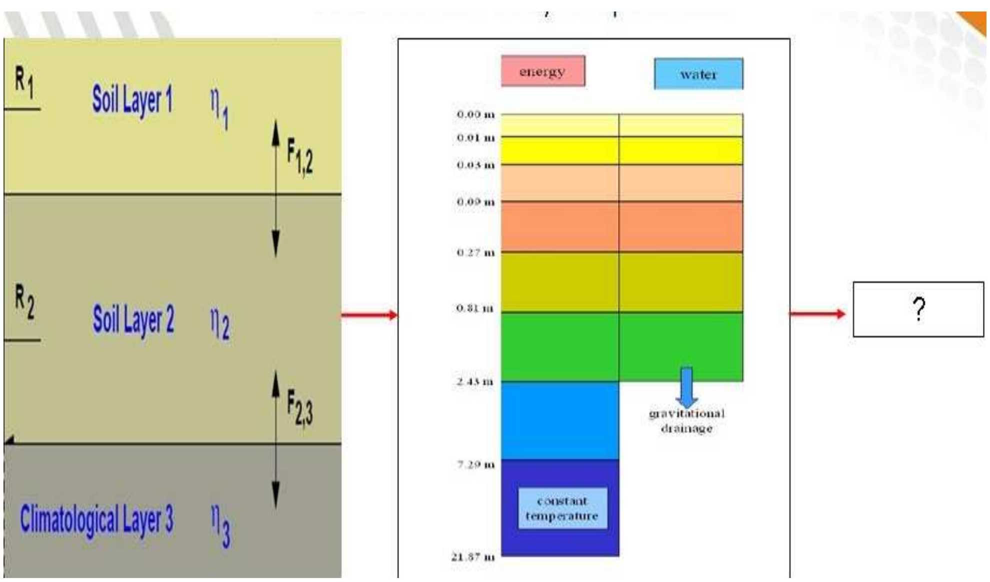

Figure 1: Changes of structure of soil model TERRA in COSMO meteorological model.

Maybe now it is the time to go further, dividing this structure of seven levels into more detailed one? or maybe we should try another type of approach? In this paper authors would like to present preliminary results of this new approach and to draw some outlines of further work.

2 Basic methodology

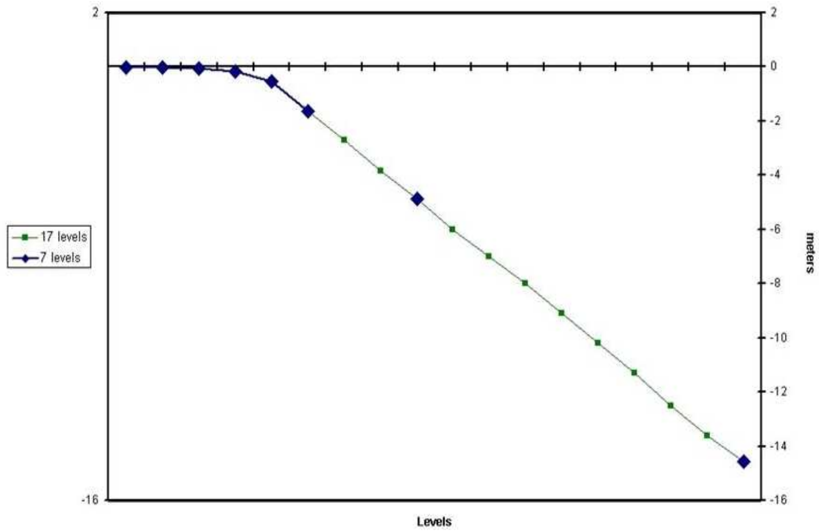

Figure 2: A proposition of a new soil model structure - ten new levels. Solid black horizontal line marks ground level; big blue squares and blue line mark TERRA_ML 7 basic levels; small green squares and green line mark new introduced "detailed" levels.

A fundamental question to answer in this study was whether introduction of more (detailed) soil levels may be a way to improvement of a soil model. Authors agreed to introduce new levels in such a way that a new single-layer depth was uniform and equal to, approximately, 0.5 m. The basic structure of new "detailed" levels is shown in the Figure 2.

3 Preliminary results (case studies)

To assess results fields of air temperature (T2M) and dew point temperature (TD2M) at 2m above ground level, wind speed (U10M) at 10m a.g.l., cloud cover (CLC)and pressure reduced to mean sea level (PMSL) were selected.

At least two model runs every month of first half of 2012 were carried out. First thing that authors were able to find was that during Winter and Spring (January, February, March) there was basically no visible effect comparing reference runs (with 7-level TERRA_LM) and "High-Resolution-Levels" runs (HRL-runs; with 17 levels in soil model). And on the other hand, there were surprisingly significant impact during summer (May to July) - mainly on air temperature and dew point temperature (see figures below). These changes of results were mostly observed at mid latitudes of territory of Poland (in-between seashore and mountains). In most of these cases the changes of results effected in an improvement in forecast vs. observations. Basic statistical parameters - mean error and Root Mean Square Error (RMSE) of forecast - were smaller for HRL-runs in comparison with "reference" forecasts. What also should be noticed, computing time increased on average by less than 10% (from 5 to 8%).

Statistics	Mean Error		RMSE	
	Reference run	HRL-Run	Reference run	HRL-Run
Air temperature	-0.9	-0.4	6.9	6.0
Dew-point temp	-1.4	-1.1	7.4	6.6

Table 1: Basic statistics: forecasts against measurements at stations; 2012.07.29, 09:00 UTC

In next four charts selected results of mentioned comparison are shown.

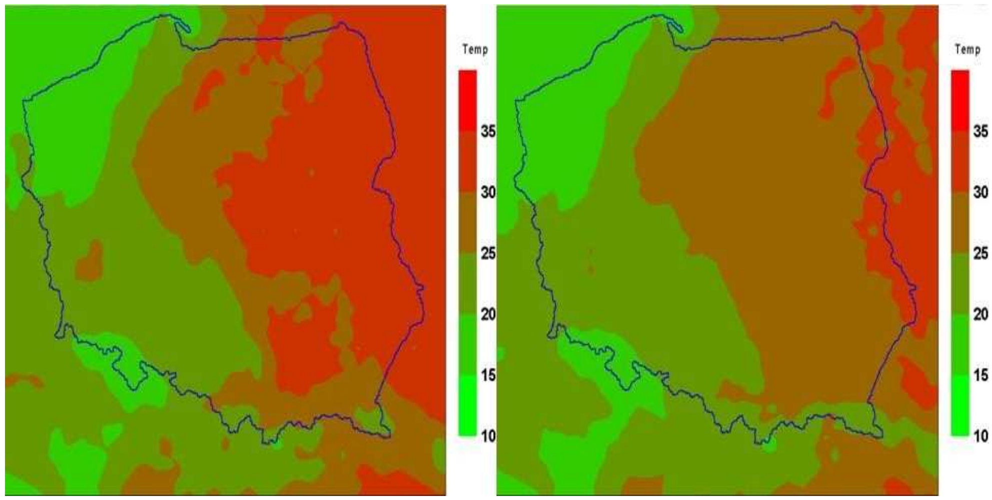

Figure 3: Forecast of air temperature at 2m agl., actual values of T2M, 2012.07.29, 09:00 UTC; reference run (left) vs. "high-resolution-levels" run (right).

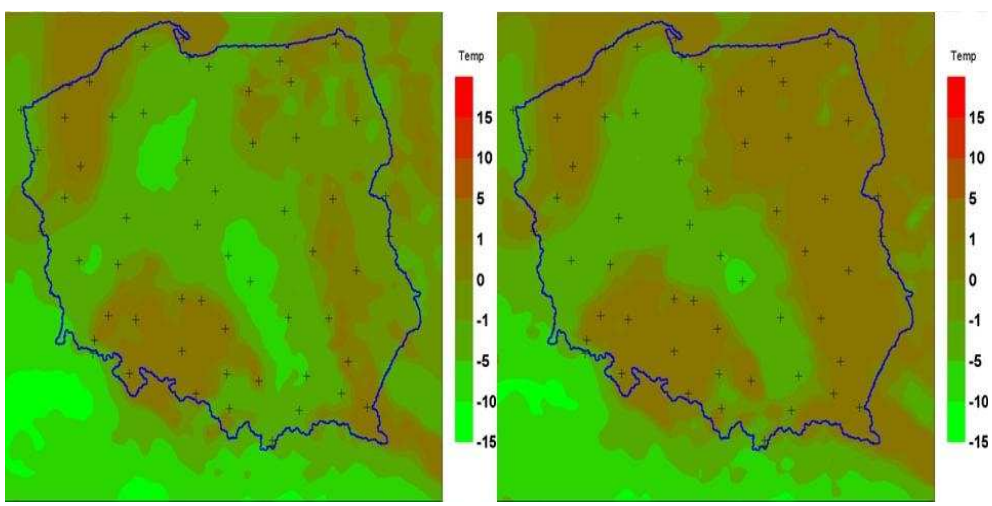

Figure 4: Air temperature at 2m agl., Observed-Forecasted, 2012.07.29, 09:00 UTC; reference run (left) vs. "high-resolution-levels" (right). Crosses mark meteorological stations where observations are continuously carried out.

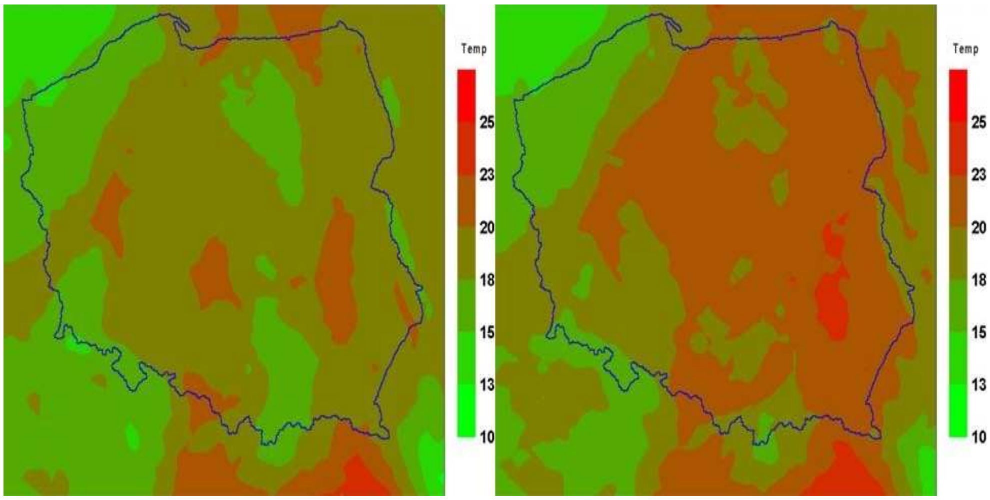

Figure 5: Forecast of dew point temperature at 2m agl., actual values of TD2M, 2012.07.29, 09:00 UTC; reference run (left) vs. "high-resolution-levels" run (right).

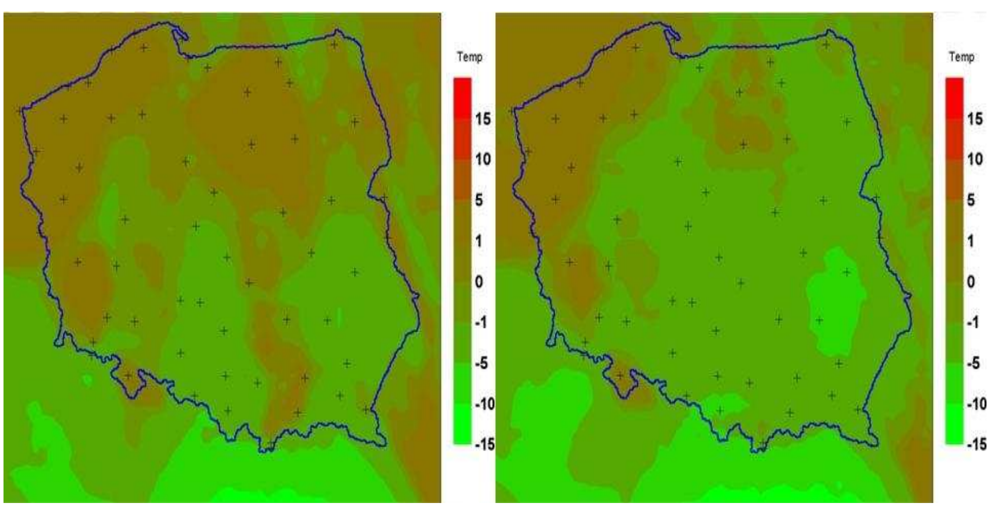

Figure 6: Dew point temperature at 2m agl., Observed-Forecasted, 2012.07.29, 09:00 UTC; reference run (left) vs. "high-resolution-levels" (right).

4 Discussion

In general, the improvement in forecasts is not adequate to authors expectations. Less than half of degree, in case both of temperature and dew point temperature is actually not much, taking into account that other meteorological parameters were not affected so ”strong”, i.e. changes were not so significant in case of other elements nor other time period. In authors opinion, no changes brought on during Winter/Spring might be a direct effect of ”frozen” ground - what could actually stopped most of heat- and water transfer via soil layers. Apparently, this ”high-resolution” approach was not a satisfactory step-forward to properly assess soil processes.

After a thorough consideration, authors came to the following conclusion: it seems that in order to obtain valid results, entirely new parameterization of soil processes may be needed to resolve the problem with proper accuracy. So, in authors opinion, this should be a direction for the future.

References

[1] Doms, G. and U. Schattler, 2002: A Description of the Nonhydrostatic Regional Model LM, Part I: Dynamics and Numerics, DWD.

[2] Doms, G., J. Forstner, E. Heise, H. - J. Herzog, M. Raschendorfer, T. Reinhardt, B. Ritter, R. Schrodin, J. - P.Schulz and G. Vogel, 2002: A Description of the Nonhydrostatic Regional Model LM, Part II: Physical Parameterization, DWD.

[3] Schattler, U., G. Doms and C. Schraff, 2009: A Description of the Nonhydrostatic Regional Model LM, Part VII: Users Guide, DWD.

[4] Ament, F. and C. Simmer, 2010: Improved Representation of Land - Surface Heterogeneity in a Non - Hydrostatic Numerical Weather Prediction Model (personal communication).

[5] Stensrud, D. J., 2007: Parameterization Schemes - Keys to Understanding Numerical Weather Prediction Models, Cambridge University Press.

[6] Cotton, W. R. and R. A. Anthes, 1989: Storm and Cloud Dynamics, Academic Press, INC.

[7] Smith, R. K., 1997: The Physics and Parameterization of Moist Atmospheric Convection, Kluwer Academic Publishers.

[8] Tiedtke, M., 1989: A comprehensive mass flux scheme for cumulus parameterization in large scale model, *Mon. Wea. Rev.*, **1779 - 1800**.

[9] Jacobson, M. Z., 2000: Fundamentals of Atmosferic Modeling, Cambridge University Press.

[10] Mellor, G. and T. Hamada, 1982: Development of a turbulence closure model for geophysical fluid problem, *Rev. Geophys. and Space Phys.*, 20, **851 - 875**.

[11] Mellor, G. and T. Hamada,1974: A hierarchy of turbulence closure models for planetary boundary layers, *J. Atm. and Space Phys.*, 31, **1791 - 1806**.

[12] Rewut, I. B., 1980: Soil physics (in Polish: Fizyka gleby), PWRiL.

[13] Duniec, G. and A. Mazur,2011: COLOBOC - MOSAIC parameterization in COSMO model v. 4.8, *COSMO Newsletter*, No. 11, **69 - 81**.

[14] Duniec, G. and A. Mazur,2012: Tests of TILES/MOSAIC parameterization in COSMO model, *COSMO Newsletter*, No. 12, **8 - 19**.

[15] Warner, T. T., 2011: Numerical Weather and Climate Prediction, Cambridge University Press.

On thunderstorm quantification

JAN PARFINIEWICZ

Institute of Meteorology and Water Management 61 *Podlesna str., PL*-01673 *Warsaw, Poland*

1 Introduction

The SAFIR/PERUN network system provides lighting information in six categories: cloud-to-ground (CG) flashes divided into return and subsequent strokes (Rs and Ss), intracloud discharges (IC), where the emission (nodal) points of IC strokes are subdivided into (ICs)tart, (ICi)ntermediate and (ICe)nd points and Isolated emission points (Is). This information is essential for implemented Thunderstorm Potential prediction system http://awiacja.imgw.pl/index.php?product=burze , Parfiniewicz, 2012. It occurred that one thunderstorm is not equal to another and special scale to (objectively) quantify (measure) thunderstorm activity is needed so that one can learn the system proper prediction. Operational monitoring of the tornados that were observed over Poland in summer season of 2012 showed that this extreme (Tornado or Downburst - ToD) events are strictly correlated to IC number of flashes [NoF] aggregated in cells over $\pi(15km)^2$ area within 10 minute interval.

2 Action & Result

The review of the polish press reports and investigation of the SKYWARN POLSKA http://lowcyburz.pl/ archives, including personal contact with A. Surowiecki (the Polish Skywarn representative) led to collecting twenty dates with extreme ToD events. More, A.Surowiecki has been given an eye-witness Fujita value to each event. Now, the statistics over 27887 aggregated cells, filtered in many possible ways has been constructed to fit to expected Fujita $[F]$ values. The best filter for strong ToD events with $[F] \geq 1$ (more or even) giving correlation $R \approx 0.85$ reads:

$[F] = a \times \sqrt{b \times ICs + c \times ICi} + d$ under condition $Rs > 1$ & $ICs > 70$ [NoF]

where: $a = 0.047$, $b = 0.7$, $c = 0.3$, $d = 0.22$
and ICs, ICi are measured in $[NoF/\pi 15km^2 \cdot 10min]$

For less severe events with $0 < [F] \leq 2.5$ another indicator-filter which includes CG flashes ($Rs > 0$) is being recommended:

$$[F] = a \times \sqrt{b \times ICs + c \times Rs + d \times \sqrt{ICs \times Rs}}$$

where: $a = 0.088$, $b = 0.624$, $c = 0.112$, $d = 0.264$.

3 Some statistics

Mean values of NoF for:

Is	ICs	ICi	ICe	Rs	Ss	
42.7	69.5	161.5	63.7	58.1	29.2	⇐ all aggregated cells
180.2	233.6	498.3	227.3	286.4	159.1	⇐ severe cells

Table 1: Mean values of NoF.

4 Caution

Presented numbers may strongly depend on sensitivity thresholds applied by PERUN producers to the particular application.

References

[1] Parfiniewicz J., 2012: Concerning Thunderstorm Potential prediction. *The European Meteorological Society Annual Meeting and 9th European Conference on Applied Climatology*, Łódź, Poland, 10-15 September 2012. Abstracts vol. **9**, EMS2012–81.

[2] http://meetingorganizer.copernicus.org/EMS2012/EMS2012-81.pdf

[3] http://presentations.copernicus.org/EMS2012-81_presentation.ppt

Operational multiscale modelling system for air quality forecast

Matteo Giorcelli[1,2], Stefano Bande[1], Massimo Muraro[1], Massimo Milelli[1]

[1] *ARPA Piemonte, Via Pio VII 9, 10135, Torino, Italy*

[2] *Arianet S.r.l, via Gilino 9, 20218 Milano, Italy*

1 Introduction

The EU legislation fosters the development and use of air quality modelling systems for both air quality assessment (AQA) and air quality forecast (AQF). The Air Quality Framework and Daughter Directives (1996/62/EC; 1999/30/EC, 2000/69/EC and 2002/3/EC) encouraged European air quality management and assessment institutions to implement air quality modelling as one of the main sources of information to support periodic air quality assessment. Moreover the new Air Quality Directive 2008/50/EC places more emphasis on, and encourages, the use of models in in a wide range of applications. The new directive requires the distribution of air quality information for current day, together with trend and forecast for the next days and for the implementation of short term action plans, when concentrations are expected to exceed alert and information thresholds. Several scientific projects and initiatives have been supported by EU to enhance international cooperation on integrated meteorological and air quality modelling (COST 728) and on air quality forecast (COST ES0602, 5FP project FUMAPEX and 6FP project GEMS), and to promote the use of modelling for regulatory purposes (FAIRMODE). Different air quality modelling and forecasting system are presently in operational and pre-operational phase over Europe. Over the last few years ARPA Piemonte, taking advantage of the knowledge acquired during the 5FP project FUMAPEX, has developed a multi-scale air quality modelling system (Bande et al., 2007, Finardi et al., 2008) based on Eulerian chemical transport model. The operational version of this modelling system uses meteorological fields provided by COSMO-I7 to produce daily air quality forecasts. The following sections briefly describe the forecasting system architecture and present an overview of the modelling system performances; conclusions and future works are presented in the last section.

2 Air quality forecasting system description

The forecasting system has been built by using state-of-the-art techniques for atmospheric transport and dispersion modelling. The computational system architecture, sketched in Figure 1, is modular, so that the model inter-dependence is limited, in order to facilitate system improvements without modifying the general structure. The core of the system is represented by the air quality model FARM (Flexible Air Quality Model), three-dimensional Eulerian model that accounts for transport, chemical conversion and deposition of atmospheric pollutants (Gariazzo et al, 2007). The forecasting system needs a series of detailed input datasets: emission inventories, geographic and physiographic data (to describe topography, surface land cover and urban details), large scale air quality and meteorological forecasts. Some specific modules are needed to process these data in order to produce emissions, meteorological fields and boundary conditions necessary as input to the air quality model. Emission data (point, line and area sources) coming from different resolution inventories available over all computational domains are processed by a specific emission module in order to produce gridded hourly emission rates for all the chemical species considered by the air quality

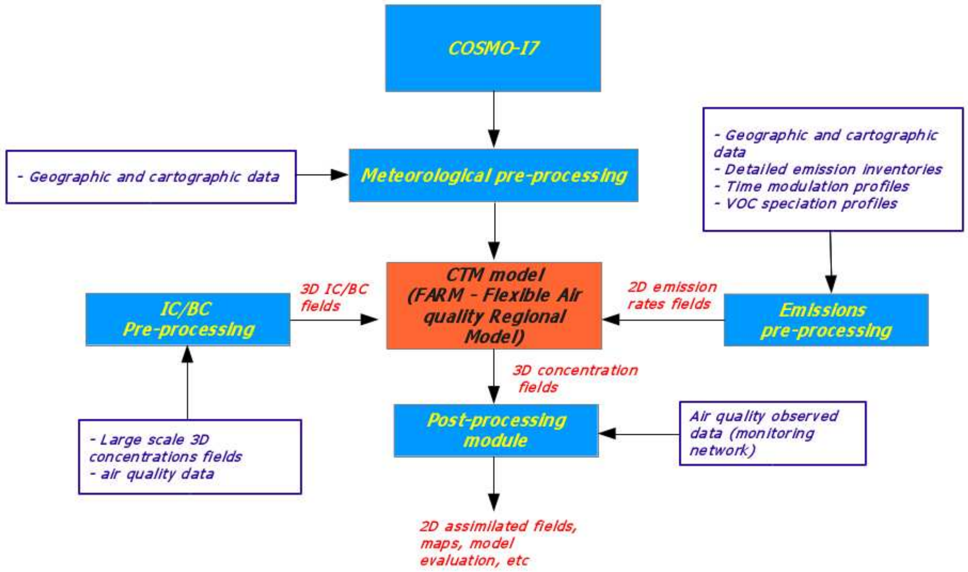

Figure 1: Forecasting system architecture.

model. This pre-processing system allows non-methanic hydrocarbon speciation and flexible space and time disaggregation, according to cartographic thematic layers and specific time modulation profiles (yearly, weekly and daily). The meteorological fields are provided by 00 UTC runs of COSMO-I7. The COSMO model levels fields are directly interpolated and adjusted (forced to be non-divergent) over all the computational domains by an interface module GAP/SURFPRO (Calori et al., 2006). GAP is a grid interpolation tool interfacing the chemical transport model FARM with any numerical weather prediction model. GAP interpolates a sequence of 2D and 3D atmospheric fields from a source grid identified by mesh points, geographic coordinates and altitudes, to a target grid defined using UTM projections and terrain-following vertical coordinates. Finally, starting from topography and land-use data managed by the modelling system and gridded fields of meteorological variables provided by COSMO-I7, SURFPRO (SURface-atmosphere interFace PROcessor) computes three-dimensional fields of horizontal and vertical diffusivity and two-dimensional fields of deposition velocities for a given set of chemical species. The initial and boundary conditions for the background domain are obtained by continental scale air quality forecasts provided by PrevAir European Scale Air Quality Service (http://www.prevair.org). The AQF modelling system performs simulations over three nested domains (Figure 2):

- a background domain, covering Po valley basin and the Alps, with an horizontal resolution of 8 km;
- a regional target domain, covering the whole Piemonte Region with an horizontal resolution of 4 km;
- three inner domains, with 1 km horizontal resolution, centred over Torino metropolitan area, Novara and Alessandria cities.

This multi-scale approach allows to take into account the effect of sources located outside the target areas, and to better describe phenomena characterized by large spatial scales, such as photochemical smog and particulate matter accumulation processes. The forecasting system runs on a daily basis in order to produce air quality forecasts for current day and the two days

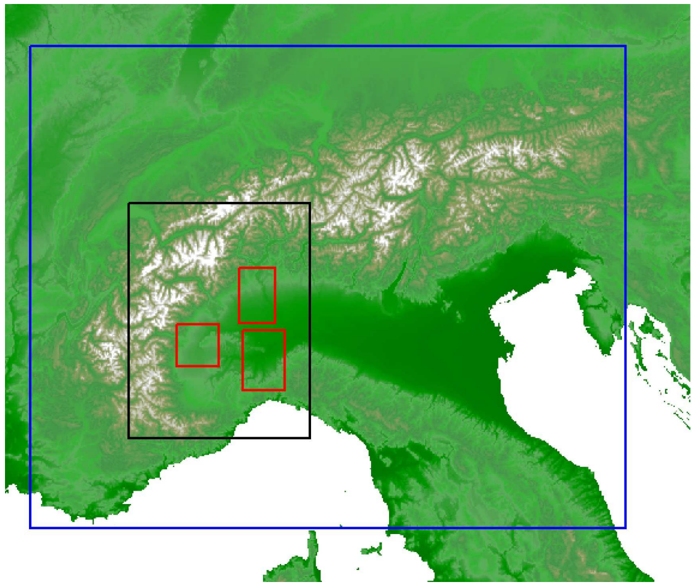

Figure 2: Forecasting system computational domains.

after, with one hour time resolution. The operational chain is organized in two main steps: during the first step the input data are acquired and processed, in the second step the air quality simulations are performed in two-way nesting mode. Finally, a post-processing phase followed by a product dissemination is carried out in order to produce the concentrations maps, to calculate all the air quality indicators required by the EU legislation and the Torino metropolitan area Air Quality Index (Giorcelli et al., 2008).

3 Overview of air quality forecasting system results

In this section we present an overview of the main results over the regional domain referred to almost one year period, from February 2012 to December 2012. The reliability of prediction for NO_2, PM_{10} and O_3 has been verified through comparison between the observed data coming from the regional air quality monitoring network and the simulated ones at corresponding station coordinates. Long term model performances have been evaluated using three statistical indexes selected among the more frequently used in air quality model evaluation studies: fractional bias (FB), root mean square error (RMSE) and Pearson correlation coefficient (ρ). The definition of the first two indexes is described below, where N is the number of observed-predicted data couples for each monitoring site, O_i and P_i represent respectively the ith observed and predicted values,and $\bar{O}$ and $\bar{P}$ the corresponding mean values.

$$FB = 2\frac{\bar{O}-\bar{P}}{\bar{O}+\bar{P}} \; ; \; RMSE = \sqrt{\frac{1}{N}\sum_{i=1}^{N}(O_i - P_i)^2}$$

The results of model evaluation are reported in Table 1, while in Figure 3 are shown the box plots of observed and predicted concentrations in some monitoring stations for NO_2 (monthly distribution hourly mean) and O_3 (monthly distribution of daily maximum 8-hour running average). The comparison over a long period, including summer and winter months, underlines the modelling system capability to reproduce accurately seasonal and daily trends for all considered pollutants, with satisfactory correlation in almost stations and limited values of FB and $RMSE$; nonetheless all the considered stations show an underestimation ten-

Table 1: Statistical indexes for the validation sites

	PM_{10}			NO_2			O_3		
Station	*FB*	*RMSE*	ρ	*FB*	*RMSE*	ρ	*FB*	*RMSE*	ρ
Alba	0,646	25,757	0,528	0,456	18,903	0,596	0,017	23,687	0,852
Alessandria-Volta	0,507	29,968	0,539	0,41	27,266	0,463	-0,069	23,59	0,878
Asti	n.a.	n.a	n.a	0,23	18,231	0,656	0,027	22,758	0,872
Biella	0,312	14,548	0,517	0,11	15,342	0,62	0,09	20,822	0,879
Borgosesia	0,74	19,53	0,497	0,507	15,598	0,526	0,089	24,913	0,844
Cuneo	0,407	19,552	0,323	0,182	20,591	0,327	0,087	20,816	0,847
Cossato	0,599	19,276	0,594	0,424	16,183	0,709	-0,09	23,358	0,823
Dernice	0,385	12,188	0,425	0,4	8,279	0,573	0,014	24,713	0,783
Druento	0,465	20,243	0,426	-0,071	17,899	0,386	0,209	29,943	0,809
Novara-Verdi	0,351	19,863	0,519	0,103	18,729	0,619	0,029	22,923	0,875
Orbassano	n.a.	n.a	n.a	-0,045	21,689	0,535	0,266	31,041	0,808
Torino-Lingotto	0,081	25,222	0,582	-0,394	37,469	0,361	0,309	30,19	0,836
Vercelli-Coni	0,527	24,767	0,478	0,048	16,44	0,555	0,191	26,923	0,873
Verbania	0,587	16,826	0,388	0,427	16,684	0,526	-0,036	21,203	0,862
Vinchio	0,401	19,328	0,583	0,043	9,986	0,685	0,136	30,086	0,802
Vinovo	n.a.	n.a	n.a	-0,02	25,264	0,374	0,143	27,672	0,787
Torino-Consolata	0,245	27,181	0,608	0,006	27,029	0,467	n.a.	n.a.	n.a.

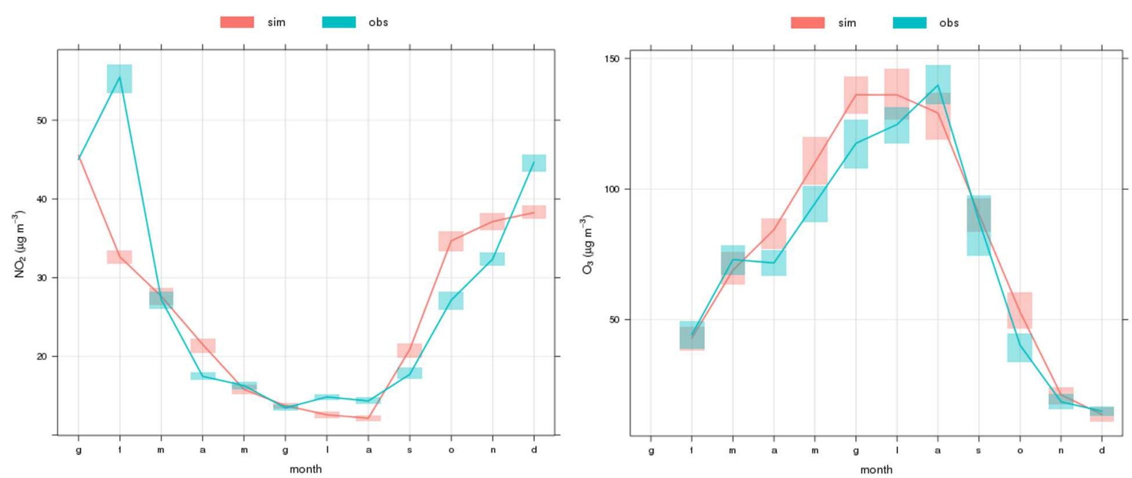

Figure 3: Box plots of observed (cyan) and predicted (pink) distributions: NO_2 hourly mean monthly distribution, Vercelli-Coni urban background station (left) and O_3 daily maximum 8-hour running average monthly distribution, Alessandria-Volta urban background station (right).

dency during wintertime. The statistical evaluation of results can be considered satisfactory for long term applications finalised to air quality assessment. The main request for those simulation is therefore to reproduce concentration distribution, providing a reliable evaluation of average and peak values through the estimation of indicators prescribed by EU directives. The requests become more stringent for air quality forecast, when concentration variations should be described with the correct space and time correlation. For a better insight of the possible influence on air quality simulations of meteorological fields, the time series of computed and observed concentrations have been analysed, with particular attention to air pollution episodes characterised by relevant time variation of measured concentrations. The comparison of time series (Figure 4) in two urban monitoring sites located in Torino and

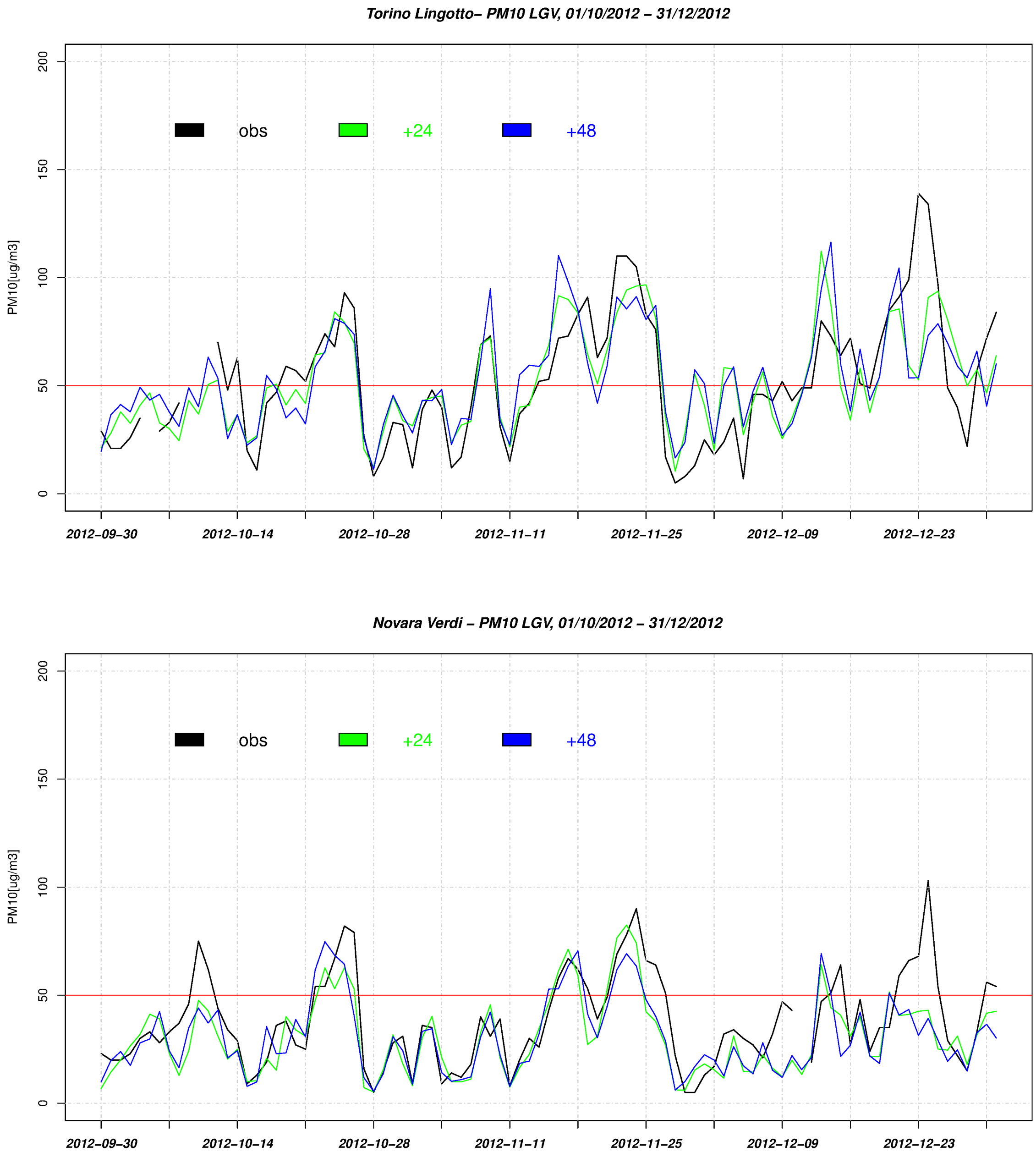

Figure 4: Time series of observed (black line) and predicted (green line +24 forecast, blue line +48 forecast) PM_{10} daily mean concentrations for the last three months of 2012: Torino-Lingotto (top) and Novara-Verdi (bottom) urban background stations.

Novara cities, shows that COSMO-I7 fields can provide a satisfactory capability to simulate meteorological forcing that can cause peak pollution episodes, even if weather forecast errors cause the occurrence of *false alarm* conditions with concentration overestimation.

4 Summary and Outlook

The analysis of results obtained by multiscale air quality forecasting system has confirmed its capability to forecast air pollutant episodes, concentration trends and mean levels. Some difficulties were found in the simulation of NO_2 and PM_{10} winter concentrations; this is probably due to a lack in domestic heating and vehicular traffic emissions estimation, but also to an insufficient description at locale scale of accumulation phenomena. In the near future, we are going to use COSMO-I2 as meteorological driver over target high resolution domains in order to provide a better reproduction of surface meteorological variables at locale scale. A second aim is to develop a near real time modelling system based on COSMO-I2 analysis (Galli et al., 2011) to provide daily analysis of previous day air quality levels.

References

[1] Bande S., Clemente M., De Maria R., Muraro M., Picollo ME., Arduino G., Calori G., Finardi S., Radice P.,Silibello C., 2007: The modelling system supporting Piemonte region yearly air quality assessment. *Proceedings of the 6^{th} International Conference on Urban Air Quality*, Limassol, Cyprus.

[2] Bande S., D'Allura A., Finardi S., Giorcelli M., Muraro M., 2008: Meteorological modelling influence on regional and urban air pollution predictability. *Croatian Meteorological Journal*, 43, p. **613-617**.

[3] Calori, G., Clemente, M., De Maria, R., Finardi, S., Lollobrigida, F., Tinarelli, G., 2006: Air quality integrated modelling in Turin urban area. *Environ. Model. Softw.*, 21 (4), **468-476**.

[4] Finardi, S., De Maria, R., D'Allura A., Cascone C., Calori G., Lollobrigida F., 2007: A deterministic air quality forecasting system for Torino urban area, Italy. *Environ. Model. Softw.*, 23 (3), **344-355**.

[5] Galli M., Milelli M., Cassardo C., 2011: The effects of T2m assimilation on surface fluxes in COSMO-I2. *COSMO Newsletter*, No. 11, **3-21**.

[6] Gariazzo C., Silibello C., Finardi S., Radice P., Piersanti A., Calori G., Cucinato A., Perrino C., Nussio F., Cagnoli M., Pelliccioni A., Gobbi G.P., Di Filippo P., 2007: A gas/aerosol air pollutants study over the urban area of Rome using a comprehensive chemical transport model. *Atmospheric Environment*, 41, **7286-7303**.

[7] Giorcelli M., Pallavidino L., Bande S., Bertello A., D'Allura A., Finardi S., Muraro M., Pavone F., Prandi R., 2010: Public information under the new 50/2008/EC Directive: an example of Air Quality Forecast Index. *Proceedings of 13^{th} International Conference on Harmonisation within Atmospheric Dispersion Modelling for Regulatory Purposes*, Paris, France.

Using synoptic classification to evaluate COSMOGR through Weather Dependant Verification

Gofa F.[1] and Tzeferi D.[1]

1: Hellenic National Meteorological Service (NHMS)

1 Introduction

With the multiplicity of weather prediction models and their fast-growing evolution, it is sometimes difficult for the forecaster to have an objective opinion regarding their quality. Verification analysis issued by the modelers is often not precise enough to be used as a guideline for a correct forecast. On the one hand, the forecaster would like to know when they can trust the model, on the other hand, the modeler would like to know when the model is not performing well in order to make improvements. To answer these questions, can be necessary to differentiate between different weather situations, by appropriately stratifying the verification dataset. One might suspect that the performance in winter and in summer could be different, or that, for instance, model performance in anticyclonic conditions may differ from that in a vigorous northerly flow. These differences may depend also on the geographical location, especially with respect to the presence of a land-sea border or mountains. Monthly, seasonal and annual statistical verifications are limited in that their performance is averaged over the whole spectrum of weather types the atmosphere can produce. The danger is that they can mask differences in forecast quality when the data are not homogeneous, even in terms of flow regimes.

During this study, a weather-based stratification was applied before the verification process took place. In this way, systematic model errors during the various synoptic situations could be identified.

2 Methodology of Classification

A weather type classification is a method which distinguishes between meteorological situations describing them in accordance with circulation parameters (e.g. zonality, cyclonality, position of low and high pressure systems, etc.) or local weather elements such as temperature or precipitation. Circulation parameters are often preferred since such parameters can be used very easily to relate certain features of the atmospheric circulation with local weather by statistical methods. The large number of different methods applied for classification of weather types implies open challenges to the meteorological-climatological communities [2]. The type of classification is usually adapted to a specific region and is not easily transferable to another region, or it is focused on the analysis of a specific problem so the temporal and spatial scales are adjusted accordingly.

With the aim of gaining a better understanding of model behaviour for the various types of weather that influence our area of interest, a subjective classification was adopted that is based mainly on the basic circulation patterns that the forecasters at HNMS come across in their daily experience. This tailor-made classification scheme comprises 12 different weather classes which describe the synoptic situation of the 500hPa at 12 UTC on a daily basis, with a geographical focus on the Greek region. These classes roughly separate the different weather situations into advective classes (e.g. 'northwest', 'southeast') and the accompanied convective classes 'anticyclonic' and 'cyclonic'.

Figure 1: Graphical representation of the weather classes used.

Each of these categories is related to specific weather phenomena, the intensity and amplitude of which depend greatly on the season. The categories used are presented in fig. 1 with an example of the graphical representation of the circulation. The time period covered by the study was 1 December 2009 to 30 June 2011.

Zonal C	Zonal AC	N-NW C	N-NW AC	N-NE C	N-NE AC	S-SW C	S-SW AC	S-SE C	S-SE AC	Cut-off low	Stat/ry AC
28	14	10	2	2	1	21	6	1	1	11	4

Table 1: Percentage of days in each weather regime (total number of days 577)

Table 1 shows the relative percentage of days that fall into each weather category. Particular attention must be given to gathering large enough samples to provide trustworthy verification results, i.e. interpretation of verification results for classes 'N-NE' and 'S-SE' for both convective classes is limited.

3 Results

The following section presents some of the results of the verification of the continuous and non-continuous surface parameters for the period: December 2009 - June 2011. The verification of continuous variables (e.g. T2m, Td2m, MSLP, wind speed) is typically performed using statistics that show the degree to which the forecast values differ from the observations. The Mean Error (ME) and the Root Mean Square Error (RMSE) are simple indices that provide useful information about the model's performance for a given weather parameter for a given location. Thus, for all continuous weather parameters, 3-hourly forecast values for a horizon of 72h of the 00UTC model runs were compared against the respective SYNOP data.

Looking at the overall 2m temperature verification graphs (fig. 2) for each classification class, one can identify some characteristics common to all classes. These include the distinct daily cycle of both ME and RMSE and the general trend of underestimation of temperature by the forecast model. Looking into characteristics that are related to each circulation, it can be noted that for the northern weather systems (fig. 2 c,d,e,f), there is a colder bias (underprediction) of the 2m temperature in comparison with the weather systems originating from the south. The value of ME is respectively a bit higher, and in general terms the model has a discrepancy of approximately $2 - 3^oC$.

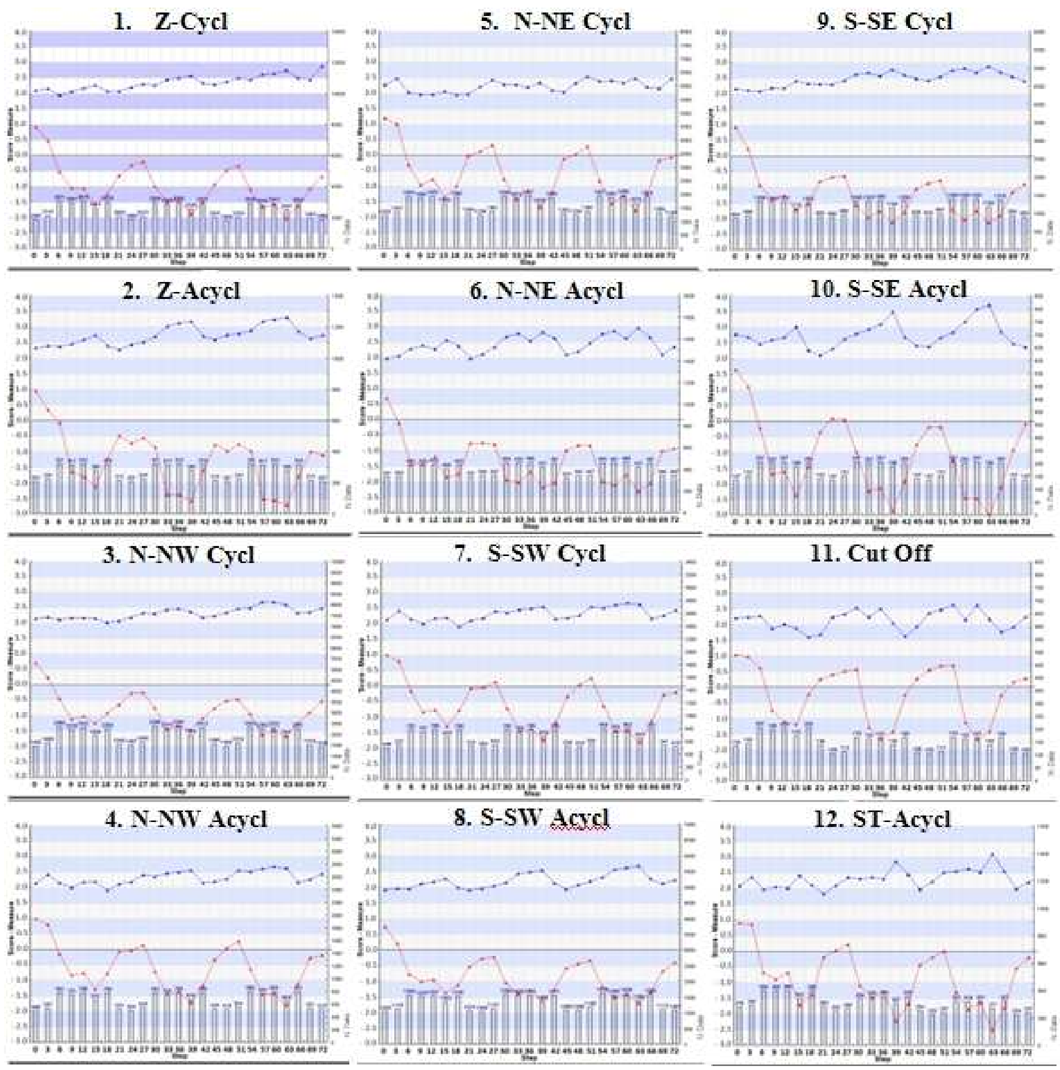

Figure 2: 2m Temp RMSE (blue) ME (red) for stratified forecasts against 80 weather stations.

A weather parameter that most if not all NWP models fail to predict correctly is the amount of clouds. COSMO-GR produces subgrid scale cloudiness using an empirical function that depends on relative humidity and height. Looking the calculated ME and RMSE for each weather type (fig. 3), we can see large differences in the ability of the model to correctly estimate the amount of clouds for each weather pattern. The error seems to be connected mainly with the cyclonality with improved performance during the passage of low pressure systems versus stable anticyclonic conditions.

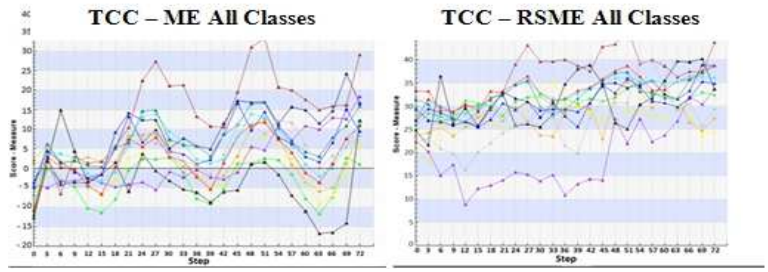

Figure 3: Cloud cover: ME (left) and RMSE (right) values for all weather classes.

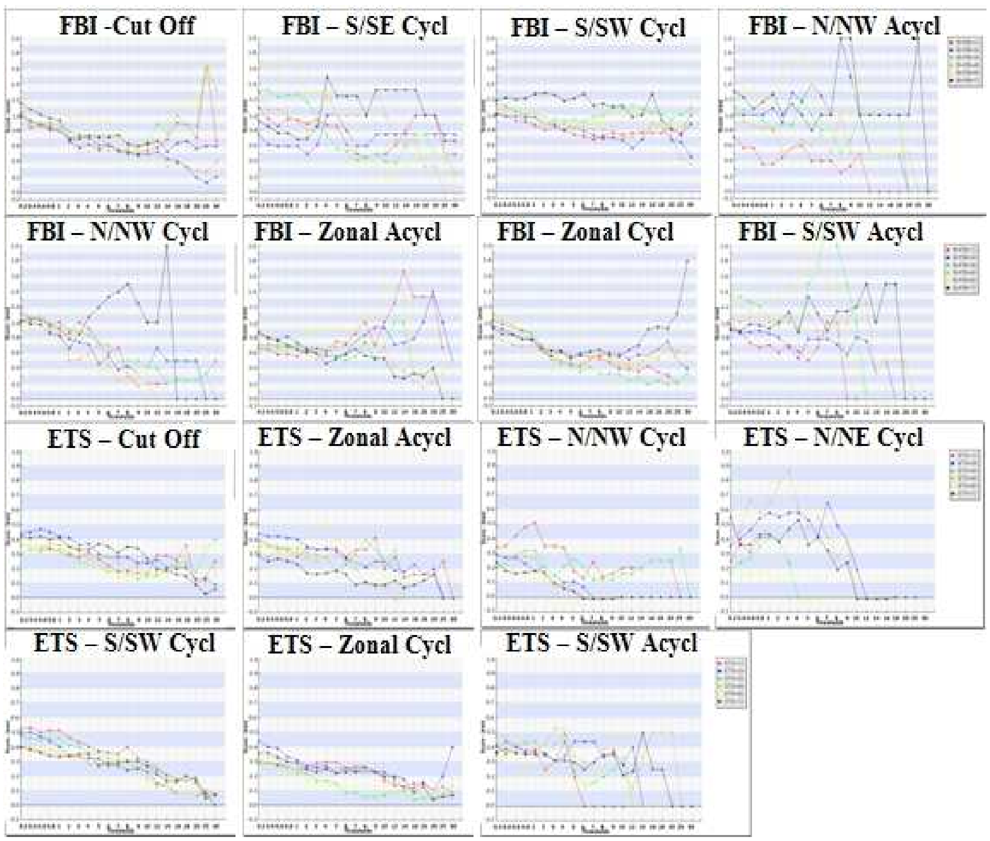

Figure 4: FBI (top rows) and ETS (bottom rows) for 12h precipitation forecasts (selected cases).

Precipitation is commonly accepted as the most difficult weather parameter to correctly predict in terms of its spatial and temporal structure due to its stochastic behaviour and any connection with specific weather systems is greatly appreciated by forecasters. The 12h-hour precipitation amounts were verified for this study and the thresholds for the precipitation amounts ranged from 0.2mm up to 30mm accumulated over each time interval. For each threshold a number of scores were calculated that provide insight into model behaviour, the most representative of which are shown in fig. 4.

The Frequency Bias (FBI) is a measure of comparison between the frequency of forecasts to the frequency of occurrences (range: $0-\infty$, perfect score$=1$, $FBI > 1$ indicates over-forecast) while the Equitable Threat Score (ETS) is a measure of the fraction of correctly predicted events, adjusting for random hits (range: $-1/3-1$, perfect score$=1$). In the case of precipitation, statistical indexes worsen when model resolution is increased as it produces better defined mesoscale structures, higher amplitude features and larger gradients, and inevitably leads to increased spatial and temporal errors. The results indicate that the COSMO-GR model performs well for the thresholds corresponding to small amounts of precipitation, but it fails to accurately predict large rainfall events. In cases that there was precipitation during a substantial number of days, FBI index results indicate that there is an overprediction for the lower thresholds during all cyclonic circulations, independent of the origin of the system, meaning that the model was giving us more often precipitation than truly occurred. On the other hand, the model underforecasts precipitation during heavy rainfall events ($> 8mm$), especially during anticyclone circulations. The ETS index, which provides a measure of the general performance of the model, reduces dramatically as the precipitation threshold increases. After measuring this index for all the statistically significant weather classes, it was discovered that precipitation forecasts were more successful for weather systems originating from the south-west, but this behaviour can only be better understood if a seasonal analysis is performed.

4 Conclusions

A systematic weather dependent comparison of forecast weather parameters with synoptic station measurements has been presented for the period of 2010-2011. In summary, the analysis identified: a colder bias of the 2m temperature during the passage of weather systems originating from the north, a reduced 10m wind speed error for all anticyclonic convective classes, an improved performance of cloud cover prediction when low pressure systems are present and, finally, an overprediction of the precipitation for all cyclonic circulations for the lower thresholds of precipitation, independent of the origin of the system. The limitations of this study are related to the lack of large samples for every weather class. Moreover, the weather classification scheme that was followed is not specifically geared to a specific weather parameter and may, not be the optimal choice every time.

References

[1] Gofa F., A. Raspanti, T. Charantonis, 2010: Assessment of the performance of the operational forecast model COSMOGR using a conditional verification tool. In Proc 10^{th} COMECAP Conference of Meteorology, Patras. Greece, Hellenic Meteorological Society.

[2] Maheras P., 1988: The synoptic weather types and objective delimitation in the winter period in Greece. Weather 43: 40-45.

Tropospheric Delay (ZTD) and Precipitable Water data from COSMO model vs. geodetic GPS network data

Michał Kruczyk[1] and Andrzej Mazur[2]

1: Faculty of Geodesy and Cartography, Warsaw University of Technology Pl. Politechniki 1, PL-00-661, Warsaw, Poland

2: Institute of Meteorology and Water Management - National Research Institute 61 Podleśna str., PL-01 673, Warsaw, Poland

1 Introduction

Atmospheric refraction is topic of great concern in satellite geodesy. Refraction of Global Positioning System (GPS) L-band navigational signal manifests itself in the form of Tropospheric Delay. For the satellite in zenith, tropospheric delay (here Zenith Tropospheric Delay ZTD) on station at the sea level is around 2.3 m. Valuable geodetic coordinate solutions for antenna phase center should be at centimetre level (daily solutions). There are two approaches to eliminate tropospheric delay in GPS solutions (and other satellite positioning systems and VLBI). First is to model ZTD from surface meteorological parameters by means of rather coarse equations ([7], [4]) and next we transform it to satellite elevation by so called 'mapping function'; second emphasizes optimal construction and solution of observational equation system so tropospheric delay is estimated stochastically together with coordinates. Advanced GPS software practically mixes both methods [3] starting with model ZTD value and estimating values for each station in selected intervals (mostly 1 hour or as random walk). In some special cases WVR (Water Vapour Radiometers) are used to directly measure most variable (and problematic) part of atmospheric delay coming from water vapour.

In case of permanent GPS stations maintained for most precise scientific purposes (plate tectonics etc.) ZTD is also estimated for purposes of atmospheric research: so called 'GPS meteorology' [5]. Notion of 'GNSS meteorology' is more frequently used ($GNSS = GPS + Glonass + Galileo$). This new discipline is now quite advanced: in some cases at the level of operational assimilation of GPS data to numerical weather prediction models (e.g. NOAA RUC).

We describe several interesting results of IPW and ZTD time series comparisons and analyses. Greatest attention is paid to IPW (Integrated Precipitable Water) - important meteorological parameter easily derivable from GPS tropospheric solutions (ZTD's). We have made quite many comparisons of different static solutions (mainly IGS and EPN) and input fields of operational numerical weather forecast model COSMO (maintained by Polish Institute of Meteorology and Water Management).

2 Zenith Tropospheric Delay and Precipitable Water in satellite geodesy

Networks of GNSS receivers and dedicated solutions are coordinated in the frame of two organizations: IGS International GNSS Service (global reach) and European (EUREF) Permanent Network (EPN).

Total Zenith Delay above all stations in the network became one of the standard products of IGS (from 1998) and EPN (from 2001). It is created as a combination of individual

Local Analysis Center's solutions (EPN has 16 such centers and each station is calculated independently by 3-4 centers) or special solution using 'final' sub-products orbits, clocks etc. (IGS, [2]). In our paper we describe results of only these two official solutions, but many other are available or in development.

IPW (Integrated Precipitable Water) sometimes defined simply as PW describes quantity of water vapour in the vertical direction over station in mm of liquid water after condensation. Related parameter IWV (Integrated Water Vapour) is used more frequently - it has the same numerical value but another unit of measure: g/m^2. IPW can be calculated from ZTD by known procedure of separating ZHD (Zenith Hydrostatic Delay) and recalculating obtained ZWD (Zenith Wet Delay) by numerical coefficient dependent on so called 'mean temperature' in vertical profile of atmosphere ([1], [6]).

Separation of hydrostatic and wet part of delay involves using some model of ZHD (Zenith Wet Delay - in our work Saastamoinen formula with gravitational correction):

$$ZWD = ZTD - ZHD$$

Next we recalculate ZWD to IPW by

$$IWV \approx k \cdot ZWD$$

Coefficient k is given by equation

$$\frac{1}{k} = 10^{-6}(\frac{C_3}{T_m} + C_2')R_v$$

and has value of about $\frac{1}{6.4}$ $\{R_v$ is specific gas constant for water vapour, T_m - 'mean temperature', C_x are empirical coefficients given in many versions by different sources$\}$. Coefficient k depends on temperature profile but can be estimated by means of surface temperature at the GNSS station.

In short: ZHD is function of surface pressure (sometimes also temperature) and k of temperature. GPS meteorology needs stations to be equipped with meteorological device but it is true only for about 20% of EPN network. Fortunately in case of comparisons with COSMO results we can use values interpolated from model grid.

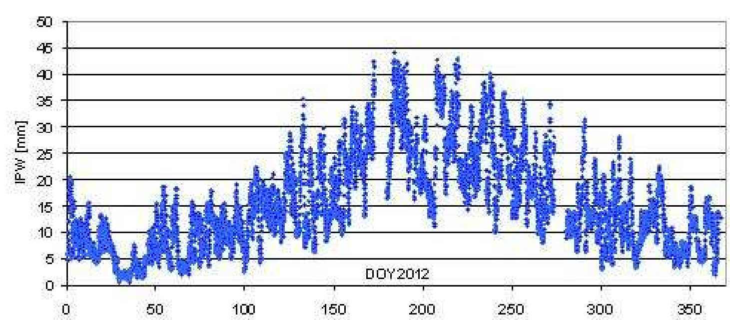

Figure 1: Precipitable water from EPN GNSS combined solution for station JOZE (Warsaw University of Technology Astro-Geodetic Observatory) in 2012

Most direct meteorological data to calculate IPW are free radiosoundings (RAOB) carried out 1 - 4 time a day in some cases at points close to GNSS station.

radiosounding point		GPS	distance [km]	RAOB point height [m]	bias [mm]	mean absolute bias [mm]	difference std dev [mm]	difference RMS [mm]	no of points
3238	UK Albemarle	MORP 13299S001	24.89	141	-0.65	1.11	1.39	1.54	325
6610	SW PAYERNE	ZIMM 14001M004	39.67	490	2.85	2.89	1.63	3.29	679
8522	PO Funchal	FUNC 13911S001	2.14	56	-0.59	1.2	1.49	1.6	319
11520	CZ PRAHA-LIBUS	GOPE 11502M002	25.87	303	2.43	2.47	1.56	2.89	1224
11747	CZ Brno/Prostejov	TUBO 11503M001	42.64	216	0.5	1.62	2.01	2.07	665
12120	PL LEBA	REDZ 12227M001	40.74	2	0.7	1.49	1.88	2.01	466
12374	PL LEGIONOWO	BOGI 12207M003	9.43	96	0.83	1.38	1.68	1.87	300
12374	PL LEGIONOWO	BOGO 12207M002	9.53	96	1.18	1.47	1.42	1.85	382
12374	PL LEGIONOWO	JOZ2 12204M002	33.85	96	1.07	1.46	1.51	1.85	718
12374	PL LEGIONOWO	JOZE 12204M001	33.96	96	0.53	1.23	1.6	1.68	722
12425	PL WROCLAW I	WROC 12217M001	12.73	122	0.2	0.91	1.2	1.21	681
16754	GR HERAKLION (AIR	TUC2 12617M003	103.03	39	1.28	2.51	2.82	3.1	348
17062	TU ISTANBUL/GOZTE	ISTA 20807M001	15.75	33	1.48	1.72	1.7	2.26	653
17130	TU ANKARA/CENTRAL	ANKR 20805M002	12.54	894	0.67	0.97	0.99	1.2	546
10200	DL EMDEN-FLUGPLAT	BORJ 14268M002	44.65	1	0.93	1.86	2.31	2.49	329
10113	DL Norderney	BORJ 14268M002	31.59	11	0.48	1.84	2.6	2.65	336
10035	DL SCHLESWIG	HOE2 14284M002	84.79	48	2.93	3.34	3.2	4.34	459
10393	DL LINDENBERG	POTS 14106M003	73.82	115	1.58	1.86	1.65	2.28	317
10410	DL ESSEN	EUSK 14258M003	82	152	0.61	1.32	1.63	1.74	145
10771	DL KUEMMERSRUCK	WTZR 14201M010	77.8	419	1.89	2.17	1.81	2.61	1373
4270	GL Narsarsuaq	QAQ1 43007M001	61.54	4	-0.1	1.13	1.55	1.55	715
4018	IS Keflavikurflug	REYK 10202M001	36.58	54	-0.18	0.86	1.18	1.19	691
26702	RU Kaliningrad	LAMA 12209M001	89.9	21	3.44	3.94	3.46	4.87	484

Table 1: Comparison of selected radiosoundings and nearby GPS stations (EPN combined tropospheric solution) in 2011. All results are given in values of IPW.

Note: mean bias for all 23 stations (RAOB - GNSS) is 1.05 mm, so GPS IPW values are on average smaller than radiosounding, (difference standard deviation 1.84 mm, difference RMS 2.27 mm)

3 Tropospheric Delay and Precipitable Water from COSMO model(s) (IMWM)

We can treat input fields of numerical weather prediction models (after assimilation/analysis) as a meteorological database. We tested this for main synoptic model in Poland: COSMO model maintained by Polish Institute of Meteorology and Water Management (IMWM) in Warsaw both in 14 km and 2.8 km resolution version.

The 14 km model has a grid of 183×161 points, 36 vertical levels (35 half-levels), the 2.8 km version 285×255 grid and 50 half-levels. Both are restarted twice a day (00 UT and 12 UT) so we use also first three forecast steps ($T + 3h$, $T + 6h$ and $T + 9h$) to get 3h temporal resolution.

Grid has rotated equator and 0 meridian to minimize deformations making typical map projections inadequate - so sometimes we use original grid for mapping results.

For all grid points we can calculate zenith tropospheric delay and interpolate it for about 160 EPN GPS stations located in the model area in two ways:

- hydrostatic (ZHD as function of surface pressure and station coordinates, ZWD integrated in vertical direction together with IPW)
- direct integration of refractivity profile utilizing one of formulas developed in geodesy ([8], [9] etc.).

$$ZTD = 10^{-6} \int N ds$$

For refractivity we used formula proposed by Thayer (1974):

$$N_m = (n_m - 1) \cdot 10^{-6} = 77.60\frac{p}{T} - 13\frac{e}{T} + 3.78 \cdot 10^5 \frac{e}{T^2}$$

{p - pressure, T - temperature [K], e - water vapour partial pressure}

The ZTD map is of course dominated by topography:

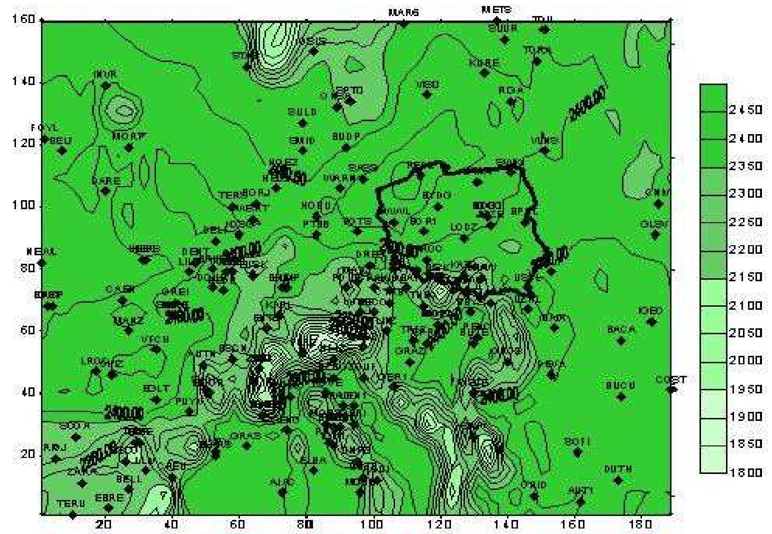

Figure 2: Map of ZTD [mm] calculated (hydrostatic method) from COSMO_14 fields May 17^{th} 2011 15:00 TU (first forecast step) in model grid

First results of comparisons: EPN combined tropospheric product - COSMO derived ZTD have shown dramatic extremes for mountain stations. We have found these differences dependent on station height. Effect caused surely by relatively poor model topography. Correlation of ZTD differences for respective station and height differences (EPN station height minus interpolated in COSMO model grid for station coordinates) is amazing. See below.

4 Comparison of precipitable water and ZTD

Numerical weather prediction model grid can be treated as meteorological data database. We get IPW (or IWV) simply by numerical integration of vertical profiles of water vapour density (calculated from half-level temperature and specific humidity):

$$IWV = \int \rho_{wv}^k dh \approx \sum_{k=1}^{N} (h_{j+1} - h_j)$$

Now we can compare IPW from COSMO model and GPS solutions.

Now we can compare IPW from COSMO model and GPS solutions.

Next we present selected results and visualizations of thorough comparisons of IPW. GPS (or $GNSS = GPS + Glonass$) IPW comes from from EPN and IGS solutions. COSMO IPW is integrated from input fields and first forecast steps in NWP models COSMO_14 and COSMO_2.8 in 2011 and 2012.

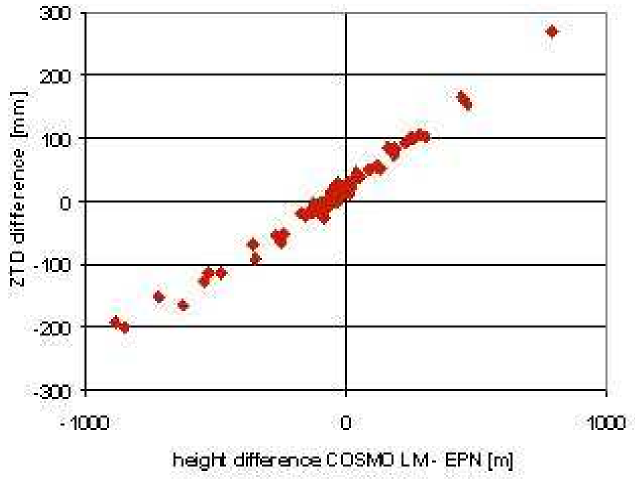

Figure 3: ZTD differences [mm] for EPN stations inside COSMO model in relation to height difference: EPN height (logs) - height of model ground level for station coordinates

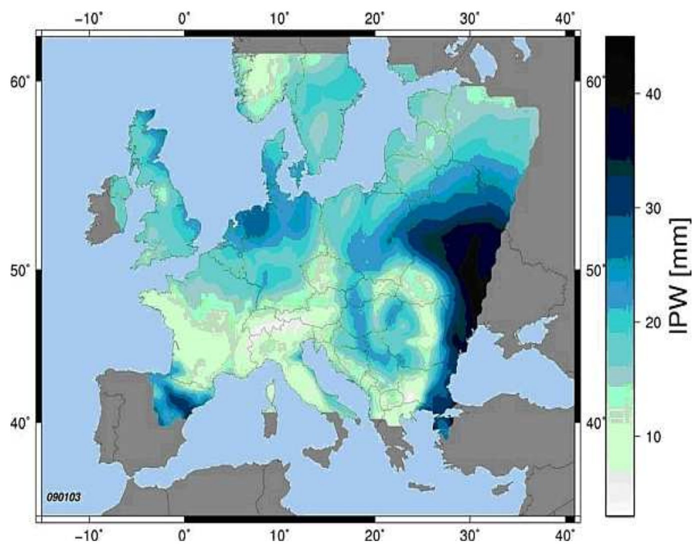

Figure 4: Maps of IPW [mm] calculated from COSMO_14 forecast: 2011 September 1^{st}, $03:00$ UTC

We analyse time dependence of IPW differences, spatial (geographical) distribution of IPW biases and standard deviations, also IPW biases height dependence (9).

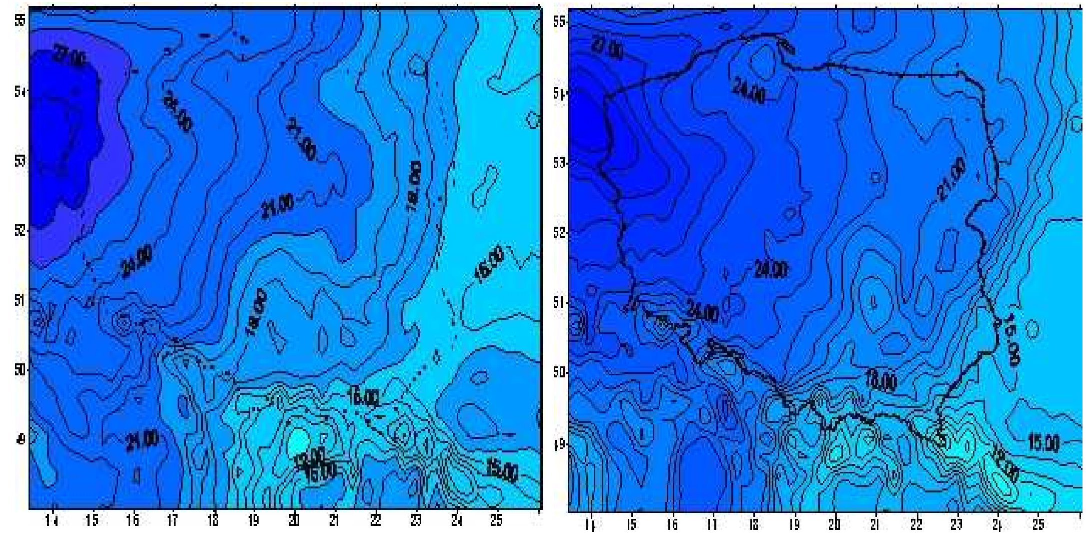

Figure 5: Maps of IPW [mm] calculated from COSMO_2.8 input fields: 2011 August 11 T = 00 UTC (analysis) and $T = 03$ UTC (first forecast step)

	GNSS	NWP model	GPS - NWP bias [mm]	mean absolute bias [mm]	difference std dev [mm]	difference RMS [mm]	stations
2011	EUR comb - station meteo	COSMO-LM_14	-0.85	2.25	2.21	2.88	38
	EUR comb - station meteo	COSMO-LM_14 ver II	-1.19	2.03	2.18	2.66	38
	EUR comb - model meteo	COSMO-LM_14	-0.87	2.07	2.34	2.74	163
	EUR comb - model meteo	COSMO-LM_14 ver II	-0.89	2.05	2.32	2.73	163
	EUR comb - station meteo	COSMO-LM_2.8	-1.06	1.87	2.06	2.44	19
	EUR comb - model meteo	COSMO-LM_2.8	-0.78	1.68	2.09	2.28	31
2012	EUR comb - model meteo	COSMO-LM_14	-0.68	1.94	2.29	2.63	159
	EUR comb - station meteo	COSMO-LM_14	-0.71	1.72	2.13	2.39	30
	EUR comb - station meteo	COSMO-LM_14 ver II	-0.74	1.73	2.13	2.41	30
	EUR comb - model meteo	COSMO-LM_14 ver II	-0.73	2.04	2.40	2.76	159
	EUR comb - station meteo	COSMO-LM_2.8	-0.46	1.50	1.99	2.12	18
	EUR comb - model meteo	COSMO-LM_2.8	-0.80	1.60	2.04	2.22	31
	IGS final - station meteo	COSMO-LM_14	-0.80	1.69	2.07	2.33	14
	IGS final - model meteo	COSMO-LM_14	-1.06	1.78	2.23	2.52	18

Table 2: Comparison of IPW standard ZTD solutions (EPN and IGS tropospheric product) and radiosoundings nearby GPS stations in 2011 and 2012. All results are given in values of IPW. Indicated source of meteo data for IPW separation and method of vertical integration (version II tests profile reconstruction using half-levels as layer boundaries - so we get double levels number).

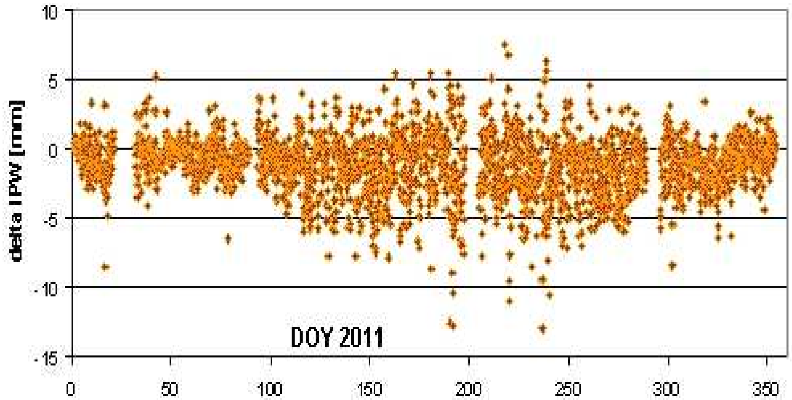

Figure 6: IPW difference: GNSS EUR for JOZE - COSMO_14 model in 2011

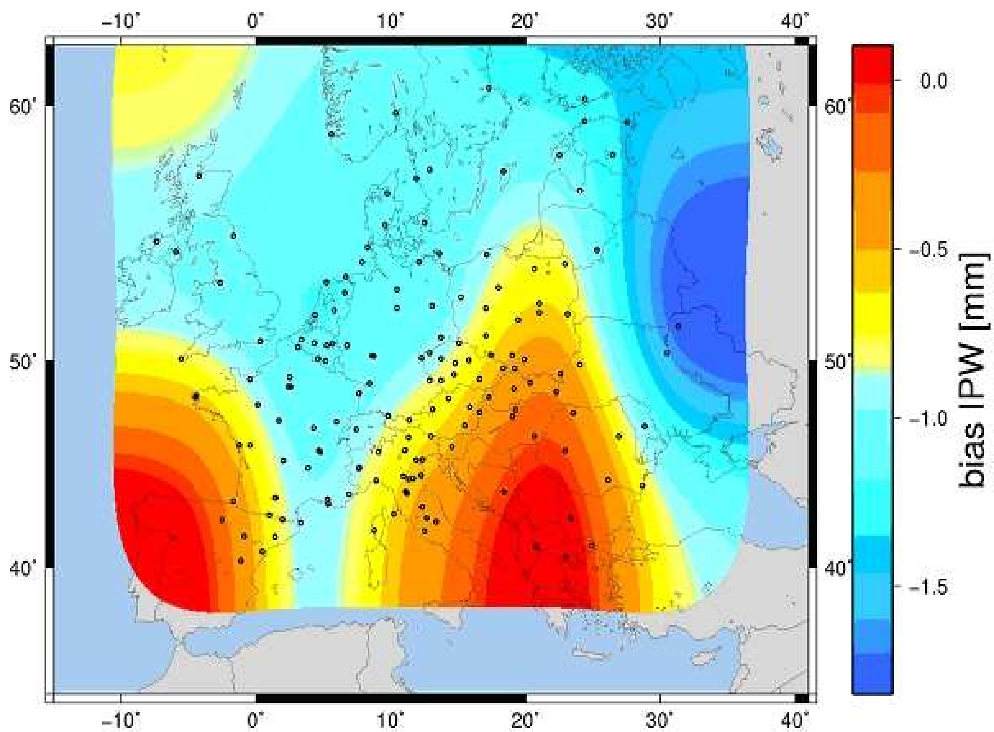

Figure 7: IPW difference (GNSS EUR tropospheric combination - COSMO_14; annual average) map for 2011, meteo from COSMO model; map area is wider than model area due to technical reasons.

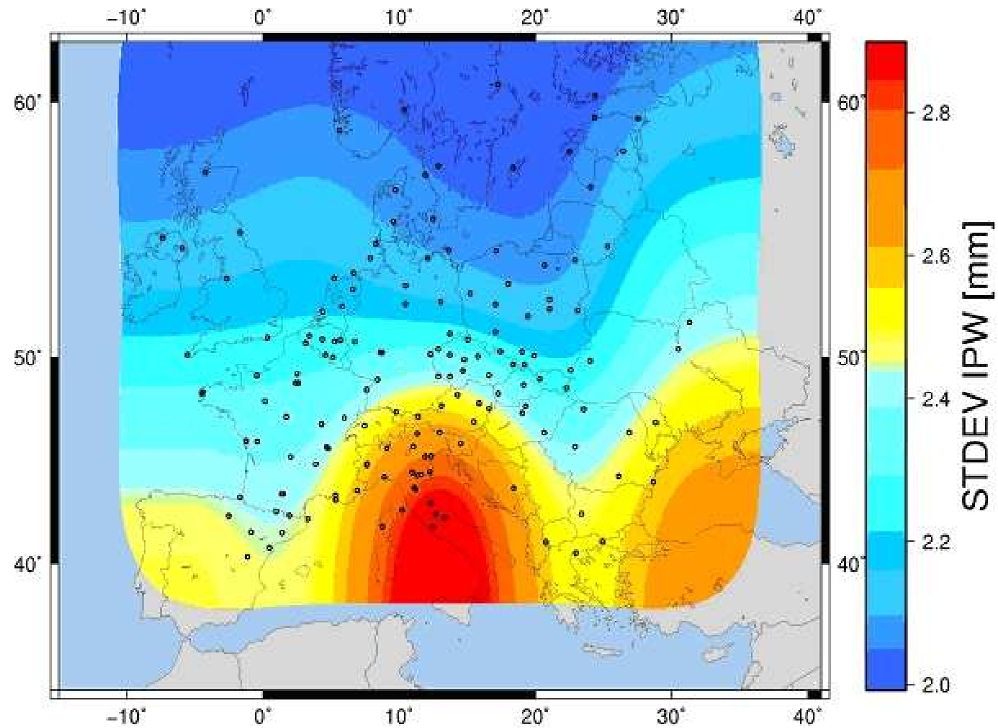

Figure 8: IPW difference standard deviation (GNSS EUR tropospheric combination - COSMO_14; annual average) map for 2011, meteo from COSMO model, version I

Separating analysis fields and forecast steps for comparison of IPW (GPS EUR vs. COSMO) we get to the conclusion that early forecast steps can be used as meteo database together with input fields (analysis).

forecast step	mean difference [mm]	mean absolute difference	difference STDEV
T=0	-0.76	2.04	2.33
T+3h	-0.79	2.07	2.36
T+6h	-0.93	2.08	2.33
T+9h	-0.98	2.10	2.32

Table 3: Comparison of IPW (GPS EUR vs. COSMO_14 in 2011) from input fields and first three forecast steps; T means here time.

Next interesting analysis is to relate IPW differences (comparison of GPS EUR vs. COSMO) to the station height. Linear regression would indicate some problems with pressure reference.

Let us look at 'model meteo' that is meteo data interpolated from COSMO model grid needed to calculate IPW from ZTD for each station inside model grid:

Surface atmospheric pressure from local meteo device at GNSS stations and values interpolated from COSMO model typically shows bias of 1 hPa, difference std. deviation 1 hPa. Surface temperature typical bias is 1 C degree, std. deviation 2 C degrees but sometimes greater. GPS stations meteorological devices are not always properly located: often on the building roof next to GPS antenna (This is also true for JOZE).

To the IPW analysis we add also several results of COSMO tropospheric delay (ZTD) fields comparisons with GPS estimates. This research is ongoing so we present only rough sketch

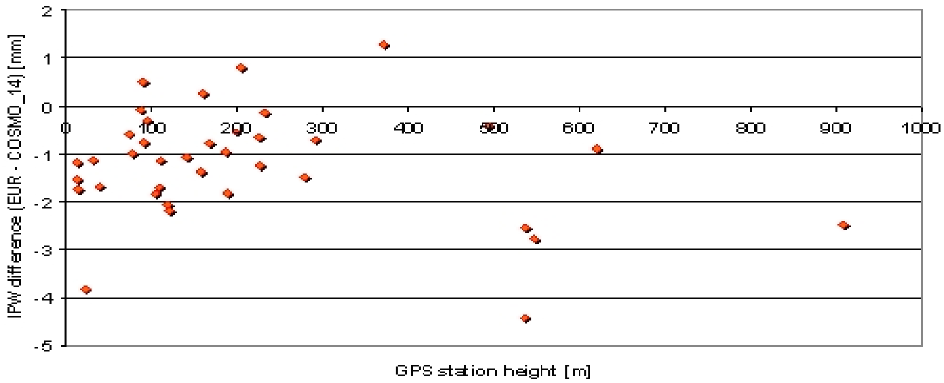

Figure 9: IPW difference (EPN tropospheric combined product COSMO_14, version II) height dependence in 2011

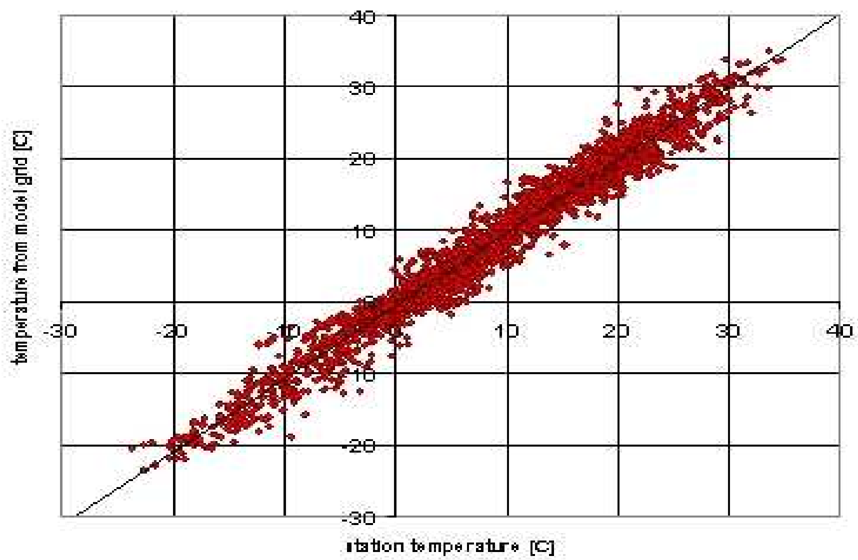

Figure 10: Temperature at JOZE GPS station (Józefosław south of Warsaw) vs. COSMO_14 model in 2012

of results.

station	GPS - COSMO bias [mm]	mean absolute bias [mm]	difference std dev [mm]	difference RMS [mm]	no of points	station ASL height [m]
BOGI	-1.91	2.32	2.09	2.83	214	109.1
BOGO	-2.1	2.34	1.89	2.83	523	118.8
BOR1	1.05	1.59	1.71	2	408	89
BPDL	-0.56	1.53	1.97	2.05	1116	167.5
BYDG	-0.59	1.66	2.14	2.22	854	73.8
DRES	-0.63	1.71	2.27	2.36	1135	159.3
GOPE	-2.06	2.4	2.41	3.17	1075	547.4
GWWL	-0.75	1.6	2.07	2.2	1126	90.8
JOZ2	-2.07	2.3	1.96	2.85	1136	120.9
JOZE	-1.06	1.68	1.96	2.22	1136	109.9
KATO	-0.45	1.5	2	2.05	1118	291.6
KUNZ	-2.33	2.66	2.22	3.21	1053	656.1
LAMA	-0.96	1.59	1.95	2.17	1108	157.7
REDZ	-0.67	1.52	1.93	2.05	1110	76.8
SWKI	-1.61	1.98	1.95	2.53	1120	188.5
TUBO	-2.31	2.59	2.4	3.34	997	279.6
USDL	0.18	1.48	2.04	2.04	1118	494.1
WROC	-0.91	1.68	2.14	2.32	1041	140.5
ZYWI	-0.37	1.46	1.97	2	1120	370.7

Table 4: Comparisons of IPW from EUREF tropospheric product (combination) and input fields and first forecast steps in COSMO_2.8 model in 2011 {for the GNSS stations minutes check: www.epncb.oma.be}

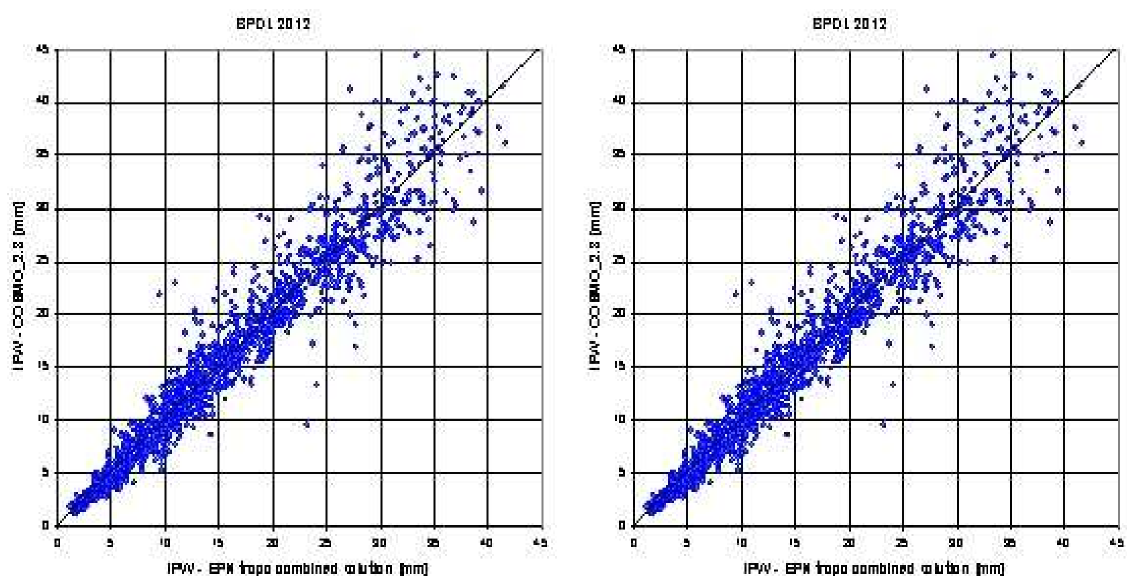

Figure 11: IPW comparisons GNSS EUR combined tropospheric solution for 2 GNSS stations in Poland vs. COSMO_2.8 model (version I) in 2012 BPDL (Bielsk Podlaski) and LAMA (Lamkówko, near Olsztyn); correlations are respectively: 0.966 and 0.973 but difference standard deviation in each case around 2 mm

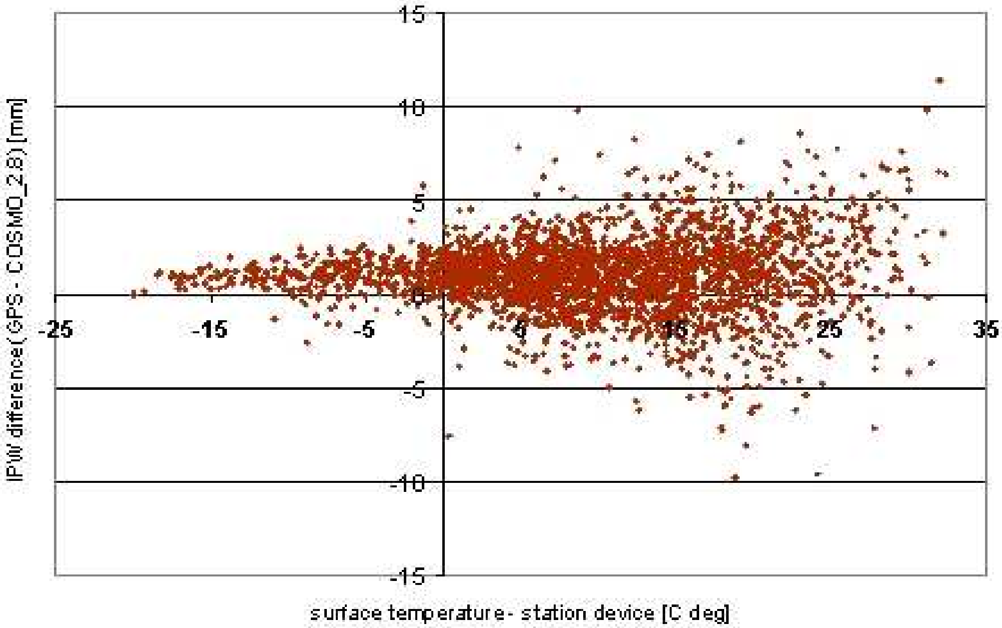

Figure 12: IPW difference (EPN tropospheric combined product - COSMO_2.8) temperature dependence in 2012

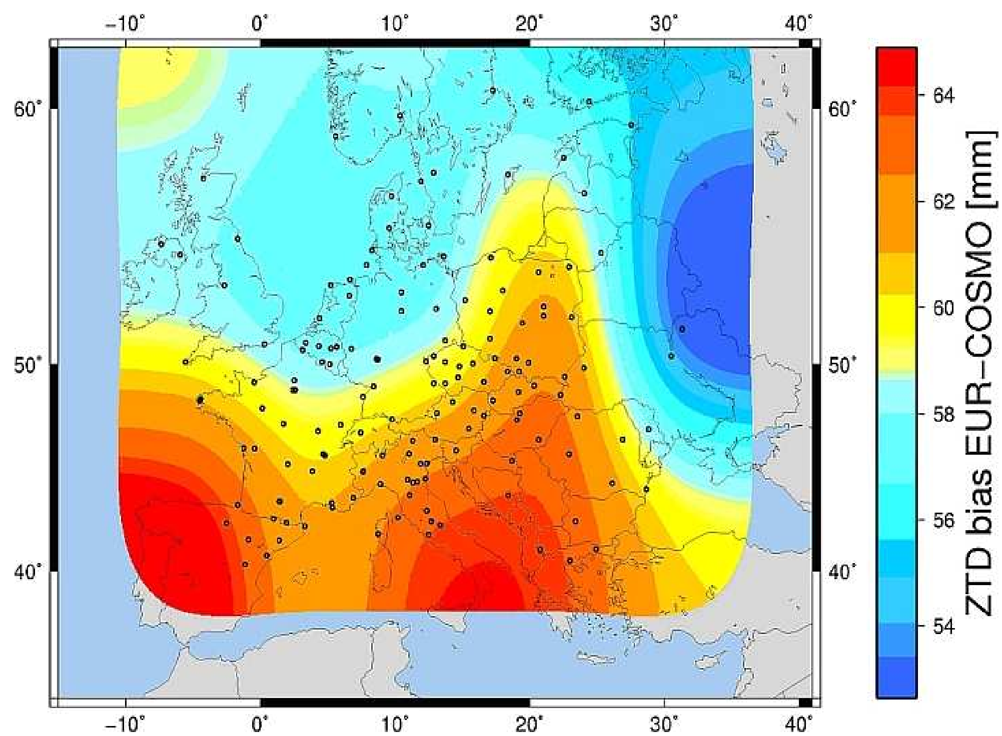

Figure 13: ZTD difference (GNSS EUR tropospheric combination - COSMO_14; annual average) map for 2012, ZTD integrated in the vertical profile

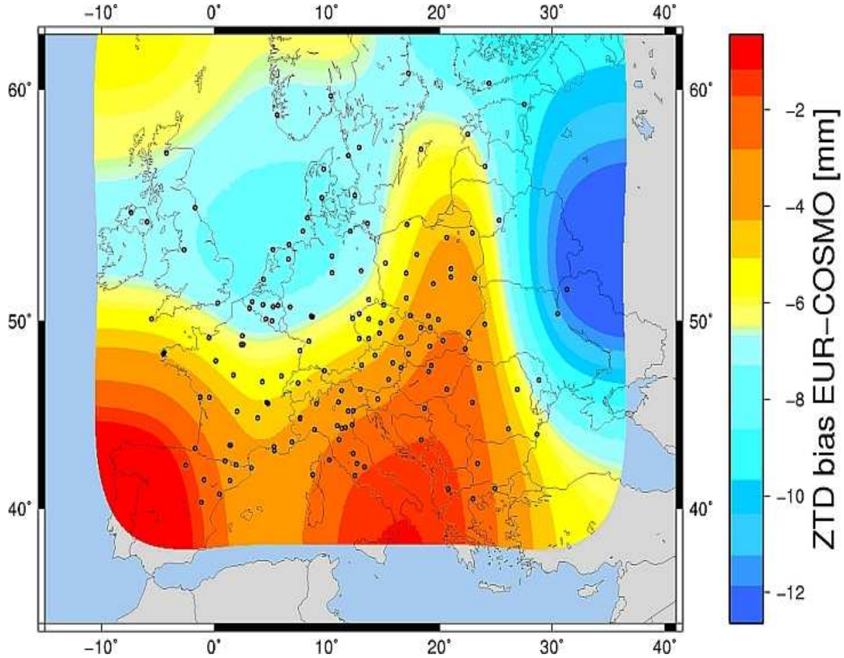

Figure 14: ZTD difference (GNSS EUR tropospheric combination - COSMO_14; annual average) map for 2012, ZTD calculated by hydrostatical method

Pattern of IPW difference distribution is clearly visible in hydrostatic ZTD difference. In the south we got greater IPW values in COSMO fields and so also greater wet delay ZWD and overall delay ZTD. Integration of refractivity by Thayer formula confusingly produces greater values of ZTD in the north. Relative discrepancies produced by direct integration is about 2.5% of ZTD in 14 km resolution model but below 1% (nearly 4 times smaller) for 2.8 km model!

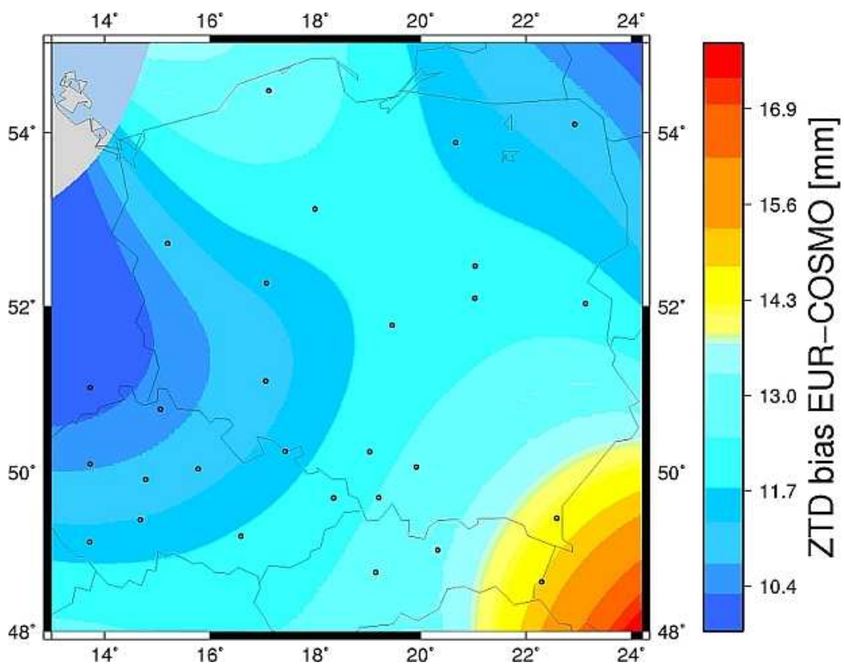

Figure 15: ZTD difference (GNSS EUR tropospheric combination - COSMO_2.8; annual average) map for 2012, ZTD integrated in the vertical profile, GPS stations indicated as small circles

ZTD bias can be result of poor quality of geodetic refractivity models (many of them were developed mostly for classic terrestial measurements), hybrid vertical coordinate in COSMO model or some numerical problems (e.g. numerical integration).

This effect should be further investigated.

5 Conclusions and Outlook

1. IGS and EPN zenith tropospheric delay (ZTD) recalculated to precipitable water (IPW) show good conformity in relation to COSMO model data. COSMO reveal positive IPW bias of about 1 mm (model is 'too wet').

2. Many factors affect both procedure of IPW derivation from COSMO model and calculation of IPW from tropospheric delay: most crucial is height adjustment, but even minor ones like water vapour density formula or barometric equation can affect IPWV on 1 mm level.

3. Using NWP models with dense grid does only slightly evidently improve IPW data, but greatly influences tropospheric delay (this effect will be investigated in next paper)

4. IPW coming from GPS (global and regional static solutions) is of good quality compared with independent meteorological water vapour data sources like radiosounding. In this case radiosoundings show positive bias close to 1 mm of IPW

5. There are many inconsistencies and errors and gaps in local meteorological data for GNSS stations (meteo Rinex) files on IGS/EPN servers. NWP models can be used instead for IPW derivation (COSMO is reliable but smoothed source of surface meteo data). For pairs GPS - RAOB correlation diminishes quickly with distance and height difference

6. GNSS networks provide us with vertically integrated humidity information (precipitable water) which can feed COSMO model (nudge water vapour content in right direction) in network much denser then RAOBs

7. Abundance of meteorological data from NWP and in accordance with them tropospheric delay information makes more and more crucial the question of their usefulness in GPS network processing. Tropospheric delay is smaller then delay caused by ionosphere but harder to eliminate so that contributes more to error budget in many positioning applications.

Acknowledgments

- This research was financially supported by the grant No. N N526 074038 of the Polish Ministry of Science and Higher Education

- Marcin Rajner (Warsaw University of Technology) - maps in GMT

- EPN products developers (esp. Wolfgang Söhne)

- University of Wyoming - radiosounding data

References

[1] Bevis, M., Businger, S., Herring T., Rocken, C., Anthes, R., and Ware, R., 1992: GPS Meteorology: Remote Sensing of Atmospheric Water Vapour using the Global Positioning System, J. Geophys. Res., 97, 15,787-15,801

[2] Sung H. Byun, Yoaz E. Bar-Sever, 2009: A new type of troposphere zenith path delay product of the international GNSS service. J Geod (2009) 83:367-373

[3] Hoffmann-Wellenhof, B., H. Lichtenegger, J. Collins, 1997: GPS Theory and Practice, Fourth, revised edition, Springer-Verlag Wien - New York

[4] Hopfield, H.S., 1971: Tropospheric effect on electromagnetically measured range: Prediction from surface weather data. Radio Science, 1971. 6(3): p. 357-367

[5] McClusky S., T. A. Herring, and R. W. King, 1996: GPS Meteorology: Direct Estimation of the Absolute Value of Precipitable Water, J. of Applied Met., 35, 830-838, June 1996

[6] Rocken, C., R. Ware, T. Van Hove, F. Solheim, C. Alber, J. Johnson, M. Bevis, and S. Businger, 1993: Sensing atmospheric water vapor with the Global Positioning System, Geophys. Res. Lett., 20, 2631

[7] Saastamoinen, J., 1973: Contribution to the theory of atmospheric refraction, Bulletin Géodésique, 107, pp. 13-34.

[8] Smith E.K., S. Weintraub, 1953: The Constant in the Equation for Atmospheric Refractive Index at Radio Frequencies, Proceedings of the I.R.E., 41 pp. 1035-1037, August 1953

[9] Thayer G., 1974: An improved equation for the radio refractive index of air, Radio Science, Vol. 9, No. 10, pp 803-807

COSMO model validation using the Italian radar mosaic and the rain gauges estimated precipitation

N. Vela[1,2], R. Cremonini[1], E. Oberto[1], M. Giorcelli[1,3]

[1] *ARPA Piemonte, via Pio VII 9, 10135, Torino, Italy*

[2] *University of Torino, via Giuria 1, Torino, Italy*

[3] *Arianet S.r.l, via Gilino 9, 20218 Milano, Italy*

1 Introduction

The aim of the present work is to realise a new type of verification for the COSMO-I7 model. The verification is made against a precipitation field estimated by the Italian radar mosaic corrected with the data coming from the Italian rain gauges network. In order to perform the modification an ordinary kriging process of the differences between the radar data and the rain gauges measurement is needed. Once the modified precipitation field is obtained, firstly the relative error is calculated, then a fuzzy multi-scale verification is performed. The whole work is based upon a case study from the 24th to the 27th of October 2010. A second but not less important purpose of the work is to apply this method (already established in literature) to our territory, in order to analyse and elaborate data witch might be applicable to any future model verification. After completing this study, a second phase of the work will begin using the COSMO-I2 model.

2 Observed data: the rain gauges and the Italian radar mosaic

The rain gauges are unevenly distributed through the Italian territory with the exception of the Puglia and Sicily regions. The data delivered within the COSMO Project are used together with those observed by the rain gauges belonging to the different Regional Centres and made available through the Italian Civil Protection Department. The radar data come from 24 operative machines: 10 are installed and managed by Regions, 4 are owned by the Air Force, 2 are owned by ENAV (Air Traffic Control Agency) and 8 are installed by Civil Protection Departement (6 emitting in C band, 2 in X band). In Figure 1 the distribution of the rain gauges and the radar mosaic is shown.

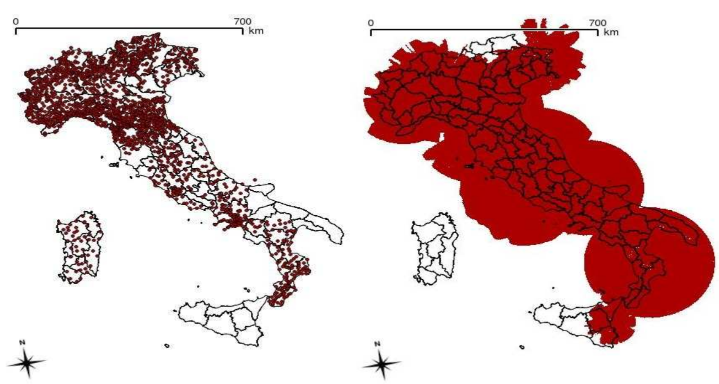

Figure 1: The Italian rain gauge network (left) and the Italian radar mosaic area (right).

3 Reconstruction of the precipitation field

3.1 Calculation of the difference (between radar and rain gauges)

The correspondence between the estimated 24 hour cumulative precipitation (radar) and the rain gauges measurements is calculated. The area associated to each rain gauge includes 9 radar grid points (witch has a 1040.9 m resolution). The median value among the 9 radar grid points is coupled with the rain gauge one. The difference (or deviation) between the two data is calculated as follows:

$$Difference = 10 * \log_{10}\left(\frac{r}{rg}\right) \tag{1}$$

where r is the precipitation estimated by the radar and rg is the rain gauge measurement.

3.2 Ordinary kriging

The ordinary kriging technique has been used to modify the estimated precipitation field recorded by the radars through the rain gauges network data. The "autoKrige" function of the R software has been used for this purpose. This function produces many outputs among witch two have been used: the kriging prediction and the kriging standard error.

4 Validation

4.1 Relative error

The relative error is calculated as follows:

$$Erel = \left[\frac{(F - O)}{O}\right] * 100 \tag{2}$$

where $Erel$ is the relative error, F is the forecast precipitation amount and O is the observed one (coming from the correction of the radar estimation). The relative error is calculated for the 24 hours cumulative precipitation (mm/24h). Concerning the model, the first day of forecast is used (00UTC run). The relative error is evaluated for the areas where the kriging standard error does not exceed the value of 4 dB.

4.2 Fuzzy verification

This kind of verification answers the question: "*Witch is the link between spatial forecast and a combination of the intensity of the precipitation and the scale of the event ?*" The scale decomposition methods allow us to diagnose the model errors and performances according to different scales. The scale-intensity approach links the traditional bi-dimensional verification categories: it returns the model skills according to different precipitation intensities and spatial scales. It verifies the model over the whole domain. It is useful in the spatial verification of discontinuous fields (like the precipitation). It supplies information both for single case studies and forecast systems evaluated over a longer time. Using a neighborhood verification method an exact correspondence between forecast and observation is not needed.

Re-sampling of the domain The domain is divided in boxes with a side of 10 km: each box contains the mean value of the precipitation records found in it (or a value which marks it as non valid if less than 75% of the included values are valid). Two different files are then created: one for the forecast data (COSMO-I7), the other one for the observations (radar corrected with the rain gauges).

Fraction Skill Score Answers the question: *What are the spatial scales at which the forecast resembles the observations ?* The Fraction Skill Score (FSS) directly links the portions of the grid which are covered by the forecast and by the observation (for example the rain exceeding a certain threshold) through spatial windows of increasing size. The FSS is calculated as follows:

$$FSS = 1 - \frac{\frac{1}{N}\sum_N (P_f - P_o)^2}{\frac{1}{N}\left[\sum_N P_f^2 + \sum_N P_o^2\right]} \tag{3}$$

where P_f is the portion of the box covered by the forecast, P_o is the portion of the box covered by the observation and N is the number of spatial boxes covering the entire domain. The Fractions Skill Score ranges from 0 (complete mismatch) to 1 (perfect match).

The value of FSS above which the forecasts are considered to have useful (better than random) skill is given by $FSS_{useful} = 0.5 + f_o/2$, where f_o is the domain average observed fraction. The smallest window size for which $FSS \geq FSS_{useful}$ can be considered the "skillful scale". As the size of the squares used to compute the fractions gets larger, the score will asymptote to a value that depends on the ratio between the forecast and observed frequencies of the event. The closer the asymptotic value to 1, the smaller the forecast bias. The score is most sensitive for rare events (small rain areas for example).

Equitable threat score (Gilbert skill score) Answers the question: *"How well did the forecast "yes" events correspond to the observed "yes" events (accounting for hits due to chance) ?"* It measures the fraction of observed and/or forecast events that were correctly predicted, adjusted for hits associated with random chance (for example, it is easier to correctly forecast rain occurrence in a wet climate than in a dry climate). The ETS is often used in the verification of rainfall in NWP models because its "equitability" allows scores to be compared more fairly across different regimes. It is sensitive to hits. Since it penalises both misses and false alarms in the same way, it does not distinguish the source of forecast error. It is calculated as:

$$ETS = \frac{hits - hits_{random}}{hits + misses + falsealarms - hits_{random}} \tag{4}$$

where

$$hits_{random} = \frac{(hits + misses)\,(hits + falsealarms)}{total} \tag{5}$$

5 Case study: 2010/10/24-25-26-27

This case study has been chosen because of the preponderance of advective precipitation over the whole event, against a short convective phase at the beginning. The precipitation is well spread over the entire Italian territory on the 25^{th} and 26^{th} of October, while it is more concentrated over northern Italy on the 24^{th} and over the south on the 27^{th} of October.

5.1 Preliminary operations

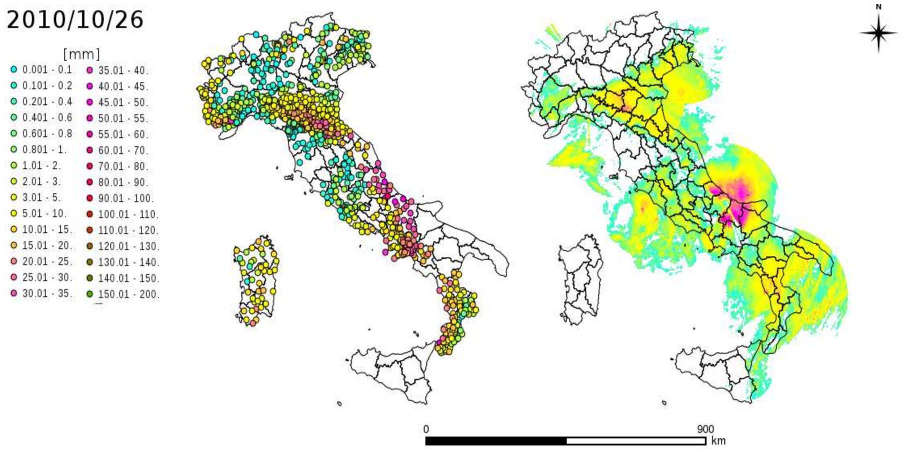

Figure 2: Rain gauges measurement (left) and pluviometric data from the Italian radar mosaic (right). (mm/24h, 26th of October)

In Figure 2 the rain gauge observations and the rain estimated by the radar are shown for the 26^{th} of October (mm/24h). It is possible to notice that the the agreement between the two data is very good for what concerns the spatial dislocation, a little less good if we look at the intensity of the precipitation. The main differences are located over the Alps and the Apennines, and where the rain is very weak or very intense. The overall mean difference between the rain gauge measurements and the radar data falls between -5 and -2.5 dB: the radar seems to underestimate the precipitation. Figure 3 shows the spatial distribution of the difference between the two data expressed in dB (in red are shown the points where the radar underestimates, in blue those where it overestimates).

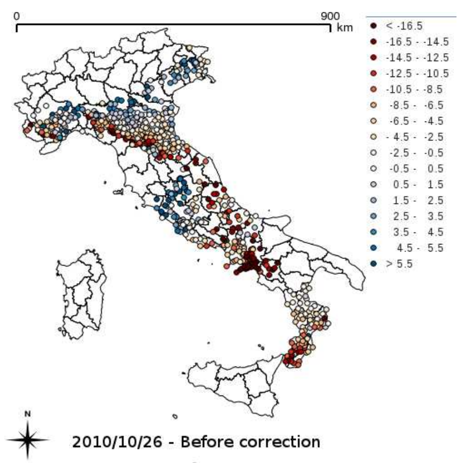

Figure 3: Difference (dB) between the pluviometric radar data and rain gauge measurements (spatial distribution). Blue: the radar data is higher than the associated rain gauge measurement. Red: the radar data is lower than the associated rain gauge measurement. In this figure it is possible to notice that the rain gauge measurements are higher than the pluviometric radar data over the more elevated points. (26th of October)

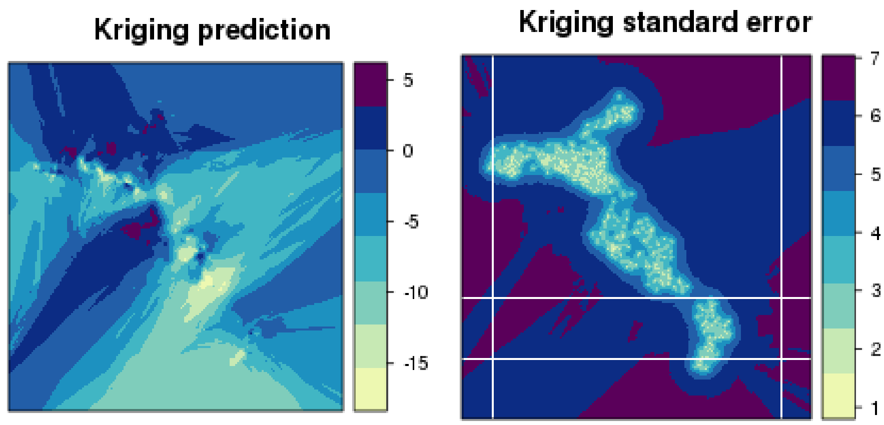

Figure 4: Two outputs among those coming from the autoKrige functionality in R. Left: kriging prediction for the difference between radar and the rain gauges network. Right: the associated kriging standard error. All the data are expressed in dB. (26th of October)

5.2 Ordinary kriging

The difference (expressed in dB) between the pluviometric radar data and the rain gauge measurements is then used to correct the radar itself. The ordinary kriging is used for this operation. In Figure 4 it is possible to see the output given by the autoKrige function of the R software (the kriging prediction on the left, the kriging standard error on the right, this is the result for the 26^{th} of October). It is possible to notice that the standard error is small where the rain gauge network is thicker, while it gets bigger where there are fewer of them (beyond Italy borders, over the sea, in Puglia and Sicily regions). The ordinary kriging procedure increases the precipitation recorded by the radar over most of the grid points (Figure 5).

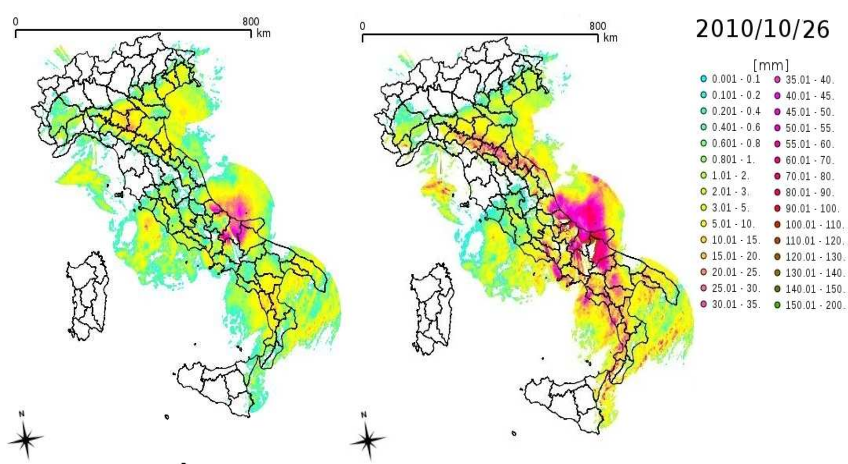

Figure 5: Pluviometric radar field (left) and pluviometric radar field after the rain gauge correction (right). Data expressed in mm. (26^{th} of October)

6 Verification

6.1 Preliminary analysis

The first step in the verification is an eyeball comparison (Figure 6, given as an example) between the modified radar field and the COSMO-I7 forecast. It is possible to notice a good agreement between the two fields. The agreement is good for what concerns the dislocation of the precipitation patterns, a little worst if we look at the intensity of the precipitation.

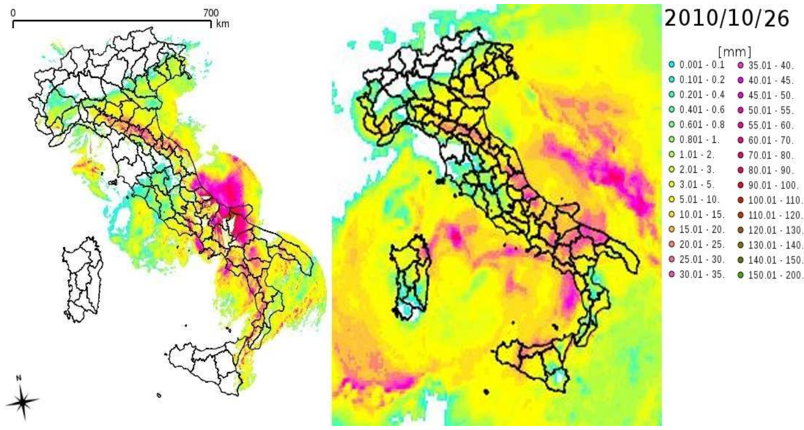

Figure 6: Pluviometric radar field corrected with the rain gauge measurements (left) and COSMO-I7 forecast cumulated (24h) precipitation (right). (26^{th} of October)

6.2 Relative error calculation

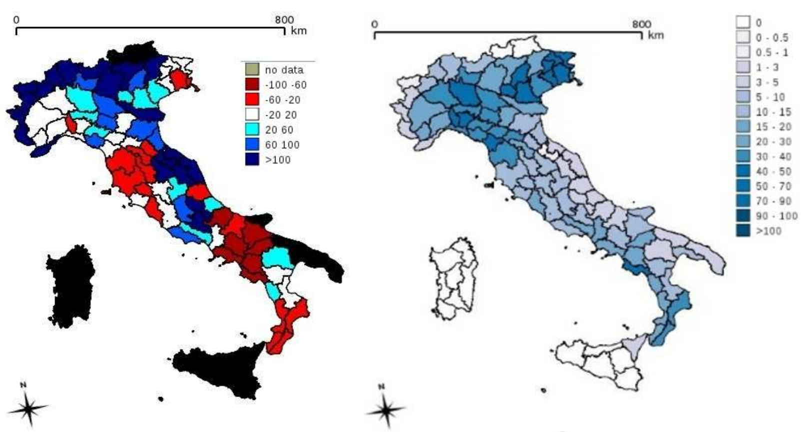

Figure 7: Relative error (left) and cumulative precipitation (mean over alert areas) (right). (25^{th} of October)

In Figure 7 the calculation of the relative error between the forecast and the observed precipitation for the 25^{th} of October is reported. The relative error is calculated for each of the 102 alert areas in which the Italian territory is subdivided. The ones coloured in black are those where the kriging standard error exceeds the value of 4 dB (no rain gauges or no rain). The red ones are those where the forecast underestimates the precipitation, the blue ones are those where COSMO-I7 overestimates it. It is possible to notice a general overestimation of the model over northern Italy, more marked in the alpine region. For what concerns the peninsula, the model underestimates almost everywhere, with the exception of the Marche and part of the Lazio regions where there is overestimation.

6.3 FSS calculation

As written before, the two fields (forecast and observed) must be brought to a common grid to calculate the FSS. This common grid is made of boxes with a side of 10 km. From these two new grids the files for each exceeding threshold are written (0.2, 1, 2, 5, 10, 20, 40, 50, 75 mm) (Figure 8, example: 25^{th} of October, 20 mm). The portions coloured in blue are those where the precipitation exceeds the threshold, the red ones are those where the threshold is not reached, while the white ones are those where the precipitation data are not valid. The

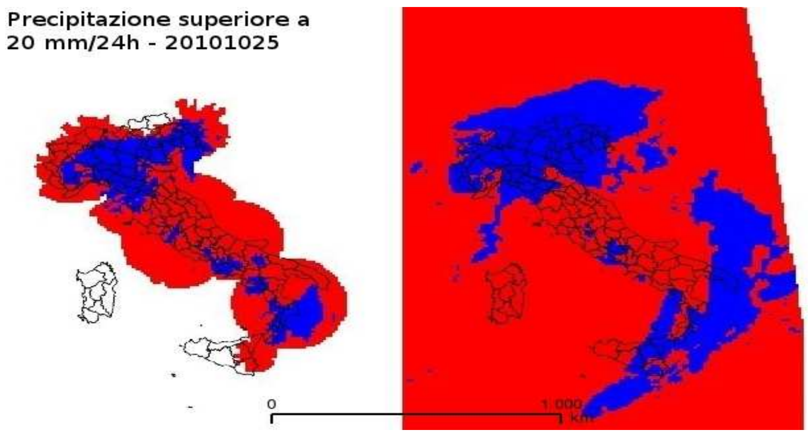

Figure 8: Observed (corrected radar field) (left) and forecast (right) precipitation exceeding the 20mm/24h threshold for the 25^{th} of October. White: no data. Red: precipitation not exceeding the threshold. Blue: precipitation exceeding the threshold.

FSS results for the four days are presented in Figure 9. The black line surrounds the values witch are higher than the FSS_{useful} (different for each threshold). Higher values of FSS can be found for large areas and very low thresholds (upper left corner in each panel). The best FSS values are those of the 25^{th} of October, where the precipitation is more extensive. It is in such a case that it is important to look at the FSS_{useful}: the value of FSS above which the forecasts are considered to have useful skill (better than random).

6.4 ETS calculation

Figure 10 shows the results for the ETS calculation over the four days of the event. Also in this case there is a better forecast for wide areas (with the exception of the 26^{th} of October for the medium-high thresholds). The graphs of the ETS are not monotone: the function contains a factor witch takes into account the frequency of the forecast event (i.e. precipitation exceeding higher thresholds are less common and for this reason more difficult to forecast). A relative maximum in the results of the ETS means a better performance of the model for those thresholds. As the FSS, the ETS shows a very good performance of the model for wider areas at low thresholds. ETS shows a good performance also for the mean thresholds.

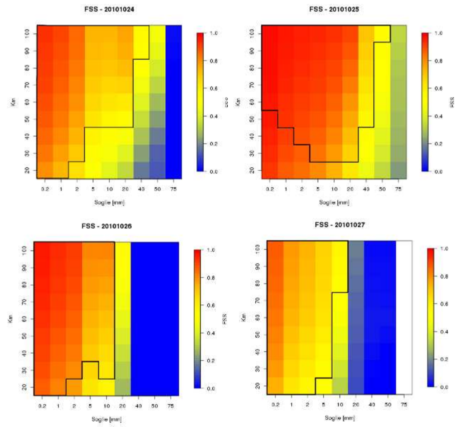

Figure 9: The graphs show the value of the FSS and the FSS_{useful} (black line) for each of the four days of the event. X-axis: thresholds (mm/24h). Y-axis: box side (km).

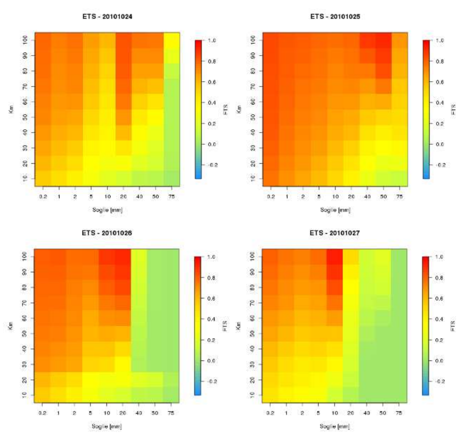

Figure 10: The graphs show the value of the ETS for each of the four days of the event. X-axis: thresholds (mm/24h). Y-axis: box side (km).

7 Conclusions

7.1 Ordinary kriging

It is not possible to integrate the radar field with the data coming from the rain gauges by simply applying a bias to the first one. On the one hand the rain estimated by the radar is affected by errors coming from the characteristics of the precipitation, the orography and the geometry of the beam itself. On the other hand, the rain gauges show some problems when displaced at higher altitude and do not supply a regular field. For the above reasons we decided to use the R functionality "autoKrige" to perform an ordinary kriging of the differences between the radar precipitation field and the rain gauge network measurements, and then to use the latter to correct the first.

7.2 Relative error

The field resulting from the correction of the pluviometric radar data has then been used as an observation to calculate the relative error of the COSMO-I7 precipitation forecast (cumulative over the 24 hours, first day forecast, 00UTC run). The evaluation of the relative error has been done by dividing the Italian territory into the 102 alert areas used by the Civil Protection Department. The mean forecast and observed precipitation has been calculated for each area (with the exception of those where the kriging standard error was too high). The results are concordant with those coming from a more classic verification (rain gauges only): COSMO-I7 tends to overestimate the precipitation over the Alpine area and underestimates (or overestimates less) over the plains.

7.3 Fuzzy verification

Fuzzy verification methods are called scientific and diagnostic and they analyse the nature of the error itself. Both the FSS and the ETS show how the COSMO-I7 model has always very good skills in forecasting the precipitation for low thresholds over wide areas. The ETS also show good skills for the middle thresholds (also on large areas). The quality of the forecast reduces if we look at higher thresholds: this might be because they are more spatially localized. This kind of verification lets us know what are the conditions in witch COSMO-I7 can be trusted for different types of forecasts (from the local to the large scale ones).

7.4 Future developments

This work, although it refers to a single case study, shows some potentiality and some promising result. The idea is to extend the approach to other cases using the model COSMO-I2 which probably is more suitable for this kind of analysis due to its higher horizontal resolution.

References

[1] Cherubini, T., Ghelli, A. and Lalaurette, F., 2002: Verification of precipitation forecasts over the Alpine region using a high-density observing network, *Wea. Forecasting*, 17, **238-249**.

[2] Ciach, G. J., W. F. Krajewski, E. N. Anagnostou, M. L. Baeck, J. A. Smith, J. R. McCollum, A. Kruger, 1997: Radar Rainfall Estimation for Ground Validation Studies of the Tropical Rainfall Measuring Mission., *J. Appl. Meteor.*, 36, **735747**.

[3] Cremonini R., R. Bechini, V. Campana, D. Rabuffetti, and I. Giudici, 2004: An implementation of Kalman filter in north-western Italy for radar calibration using 3-hourly gauges measurements and polarimetric c-band radar estimates, *Proceedings of ERAD* (2004): **352355**.

[4] Ebert, E.E. and J.L. McBride, 2000: Verification of precipitation in weather systems: Determination of systematic errors, *J. Hydrology*, 239, **179-202**.

[5] Giuli D., E. Palmisano, G. Scarchilli, J. Tan, M. Thurai, 1996: Rain assessment through integration of radar and rain-gauge data in severe storms, *Remote Sensing Reviews*, Vol. 14, Iss. 1-3.

[6] E. Goudenhoofdt, L. Delobbe, 2009: Evaluation of radar-gauge merging methods for quantitative precipitation estimates, *Hydrol. Earth Syst. Sci.*, 13, **195-203**.

[7] Holleman, I., 2006: Bias adjustment of radar-based 3-hour precipitation accumulations KNMI publication, TR-290, 11/10/2006, pp**56**.

[8] Kaufmann, P., 2007: Post-processing of the aLMo Precipitation with the Neighborhood Method, *COSMO Newsletter* No. 7.

[9] Krajewski, W. F., 1987: Co-kriging radar-rainfall and rain gage data, *J. Geophys. Res.*, 92(D8), **95719580**.

[10] Jolliffe, I.T., and Stephenson, D.B., 2003: Forecast Verification: A Practitioner's Guide in atmospheric Science, *John Wiley and Sons*.

[11] Joss, J., R. Lee, 1995: The application of Radar-Gauge comparisons to operational precipitation profile corrections. *J. Appl. Meteorol.* 34, **2612-2630**.

[12] Oberto E., Milelli M. 2010: QPF verification for 2008/2009 of several COSMO-Model version, *COSMO NEWSLETTER* No.10.

[13] Pappenberger, F., Ghelli, A., Buizza, R., and Bodis, K., 2009: The skill of probabilistic forecasts under observational uncertainties within the generalized likehood uncertainty estimation framework for hydrological applications, *J. Hydrometerol.*, 10, **807819**.

[14] Sinclair, S. and Pegram, G. 2005: Combining radar and rain gauge rainfall estimates using conditional merging, *Atmos. Sci. Lett.*, 6, **1922**.

[15] Wilks, D.S., 1995: Statistical Methods in the Atmospheric Sciences. An Introduction, *Academic Press*, San Diego, xvii+**627** pp.

[16] Zawadzki, I., 1984: Factors affecting the precision of radar measurements of rain. In Proceedings of Preprints of the 22nd Conference on Radar Meteorology; *American Meteorological Society*: Boston, MA, USA.

Development of a COSMO–based limited–area ensemble system for the 2014 Winter Olympic Games

Andrea Montani, C. Marsigli and T. Paccagnella

ARPA–SIMC, Bologna, Italy

1 Introduction

Next winter Olympics and Paralympic Games will take place in Sochi, Russia, in a region characterised by complex topography located in the vicinity of the Black Sea. The Olympic Games will take place from 7 to 23 February 2014, while the Paralympic Games from 7 to 16 March 2014. In the framework of these events, WMO is launching two initiatives: a dedicated WWRP FDP (Forecast Demonstration Project) and a dedicated WWRP RDP Research and Development Project) to improve understanding of nowcasting and short-range prediction processes over complex terrain. A new project named **FROST-2014** (**F**orecast and **R**esearch in the **O**lympic **S**ochi **T**estbed; http://frost2014.meteoinfo.ru/) was set-up at the kick-off meeting held in Sochi from 1 to 3 March 2011. Four Working Groups (WGs) were established to deal with the various components of the project, more specifically:

- WG1: observations and nowcasting;
- WG2: NWP, ensembles and assimilation;
- WG3: IT including graphical tools, formats, archiving and telecommunication;
- WG4: products, training, end user assessment and social impacts.

As for WG2, it was agreed that ensembles with resolution about 7 km or coarser could be involved in the project in forecast and demonstration mode (FDP component), while systems with resolution about 2 km would contribute to the project in research mode (RDP component). Within the former component, one of the main activities deals with the set-up, generation, implementation and maintenance of a limited-area ensemble prediction system based on COSMO model and targeted for the Sochi-area.

2 Scientific plan

In the framework of the FDP, it was decided to clone COSMO-LEPS system and relocate it over Russia, centring the domain over the Sochi area, thus generating COSMO-FROST-EPS system. In the past years, COSMO-LEPS (Montani et al., 2011) proved to be a valuable tool for the generation of probabilistic predictions of high-impact weather over complex topography and it is envisaged that COSMO-FROST-EPS can provide useful support to bench forecasters during the Olympic Games. Within FROST-2014, the attention will be focused on those atmospheric variables which play a major role in the outdoor activities of the Olympic Games. More specifically, the probabilistic prediction of wind, wind-gust, precipitation (in various forms), temperature, humidity and visibility will be required for forecast ranges up to three days, depending on the variable.

Phase I: set–up of the system
In this phase, which took place in early 2012, a prototype COSMO-FROST-EPS system was set–up with a configuration similar to COSMO-LEPS application. In order to save computer time, the ensemble size was initially limited to 10 members and the forecast range to 72 hours. Therefore, the main characteristics can be summarised as follows:

- horizontal resolution: 7 km;
- vertical resolution: 40 model levels;
- number of grid points (NX x NY x NZ) = $365 \times 307 \times 40 = 4.482.200$;
- forecast length: 72 hours;
- ensemble size: 10 members,
- initial conditions: interpolated from selected ECMWF EPS members;
- boundary conditions: interpolated from selected ECMWF EPS members;
- initial times of the run: 00UTC and 12UTC.

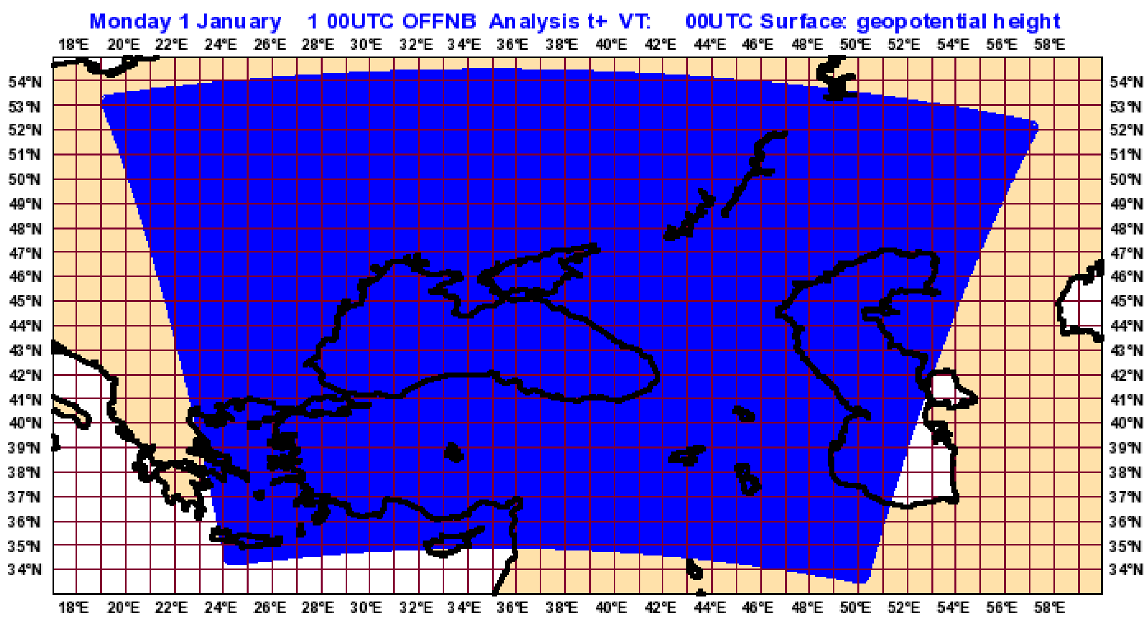

Figure 1: Integration domain for COSMO–FROST–EPS

Fig. 1 shows the integration domain of COSMO-FROST-EPS. The ECMWF EPS members providing initial and boundary conditions to COSMO-FROST-EPS integrations, are selected by means of a clustering analysis / selection of representative members similar to the one used in COSMO-LEPS time-critical application. COSMO-FROST-EPS system produces a set of standard probabilistic products (e.g. probability maps, meteograms, ...) to be delivered in real time to the Met Ops room of the Hydrological and Meteorological Centre of Russia (hereafter, Roshydromet). The generation of the different types of non-graphical products will take advantage of Fieldextra, the official COSMO post-processing software, developed at Meteoswiss (for information about Fieldextra, please refer to http://www.cosmo-model.org).

Phase II: development of the system

This phase is covering late 2012 and early 2013: on the basis of the experience gained in Phase I and on the feedback provided by Roshydromet forecasters, the configuration of COSMO-FROST-EPS will be adapted accordingly; the same applies to the type of products to be generated and delivered. As COSMO-FROST-EPS configuration is thought in a modular way, it could be modified in terms of ensemble size, forecast range and other features with limited effort. In this phase, the complete transition of the system towards the use of GRIB2 format for COSMO-FROST-EPS output files will take place. The set of products to be delivered will have to be consolidated, as well as the procedures of transmission and visualisation.

Phase III: final implementation of the system

This phase will cover the full length of Winter Olympic and Paralympic Games: COSMO-FROST-EPS system should run continuously from November 2013 to March 2014. Generation and transfer of products (forecast fields and/or plots) will have to be reliable and a timely delivery will have to be ensured.

3 Verification results

In this section, we present the first results relative to the performance of COSMO–FROST–EPS. The skill of the mesoscale ensemble is assessed over the period January–March 2012 and compared to that of ECMWF EPS. For both systems, we consider the probabilistic prediction of 12–hour accumulated precipitation exceeding a number of thresholds for several forecast ranges. Table 1 summarises the main properties of COSMO–FROST–EPS and ECMWF EPS, indicating the main differences between the two systems.

Table 1: Main features of the verified systems.

	COSMO–FROST–EPS	ECMWF EPS
EnsembleSize	10 members	51 members
ForecastLength	72h	240h
InitialTime	12 UTC	12 UTC
HorizontalResolution	7 km	25 km
VerticalResolution	40 ML	62 ML

As for observations, it has been decided to use the data obtained from the SYNOP reports available on the Global Telecommunication System (GTS), since this is recognised to be a homogeneous and stable dataset throughout the verification period. In the future, it is planned to verify the performance of COSMO–FROST–EPS over denser observational datasets.

In order to quantify the skill of the system over complex topography, the verification is performed over the domain 40N–50N, 35E–45E. Within this domain, a fixed list of 60 SYNOP stations is considered and the relative reports in terms of total precipitation are used to evaluate the COSMO–FROST–EPS and ECMWF-EPS skill. As for the comparison of model forecasts against SYNOP reports, we select the grid–point closest to the observation. Little sensitivity to the results is found when, instead of the nearest grid–point, a bi-linear interpolation using the 4 nearest points to the station location, is used to generate the model forecasts. Therefore, the results shown hereafter will be relative only to the nearest grid–point method. The performance of both systems is examined for 6 different thresholds: 1, 5,

Table 2: Main features of the verification configuration.

variable:	12–hour accumulated precipitation (18–06, 06–18 UTC);
period:	from 1 January to 31 March 2012;
region:	40–50N, 35E–45E;
method:	nearest grid–point;
observations:	SYNOP reports;
fcst ranges (h):	6-18, 18-30, 30-42, 42-54, 54-66
thresholds:	1, 5, 10, 15, 25, 50 mm/12h;
scores:	ROC area, BSS, RPSS, OUTL;

10, 15, 25 and 50 mm/12h.
The following probabilistic scores are computed over the verification period: the Brier Skill Score (BSS), the Ranked Probability Skill Score (RPSS), the Relative Operating Characteristic Curve (ROC) area and the Percentage of Outliers (OUTL). For a description of these scores, the reader is referred to Wilks (1995) and to Marsigli et al. (2008). The main features of the verification exercise are summarised in Table 2.

The skill of the two systems in terms of prediction of 12–hour accumulated precipitation is summarised in Fig. 2, where the Ranked Probability Skill Score (RPSS) is plotted against the forecast range for both COSMO–FROST–EPS and ECMWF EPS. It can be noticed

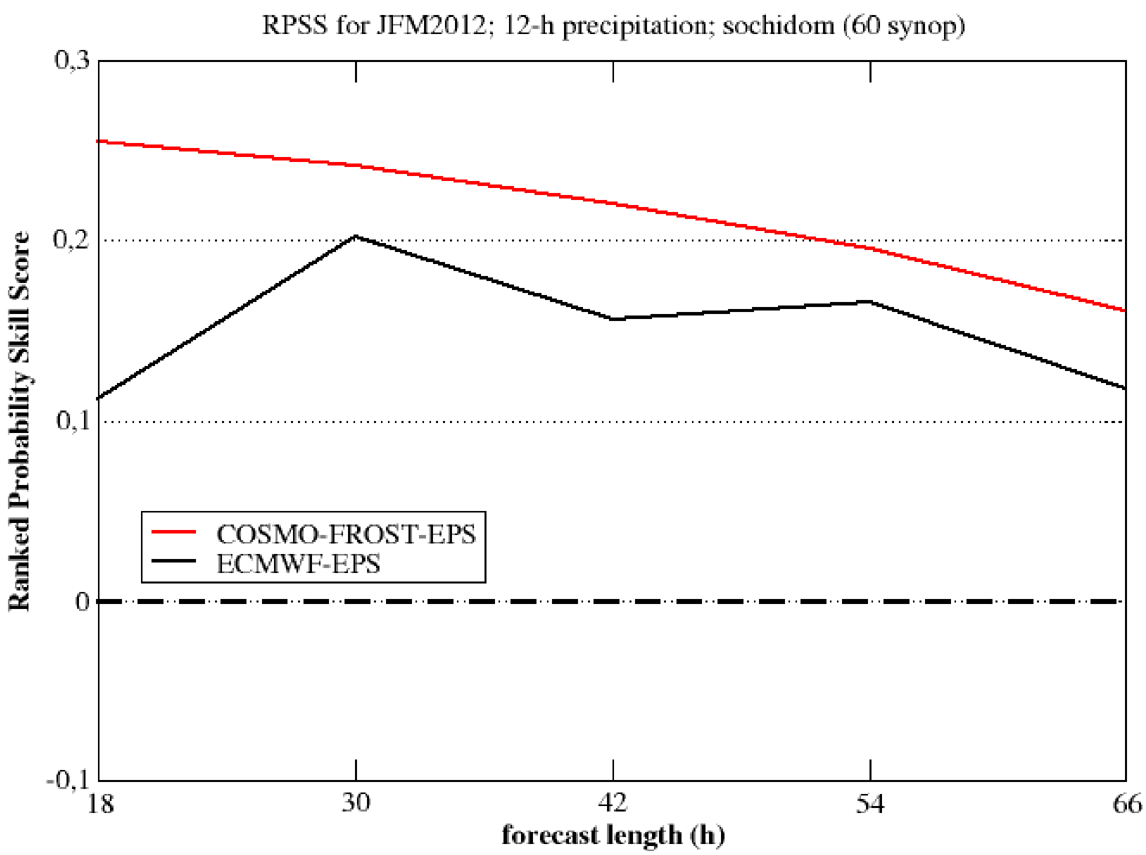

Figure 2: Ranked Probability Skill Score as a function of forecast length for COSMO–FROST–EPS (red) and ECMWF EPS (black), calculated over the 3–month period from January to March 2012.

that COSMO-FROST–EPS has higher RPSS for all forecast ranges. The difference between the two systems is consistent throughout the full forecast range, with a larger gap for the

first day of integration. This implies that, despite the higher ensemble size of ECMWF EPS, the higher resolution of COSMO-FROST–EPS contributes to provide more accurate probabilistic predictions of precipitation.
If the attention is now focused on the performance of both systems for a specific event, most of the above comments still hold. As an example, Fig. 3 shows the scores of COSMO-FROST–EPS and ECMWF EPS in terms of ROC area for the event "12–hour accumulated precipitation exceeding 10 mm". COSMO-FROST–EPS outperforms ECMWF EPS for all forecast ranges, although both systems exhibit a semi–diurnal cycle in the score and tend to provide better guidance for "night–time" precipitation, that is occurring between 18UTC and 6UTC (and corresponding to the ranges 6–18 h, 30–42 h and 54–66 h). As for COMO, this is linked with a too rapid onset of convection, as pointed out by Oberto and Turco (2008) for runs of COSMO in "deterministic mode".

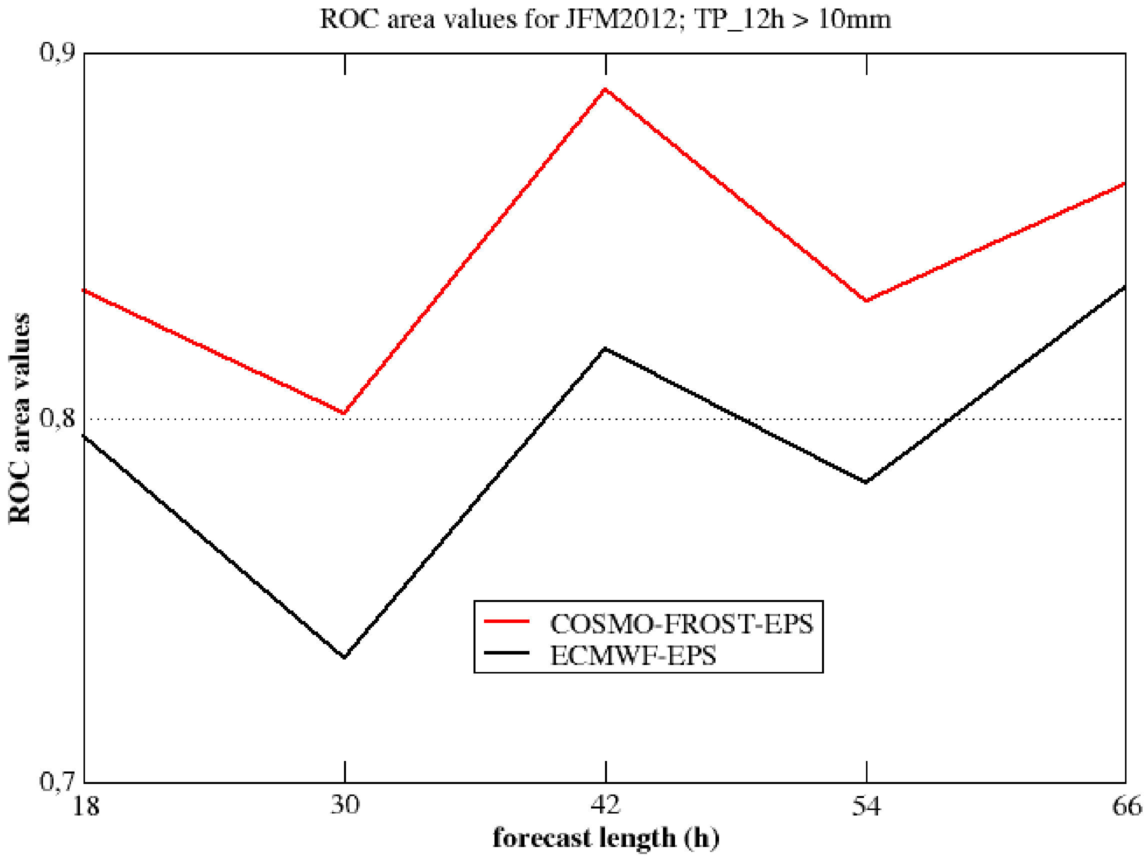

Figure 3: ROC area values for COSMO–FROST–EPS (red) and ECMWF EPS (black) relative to the event "precipitation exceeding 10mm in 12 hours" for the forecast ranges of Table 2. Both scores are calculated over the 3–month period from January to March 2012.

Finally, the attention is focused on the ability of COSMO–FROST–EPS to reduce the number of outliers with respect to ECMWF EPS, thanks to the higher resolution and the better description of mesoscale and orographic–related processes. Fig. 4 shows that COSMO–FROST–EPS has fewer outliers than the global ensemble, with a clear added value of the mesoscale ensemble for short forecast ranges.
According to Talagrand et al. (1999), the value of outliers for a reliable ensemble of size N is given by $2/(N+1)$. These values should not be exceeded. The dashed lines of Fig. 4 indicate these limits for both COSMO–FROST–EPS (red, 18%) and ECMWF EPS (black, 4%). Therefore, it looks as if COSMO–FROST–EPS approaches the theoretical value to larger extent than ECMWF EPS, which seems to have too many outliers in the short range.

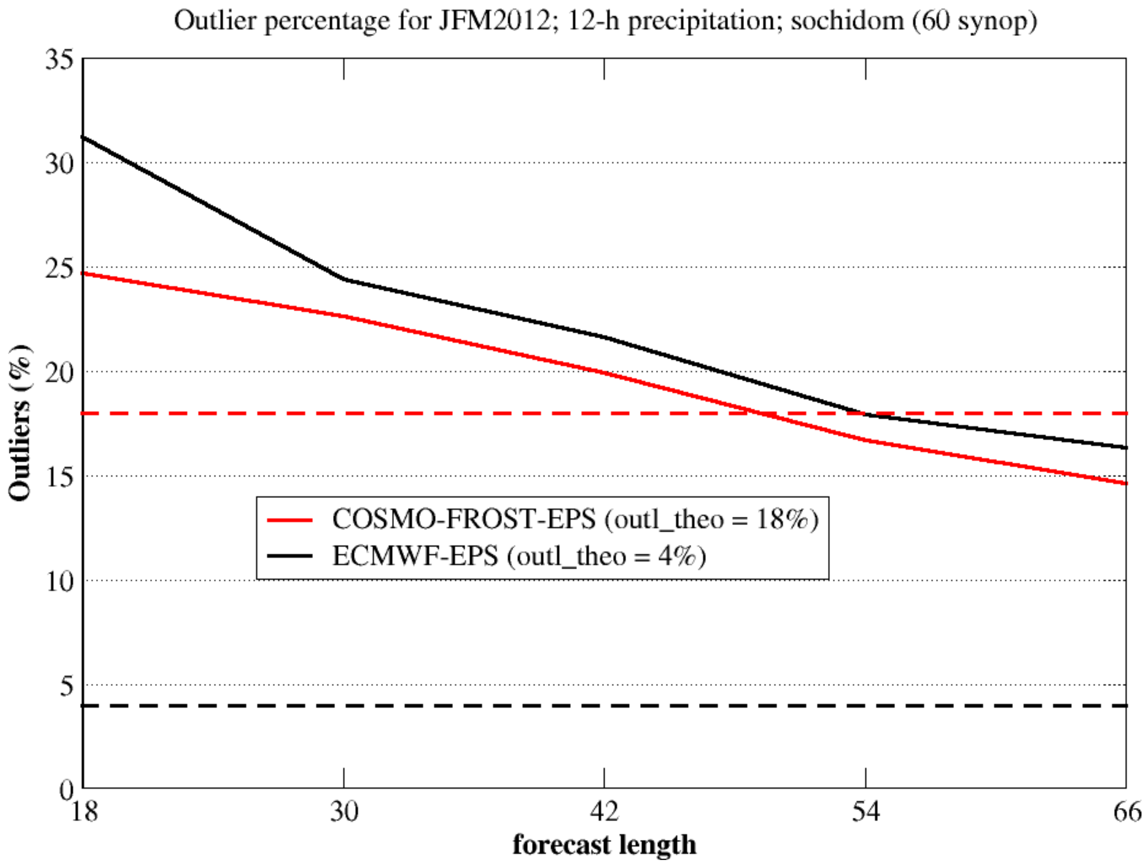

Figure 4: Percentage of Outliers for COSMO–FROST–EPS (red) and ECMWF EPS (black), calculated over the 3–month period from January to March 2012. The red (black) dashed line indicates the theoretical limit of outliers for COSMO–FROST–EPS (ECMWF EPS).

4 Summary and Outlook

COSMO–FROST–EPS is a limited–area ensemble prediction system which is supporting the probabilistic prediction of high–impact weather events for next winter Olympic Games. The system, based on a relocation of COSMO-LEPS, has been shown to provide added value with respect to the driving ensemble as for the probabilistic prediction of precipitation events. Although these results are still preliminary and not yet fully based on a long and statistically significant sample, they already show the potential of the system, which can provide accurate precipitation forecasts with high spatial detail.
In the near future, it is envisaged to perform a verification based on higher–resolution observational datasets and to improve upon the initialisation of the system in terms of soil–moisture and soil–temperature fields.

References

[1] Marsigli C., Montani A., Paccagnella T., 2008: A spatial verification method applied to the evaluation of high–resolution ensemble forecasts. *Met. Appl.*, **15**, 125–143.

[2] Montani A., Cesari D., Marsigli C., Paccagnella T., 2011: Seven years of activity in the field of mesoscale ensemble forecasting by the COSMO-LEPS system: main achievements and open challenges. *Tellus*,**63A**, 605-624. DOI: 10.1111/j.1600-0870.2010.00499.x

[3] Oberto, E. and Turco, M. 2008: Report about the latest results of precipitation verification over Italy. *COSMO Newsletter*,**8**, 3744. Available at: http://www.cosmo-model.org/

[4] Talagrand, O., Vautard, R. and Strauss, B. 1999: Evaluation of probabilistic prediction systems. *Proceedings of the ECMWF Workshop on Predictability*,Reading, UK, 2022 October 1997, 372. Available at: http://www.ecmwf.int/publications/.

[5] Wilks, D.S., 1995: Statistical Methods in the Atmospheric Sciences. *Academic Press*, New York, 467.

Test of a COSMO-based convection-permitting ensemble in the Hymex framework

Chiara Marsigli, Andrea Montani and Tiziana Paccegnella

ARPA-SIMC Hydro-Meteo-Climate Service of EMilia-Romagna, Bologna, Italy

1 Introduction

In view of the development of an ensemble system for the convection-permitting scale over Italy, in the recent years some tests aiming at defining the set-up of physics parameter perturbations for such an ensemble have been carried out at ARPA-SIMC (Marsigli, 2012). Thanks to the results of this study, a simple ensemble set-up has been defined and implemented for the first SOP (Special Observing Period) of the Hymex Project. Hymex (www.hymex-project.org) is a long lasting Project, aimed at the study of the Hydrological cycle over the Mediterranean. The first SOP was in Autumn 2012 and it permitted to collect a dense and rich observation network The ensemble set-up for the Hymex SOP period can be regarded as a "reference" ensemble, against which to compare other, more advanced, configurations. In particular, it is widely recognised that for this spatio-temporal scale a crucial ingredient is a good perturbation strategy for Initial Conditions (ICs). In the COSMO Consortium, great effort has been devoted to the development of a LETKF (Localised Ensemble Transform Kalman Filter) scheme for providing COSMO model analyses at the km-scale (KENDA, http://www.cosmo-model.org/content/tasks/priorityProjects/kenda/default.htm). Perturbed ICs derived from KENDA for the convection-permitting ensemble will be tested on the same period, in order to perform a clean comparison.

In this short paper, the behaviour of this reference ensemble is shown, to provide a reference against which to evaluate successive ensemble developments.

2 Ensemble set-up

COSMO-H2-EPS (which stands for COSMO Hymex 2.8km Ensemble Prediction System) consists of 10 runs of the COSMO model, with a horizontal resolution of 2.8km and 50 vertical level. It has been implemented over a north-western Mediterranean domain (figure 1), which covers north and entral Italy, including the whole Alpine chain, southern France, Switzerland and most of the Tyrrenean Sea. In the figure, the orography of the region as seen by the 2.8km model is shown.

Initial and boundary conditions are provided to the COSMO-H2-EPS members by the first 10 members of the COSMO-LEPS ensemble, which is running operationally with 7km horizontal resolution, nested on 16 ECMWF EPS members (see Montani et al., 2011, for further details). Therefore, no IC perturbations are applied at the small scale, both IC and BC being provided by COSMO-LEPS runs.

The COSMO-H2-EPS runs are differentiated also in the model physics set-up, since simple parameter perturbations are applied, following the previous experience of the SREPS and CONSENS Priority Projects. Perturbations are partly derived from those currently applied in the COSMO-DE-EPS ensemble (Gebhardt et al., 2011). The set-up of the suite, included perturbed values of the physics parameters, in decribed in Table 1.

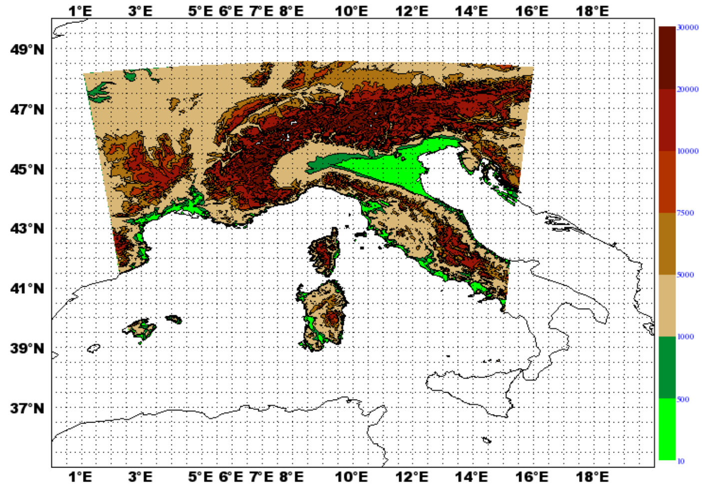

Figure 1: Orography of the COSMO-H2-EPS ensemble, showing also the model domain.

COSMO-H2-EPS was run for the whole SOP period (from 5th of September to 6th of Novembre 2012) and few products were sent to the Hymex SOP web site, where they were made available to the Hymex forecasters for the planning of the operations.

3 Results

The performance of the COSMO-H2-EPS ensemble for one event of the SOP (IOP16) is here briefly presented, in comparison with that of the driving ensemble COSMO-LEPS. In figure 2 the precipitation observed on the 26th of October 2012 is shown.

Stamp maps of the precipitation forecasted for the same period by the COSMO-LEPS ensemble starting at 12 UTC of the 25th of October are shown in figure 3. The forecast range is between 12 and 36 hours. The prediction can be regarded as good from a regional perspective, with some members forecasting high precipitation over the coasts of the Liguria region. Nevertheless, intense precipitation tends to be forecasted mainly over the central part of the region and on the Genova area, while the most intense precipitation was observed on the eastern part of the region and at the boundary with Tuscany (just above 44 N and around

Table 1: Set-up of the COSMO-H2-EPS system.

member	**tur_len**	**rlam_heat**	**cloud_num**	**entr_sc**	**pat_len**	**crsmin**
1	150	0.1	5.00e+08	0.0003	500	150
2	150	1	5.00e+07	0.0003	500	150
3	150	1	5.00e+08	0.0003	500	200
4	150	1	5.00e+08	0.002	500	150
5	500	1	5.00e+08	0.0003	500	150
6	150	1	5.00e+08	0.0003	500	150
7	150	1	5.00e+08	0.0003	1000	150
8	150	1	5.00e+07	0.002	500	150
9	500	0.1	5.00e+08	0.0003	500	150
10	150	1	5.00e+07	0.0003	500	150

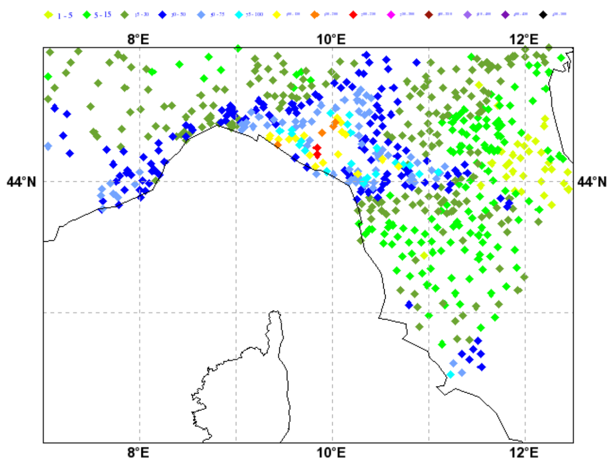

Figure 2: Observed precipitation accumulated over 24h, for the 26th October 2012.

10 E).

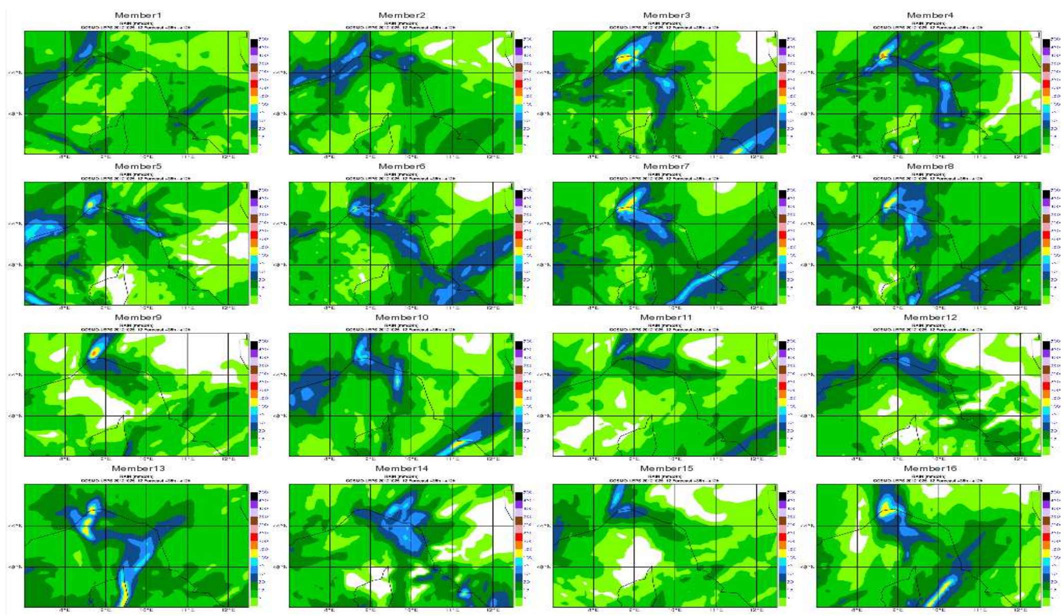

Figure 3: Precipitation forecasted by the COSMO-LEPS members starting at 12 UTC of the 25th of October, 12-36h forecast range.

Stamp maps relative to COSMO-H2-EPS for the same period are shown in figure 4, with the same 12-36h forecast range. The differences between each run and its father run are quite large for this case, with a general tendency of the higher-resolution run to forecast higher precipitation values and to modify the shape and location of the heavy precipitation pattern. Some members are now better able to indicate the eastern coast of Liguria as the area interested by heavy precipitation, extending the rainfall pattern towards northern Tuscany. This signal puts in evidence the importance of the high-resolution and of a better description of the orography of the area. Nevertheless, it is clear that the localisation of the phenomenon is an issue for the model, since precipitation over Northen Tuscany is still underestimated.

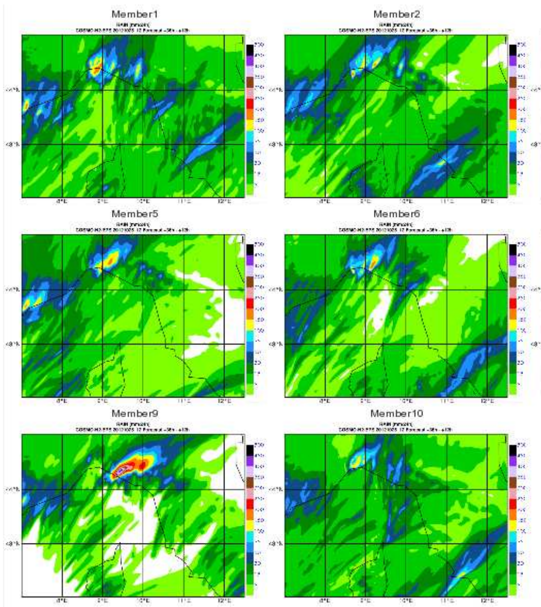

Figure 4: Precipitation forecasted by the COSMO-H2-EPS members starting at 12 UTC of the 25th of October, 12-36h forecast range.

In figure 5, the probability of precipitation exceeding 50 (left panel) and 100 (right panel) mm/24h as forecasted by the two ensemble is also shown.

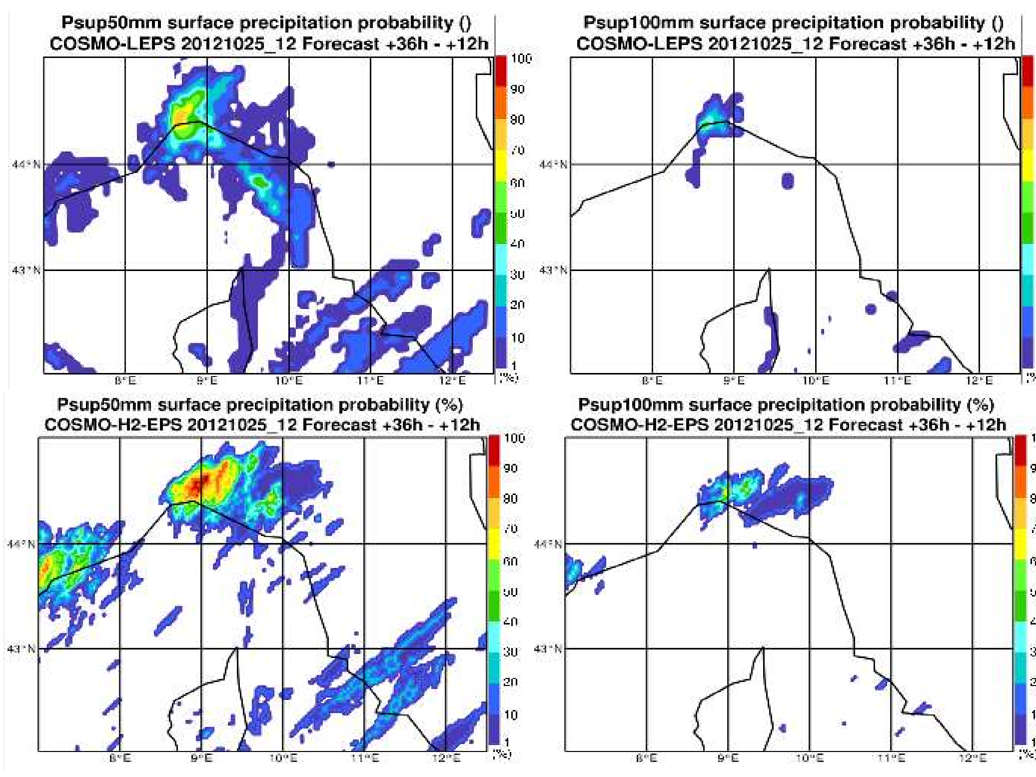

Figure 5: Probability maps for precipitation exceeding 50 (left) and 100 (right) mm/24h, for COSMO-LEPS (top panels) and COSMO-H2-EPS (bottom panels).

These maps provides a sort of summary of the signals which have been highlighted from an inspection of the stamp maps: the area which is more likely to be interested by heavy precipitation according to COSMO-H2-EPS is different from the one indicated by COSMO-LEPS. In particular, the occurrence of precipitation exceeding 100mm/24h, an event which was observed between 44 and 44.5 N and 9.5 and 10.5 E, is indicated as probable mainly over Genova and its surrounding by COSMO-LEPS, where it was not actually observed. Instead, only COSMO-H2-EPS indicate the event as likely also over the eastern part of the Liguria region, though the localisation is not perfect.

It is not possible to address, on the basis of few events only, the extent to which the different model perturbations influence the response of the COSMO runs. Therefore, it is not possible here to discuss why member 9 of this ensemble is so greatly overforecasting precipitation. Nevertheless, a statistical analysis over the whole period will likely permit to check if there are perturbations unsuitable for being included in the ensemble configuration .

4 Summary and Outlook

In the framework of the Hymex Project, a simple convection-permitting ensemble based on the COSMO model has been implemented and run for the first SOP of the Project. This basic set-up will serve as a reference run, against which to test all the further improvement to the ensemble methodology that are being made available in the COSMO Consortium.

First results show that the high-resolution ensemble can bring benefit in terms of PQPF with respect to the driving 7km ensemble.

In the next future, a new version of the ensemble will be run over the same period, with ICs derived from the KENDA system, exploiting the opportunity offered by this project framework, since the observation network made available for the SOP could be used for the ensemble data assimilation.

Further work will be devoted to the determination of how to best get BC perturbations. The reference ensemble, where BCs are derived from COSMO-LEPS, will be compared with a direct downscaling of the ECMWF EPS. The impact of model perturbations will be also addressed, by considering new parameters to be perturbed and by testing the stochastic tendencies methodology which is being recently implemented in the COSMO model.

This extensive testing will hopefully permit to define: the set-up of KENDA for providing IC perturbations to a 2.8km ensemble over Italy, a set of model perturbations for this resolution and a strategy for the BC perturbation. These ingredients will be then combined for testing the complete ensemble set-up.

References

[1] Gebhardt, C., S. E. Theis, M. Paulat, Z. Ben Bouallègue, 2011. Uncertainties in COSMO-DE precipitation forecasts introduced by model perturbations and variation of lateral boundaries. *Atmospheric Research*, **100**, Issues 2-3, 168-177.

[2] Marsigli, C., 2012. Testing the impact of model perturbations applied to the COSMO model at a convection-permitting scale over Italy. ECMWF Special Project report 2012. accessible at: http://www.ecmwf.int/about/special_projects/index.html#2012.

[3] Montani, A., D. Cesari, C. Marsigli and T. Paccagnella, 2011: Seven years of activity in the field of mesoscale ensemble forecasting by the COSMO-LEPS system: main achievements and open challenges. *Tellus*, **63A**, 605-624.

List of COSMO Newsletters and Technical Reports

(available for download from the COSMO Website: www.cosmo-model.org)

COSMO Newsletters

No. 1: February 2001.

No. 2: February 2002.

No. 3: February 2003.

No. 4: February 2004.

No. 5: April 2005.

No. 6: July 2006; Proceedings from the COSMO General Meeting 2005.

No. 7: May 2008; Proceedings from the COSMO General Meeting 2006.

No. 8: August 2008; Proceedings from the COSMO General Meeting 2007.

No. 9: December 2008; Proceedings from the COSMO General Meeting 2008.

No.10: January 2010; Proceedings from the COSMO General Meeting 2009.

No.11: February 2011; Proceedings from the COSMO General Meeting 2010.

No.12: March 2012; Proceedings from the COSMO General Meeting 2011.

No.13: April 2013; Proceedings from the COSMO General Meeting 2012.

COSMO Technical Reports

No. 1: Dmitrii Mironov and Matthias Raschendorfer (2001):
Evaluation of Empirical Parameters of the New LM Surface-Layer Parameterization Scheme. Results from Numerical Experiments Including the Soil Moisture Analysis.

No. 2: Reinhold Schrodin and Erdmann Heise (2001):
The Multi-Layer Version of the DWD Soil Model TERRA_LM.

No. 3: Günther Doms (2001):
A Scheme for Monotonic Numerical Diffusion in the LM.

No. 4: Hans-Joachim Herzog, Ursula Schubert, Gerd Vogel, Adelheid Fiedler and Roswitha Kirchner (2002):
LLM ⁻ the High-Resolving Nonhydrostatic Simulation Model in the DWD-Project LIT-FASS.
Part I: Modelling Technique and Simulation Method.

No. 5: Jean-Marie Bettems (2002):
EUCOS Impact Study Using the Limited-Area Non-Hydrostatic NWP Model in Operational Use at MeteoSwiss.

No. 6: Heinz-Werner Bitzer and Jürgen Steppeler (2004):
Description of the Z-Coordinate Dynamical Core of LM.

No. 7: Hans-Joachim Herzog, Almut Gassmann (2005):
Lorenz- and Charney-Phillips vertical grid experimentation using a compressible non-hydrostatic toy-model relevant to the fast-mode part of the 'Lokal-Modell'

No. 8: Chiara Marsigli, Andrea Montani, Tiziana Paccagnella, Davide Sacchetti, André Walser, Marco Arpagaus, Thomas Schumann (2005):
Evaluation of the Performance of the COSMO-LEPS System

No. 9: Erdmann Heise, Bodo Ritter, Reinhold Schrodin (2006):
Operational Implementation of the Multilayer Soil Model

No. 10: M.D. Tsyrulnikov (2007):
Is the particle filtering approach appropriate for meso-scale data assimilation?

No. 11: Dmitrii V. Mironov (2008):
Parameterization of Lakes in Numerical Weather Prediction. Description of a Lake Model.

No. 12: Adriano Raspanti (2009):
Final report on priority project VERSUS (VERification System Unified Survey).

No. 13: Chiara Mirsigli (2009):
Final report on priority project SREPS (Short Range Ensemble Prediction System).

No. 14: Michael Baldauf (2009):
COSMO Priority Project "Further Developments of the Runge-Kutta Time Integration Scheme" (RK); Final Report.

No. 15: Silke Dierer (2009):
COSMO Priority Project "Further Developments of the Runge-Kutta Time Integration Scheme" (RK); Final Report.

No. 16: Pierre Eckert (2009):
COSMO Priority Project "INTERP"; Final Report.

No. 17: D. Leuenberger, M. Stoll, A. Roches (2010):
Description of some convective indices, implemented in the COSMO model.

No. 18: Daniel Leuenberger (2010):
Statistical Analysis of high-resolution COSMO Ensemble forecasts, in view of Data Assimilation.

No. 19: A. Montani, D. Cesari, C. Marsigli, T. Paccagnella (2010):
Seven years of activity in the field of mesoscale ensemble forecasting by the COSMO-LEPS system: main achievements and open challenges.

No. 20: A. Roches, O. Fuhrer (2012):
Tracer module in the COSMO model.